University of Alberta

Sputtered Magnesium Aluminum and Magnesium Aluminum Titanium Alloys for Hydrogen Storage

by

Julian Haagsma

A thesis submitted to the Faculty of Graduate Studies and Research
in partial fulfillment of the requirements for the degree of

Master of Science

in

Materials Engineering

Chemical and Materials Engineering

Fall 2011
Edmonton, Alberta

This thesis is dedicated to
My family.

Abstract

Hydrogen storage has been a key area of focus in the clean energy field for over a decade, as it is a major obstacle to the widespread adoption of fuel cells for mobile applications. The aim of this thesis research was to improve the Magnesium Aluminum hydrogen storage system in order to make it operate faster and at lower temperatures, by kinetic and thermodynamic improvements. Magnesium Aluminium Titanium was examined as alloy additions were seen as a method to improve on Magnesium Aluminum. Improvements to kinetics were observed with Magnesium Aluminium Titanium, but no thermodynamic improvements were found, and hydrogen was stored predominantly as alpha magnesium hydride. Median charging times of less than 15 seconds to 90 percent of maximum capacity were found in 85Mg7.5Al7.5Ti samples over 100 cycles, and a median of 5.29 weight percent reversible storage was found in 85Mg10Al5Ti.

Preface

This work presents the theory, experimental methods, and results separately. Chapter 1 gives an introduction to the topic of hydrogen storage, and the reasons for choosing Magnesium based alloys for hydrogen storage. Chapter 2 explains the theory and reasons for conducting the research at the time it was performed. Chapter 3 contains a brief review of literature as it relates to Magnesium Aluminum and Magnesium Aluminum Titanium alloys used for hydrogen storage. Chapter 4 explains the experimental conditions of each apparatus, and the geometries of samples created. Chapter 5 contains all the results, split into two halves, the first Magnesium Aluminum, and the second Magnesium Aluminum Titanium; this is the chronological order in which these two halves of the research were performed. Finally, Chapter 6 contains conclusions regarding the results of this study.

Acknowledgements

I would like to thank Christopher Harrower and Peter Kalisvaart for their assistance in this work, including their help with operating the Sieverts Apparatus, as well as Colin Ophus for SEM and other ideas, Reza Mohammadi for SEM and EDXS, and Xue-Hai Tan for his help with DSC-TGA sample preparation, as well as my supervisor, David Mitlin.

Contents

Contents

Contents

List of Figures

List of Figures

List of Tables

List of Symbols

Symbol	Meaning [units]
ΔG	Gibbs energy [J/mol]
ΔH	Enthalpy [kJ/mol]
ΔS	Entropy [J/mol]
K	Equilibrium constant
μ	Chemical potential [J/mol]
Z	Grain separation

Symbol	Meaning [units]
p	Pressure [atm]
T	Temperature [K]
t	Time [s]
R	Ideal gas constant [J/(K*mol)]
D	Diffusion coefficient [J/(K*mol)]
d	Grain size

List of Abbreviations

Abbreviation	Meaning
CV	Contracting volume
DSC	Differential scanning calorimetry
DSC-TGA	Differential scanning calorimetry with thermogravimetric analysis
EDXS	Energy-dispersive x-ray spectroscopy
HPDSC	High-pressure differential scanning calorimetry
JCPDS	Joint Committee on Powder Diffraction Standards
KJMA	Kolmogorov-Johnson-Mehl-Avrami
SEM	Scanning electron microscopy
TGA	Thermogravimetric analysis
XRD	X-ray diffraction

1

Introduction to Hydrogen Storage

Modern society requires energy to function. World energy usage has been constantly increasing, and predictions indicate it will continue to increase rapidly as large developing nations strive to close the gap with the first world. Oil, in particular, has become an increasing concern for energy driven economies, as demand continues to rise much faster than supply, and particularly since it is a non-renewable fossil fuel with limited long-term supply. Environmental factors have made many question the use of fossil fuel based transportation and power. Recent peaks in the price of oil have also caused many to reconsider the energy source of the transportation sector. Hydrogen, as a clean fuel that can be produced from both renewable and non-renewable sources, is an alternative fuel and energy storage mechanism that many believe will play in

important role in the future of energy-based economies.

Hydrogen as an alternative fuel-system has four major areas: production, delivery, storage, and fuel cells. Hydrogen storage[1, 2] in particular is a major problem that must be addressed when moving to hydrogen fuel systems; for mobile applications such as vehicles, the total weight and volume of the system required to store hydrogen is of key importance, as the entirety of the system must be moved and contained within the vehicle. Hydrogen is traditionally stored in high-pressure tanks, or cryogenically cooled to below 21K, the point at which it becomes a liquid. Both of these solutions have serious issues: high-pressure tanks are typically steel, holding only a small fraction of their weight as hydrogen, and necessitate a variable delivery pressure; cryogenic cooling requires continuous cooling from complex refrigeration systems.

The most promising alternative hydrogen storage methods are high-pressure composite-material tanks, or metal hydride based storage[1]. Metal hydrides are intermetallics in which hydrogen chemically binds with one or more metal atoms, essentially allowing them to absorb and desorb hydrogen; metal hydrides are typically stable under ambient temperatures and pressures, a desirable trait for storage applications. Most metal-hydride hydrogen storage materials developed to date are either too heavy, or desorb at temperatures that are too high, or are not stable over enough hydrogen sorption cycles[3].

One of the more promising candidates within the metal-hydride hydrogen-storage field are Mg-based materials, as they can store a high percentage of hydrogen by weight when compared to conventional metal-hydrides currently in use in applications such as batteries, and compared to steel hydrogen tanks. There are a number of Mg-based systems, some of which catalyze magnesium hydride, and others which use more complex Mg-based hydrides.

The goal of this thesis was to investigate one of the promising Mg-based hydrogen storage material systems, MgAl, and improve its performance in terms

of operating temperature, absorption and desorption time, cycling stability, and operating pressures, without sacrificing too much weight percentage from the theoretical maximum of pure magnesium hydride. This was to be achieved through compositional variations and further alloy additions, using sputtering as a fast-prototyping method.

During the course of this research MgAl was determined to have an optimum composition for lower temperatures of absorption and desorption (200°C) near 70Mg30Al. Titanium was added to the MgAl system and an optimum composition was found at 70Mg15Al15Ti for speed and stability at a low temperature (300°C); this optimum composition is competitive with other materials in literature at these temperatures and weight percentages of sorption.

1.1 Hydrogen as a fuel

Hydrogen, in pure form, is usable as a fuel either through direct combustion with oxygen, creating heat, or through hydrogen fuel cells, creating electricity. Fuel cells, initially invented in 1945[4], have been used as a power source since the 1960's with the development of proton exchange membrane (PEM) fuel cells for the U.S. space program[5, 6], and the construction of the first prototype fuel-cell vehicle by General Motors in 1966[7]. More recent efforts have included the use of a fleet of hydrogen fuel cell buses constructed by Ballard Power[8], and numerous plans to convert local transportation, especially buses, to hydrogen powered vehicles[9–11]. While many of these efforts focus on transportation issues, there are several other major applications for which hydrogen as a fuel and as an energy storage medium are being considered.

1.2 The Hydrogen Economy

The Hydrogen Economy has been a phrase used since the 1970's to refer primarily to the switch to hydrogen-based transportation[12], and, to a lesser degree, the use of hydrogen as an energy storage medium. The purpose of moving to a hydrogen economy is multi-faceted: energy efficiency, global warming, localized air pollution, dependence of the United States upon foreign oil sources, the price of oil with increasing global demand and the storage of renewable energies are among the major topics typically addressed in the promotion of the hydrogen economy concept[2, 13–15].

1.2.1 Efficiency

One of the primary reasons to move to hydrogen as a fuel for the transportation sector is the inefficiency of internal combustion engines, both in terms of energy efficiency and CO_2 emissions (Figure 1.1)[15]. Electric-drive vehicles have higher efficiencies than internal combustion engines primarily due to the latter having very poor thermal efficiency (around 20%); most of the energy produced by burning gasoline is lost as heat. That electric vehicles, in their infancy relatively, are comparable to hybrid-electric vehicles and better than regular internal combustion engine vehicles, without any specialized infrastructure having been developed and assuming current energy generation and distribution [15], shows that they have great promise; it is hoped that further investment and refinement in electric vehicles would lead to improvements in the technology.

In terms of CO_2 emissions, electric-vehicles, including fuel cell vehicles, are more efficient than internal combustion engines again due to the low thermal efficiency of the latter. The emissions of hydrogen-fuelled vehicles is directly based on how hydrogen is generated - if one assumes that hydrogen is being

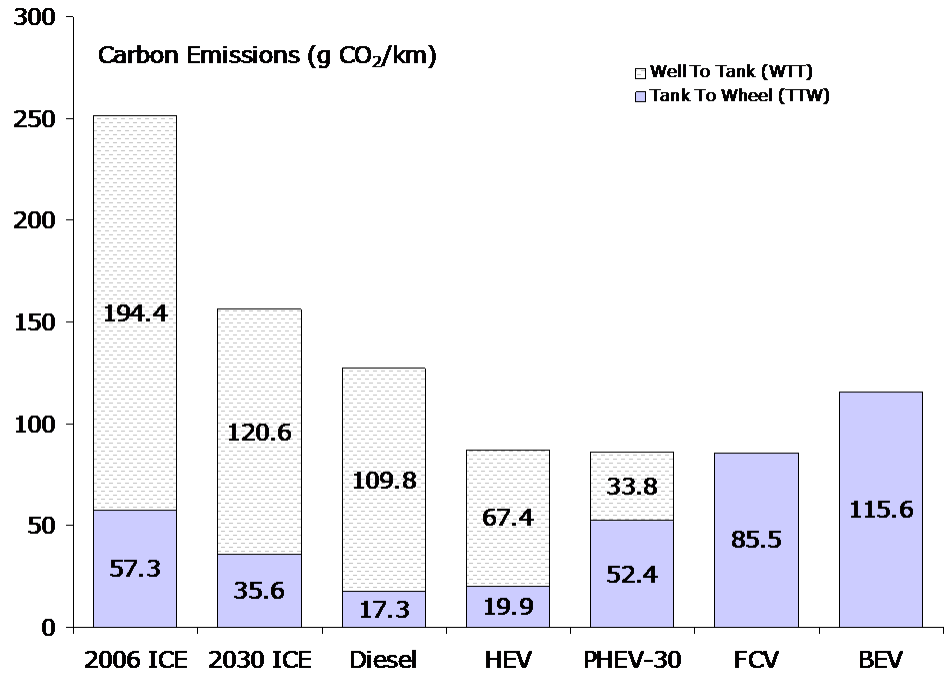

Figure 1.1: "Well-to-Wheel" greenhouse gas production of various technologies; adapted from Kromer[15]. ICE = Internal Combustion Engine; HEV = Hybrid Electric Vehicle; PHEV-30 = Plugin Hybrid Electric Vehicle (30 mile electric range); FCV = Fuel Cell Vehicle; BEV = Battery Electric Vehicle

produced through electrical means, then the average emissions per unit energy produced on the grid must be considered; as countries begin to move away from fossil-fuel based generation, the emissions of electric vehicles become more favourable. If methane reforming is used, lowering carbon dioxide emissions would depend on the implementation of carbon sequestration techniques [16].

Compared directly to electric vehicles being powered from the grid, hydrogen vehicles have a key advantage over battery-electric vehicles in that the generation of hydrogen using electrolysis could be performed at the power plant, without associated grid losses; hydrogen distribution is a layer of infrastructure which would need to be developed for this implementation.

Load balancing the electric grid is yet another use for hydrogen in the hydrogen economy. The electric grid experiences a cyclic load with sometimes unpredictable increases in use; these fluctuations are normally compensated for with power generation units that can be turned on quickly [17]. In a hydrogen economy, the base power generation could be built to higher levels than the minimum load, and the excess energy used to produce hydrogen in low-load periods and during high-load periods this hydrogen would be used to generate electricity for the grid. This is especially useful with nuclear technology, as a nuclear power plant cannot easily adjust its power output to load conditions.

Further load-balancing of the grid could be achieved if home-refuelling of hydrogen vehicles becomes common. Honda has been experimenting with home-refuelling hydrogen stations for fuel cell vehicles, which could interact with an intelligent grid so that they produce their hydrogen during off-peak hours [18].

1.2.2 Global Warming

Global warming, the gradual increase in global mean temperature, has been observed for several hundred years, and has been recently attributed to the

greenhouse effect, the process by which atmospheric CO_2 traps heat from the sun, due to the extensive use of fossil fuels since the industrial revolution in the 1800's.[19] Fossil fuels, which were formed from atmospheric CO_2 and stored in the ground for millions of years, emit CO_2 when burned; increasing emission rates of CO_2 into the atmosphere caused by the burning of fossil fuels might lead to an acceleration of global warming, as the ocean sink and biosphere are unable to absorb and utilize as large a proportion of CO_2 as they have historically.[20]

Projections of warming of global average temperatures by the end of the 21st century have produced median figures around 4°C [21]. this sort of temperature change may have unprecedented effects on the climate and consequently on society as a whole.

Moving to a hydrogen-based fuel for transportation from fossil fuels would eliminate this additional emission of CO_2 into the atmosphere (provided the hydrogen was produced without burning CO_2), significantly reducing total emissions and bringing us closer to an equilibrium CO_2 concentration, potentially slowing the rate of global warming.

1.2.3 Localized Air Pollution

While greenhouse gasses, specifically CO_2, receive the most media attention out of all vehicular emissions, other emissions such as nitrogen oxides (NO_x), carbon monoxide (CO), sulphur dioxide (SO_2) and particulate matters, which are largely responsible for smog in cities, are a more localized problem. These emissions would be severely reduced in the move to fuel cell or electric vehicles, and could lead to a significant increase in air quality [11, 22].

1.3 Hydrogen Production

1.3.1 Steam Reforming

Steam reforming of methane is currently the predominant form of hydrogen production, wherein natural gas (CH_4) is exposed to steam at temperatures of ~800°C in the presence of a nickel-based catalyst [23]. The water reacts with methane producing hydrogen and carbon monoxide, which further reacts with water to form hydrogen and carbon dioxide ($CH_4 + 2H_2O \rightarrow CO_2 + 4H_2$). This process is economical at the industrial scale, and has an efficiency of 65-75%, but produces quantities of CO_2 that are similar to those produced burning conventional fossil fuels [24].

1.3.2 Electrolysis

Electrolysis of water is a well established process wherein electricity is used to dissociate hydrogen and oxygen from water; as hydrogen is released at one electrode and oxygen at the other, it is a good source for high-purity hydrogen, and also an ideal method for remote production of hydrogen, as only water and electricity are required as inputs [25]. Electrolysis of water can be somewhat efficient at high temperatures (~59%), but conventional alkaline water electrolysis is less than half this efficient [26]. This efficiency is relative to electrical input, however, and electrical generation has its own inefficiencies which must be factored in when considering large-scale electrolysis; electrical conversion efficiencies in nuclear reactors, for example, currently ranges from ~34% to ~50% [27], and the best cases combined would result in a net efficiency of ~30%.

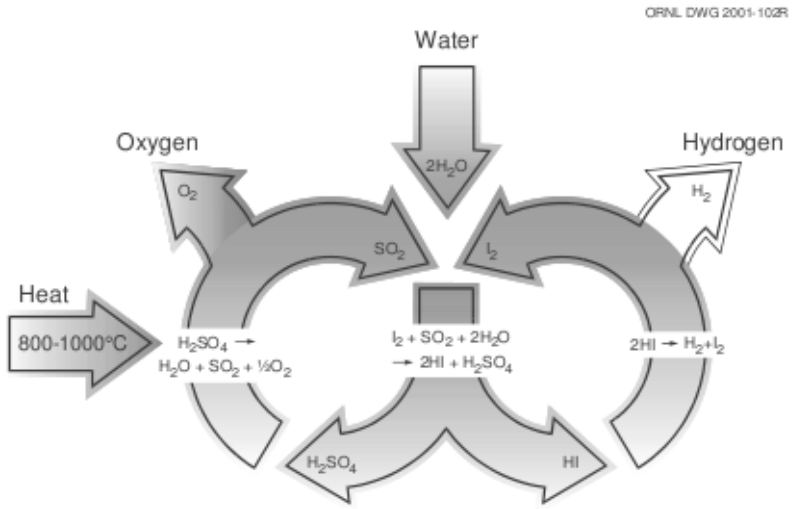

Figure 1.2: The iodine-sulphur reaction for producing hydrogen thermochemically; reproduced from Forsberg [27].

1.3.3 Thermochemical Hydrogen Production

The leading long term option for large scale hydrogen production is thermochemical hydrogen production using nuclear energy, where heat decomposes water into H_2 and oxygen [27]. This process requires high temperatures (>750°C) for it to be efficient, and involves using one of several chemical cycles which yield this net result. The iodine-sulphur reaction, shown in Figure 1.2, is a leading example of one of these reactions and can be developed into a more efficient source of hydrogen production; due to the removal of electricity generation as a required intermediate step for dissociation, and combining the cycle with a traditional electricity generating nuclear reactor may yield combined efficiencies of ~60%, [27], very competitive to electrolysis after electrical conversion is considered.

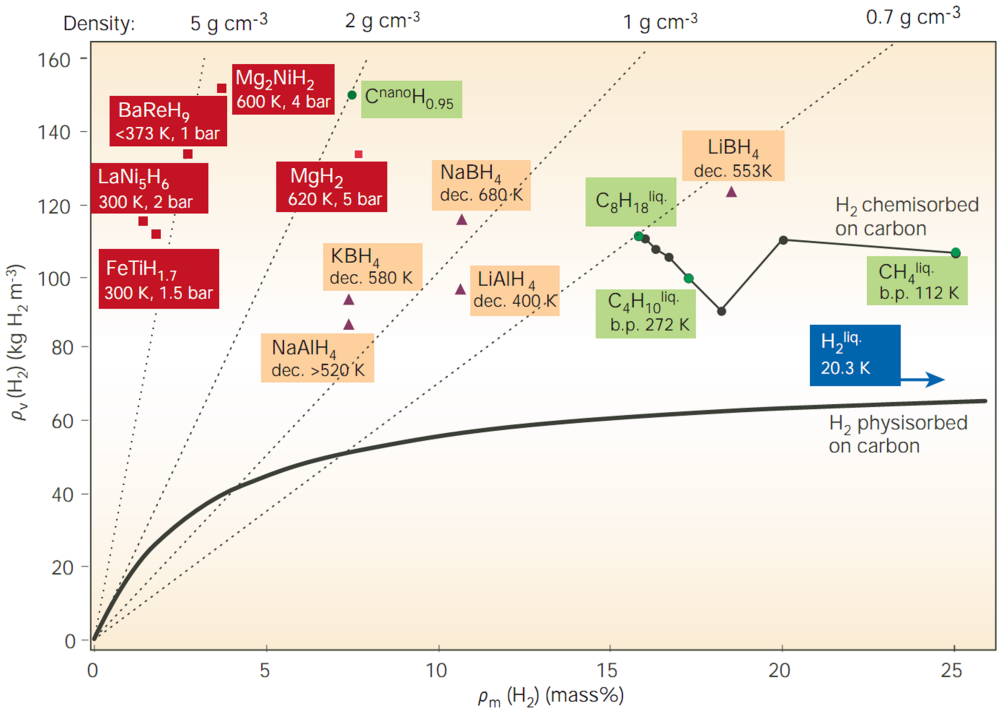

Figure 1.3: An overview of various hydrogen storage materials, from Schlapbach et al. [14].

1.4 Hydrogen Storage

As mentioned previously, there are several classes of materials that can be used to store hydrogen: storage in tanks, adsorption on a high-surface-area material, storage in metal hydrides, storage in alanates and light hydrides, as liquid hydrogen, and others [14], as seen in Figure 1.3. As each of these classes of material has different properties, and given their vested interest in the development of hydrogen storage materials, the United States Department of Energy (DOE) developed a series of targets for hydrogen storage, to enable their use in vehicular applications without adding much more weight to the vehicle compared to an internal combustion engine plus fuel tank, and without occupying much more combined volume than that of an internal combustion engine system, and without requiring operating temperature significantly removed from ambient temperature. In 2002, the DOE goals were 6.5 weight percentage hydrogen stored of system weight - gravimetric hydrogen density - operating between 0°C and 100°C [14]. By 2007, the DOE goals for 2010 had been updated to 6% of system weight (gravimetric capacity), operating between -30°C and 85°C, delivered at 8bar with a 3 minute fuelling time, plus with a low total system cost, with a volumetric capcity of 0.045 kg_{H_2}/L.[13] These goals were set with the intention of fuelling a mid-sized vehicle for a distance of ~400km; using a hydrogen fuel cell this may be accomplished with approximately 4 kg of hydrogen.[14] Standard hydrogen tanks are considered dangerous and heavy for use in standard vehicles, although composite tanks are being developed, and their volume is considerable. Initial reported success of high-surface-area materials - specifically with carbon nanotubes - were not reproducible elsewhere, and although nanostructured graphitic carbon is able to reversibly store 2 percent of its weight in hydrogen, this is at 77 K [14], essentially cryogenic temperatures well below the desired temperature ranges. Metal hydrides can be capable of storing large amounts of hydrogen, by dissociating H_2 into two H atoms which combine with a metal atom to form a

hydride of the form A_xH_y or $A_xB_yH_z$. Many, such as MgH_2 or rare earth hydrides are not within the desired ranges either; MgH_2, specifically, can store 7.6 weight% hydrogen, but requires 300°C for a 1 bar plateau pressure and has slow kinetics - causing a slow absorption and desorption speed - but it is low cost [14, 28, 29]. Alanates store an even higher weight percentage than heavier metal hydrides - up to 18% for $LiBH_4$ - but they desorb at even higher temperatures up to 600°C [14]. With each class of material having issues of some sort, engineering a material towards the desired properties becomes necessary [30]; some aspects, like the price of the material, cannot be modified through materials design except through reduction in quantity of expensive materials - while Mg is relatively inexpensive, elements such as Ni, Ti, V and Cr are considerably higher, and La (a staple of the LaNi hydrides) is 100 times more costly than Mg [28]. In the case of MgH_2, lowering the hydrogen desorption temperature and improving the kinetics are the key desirable changes, as it holds enough hydrogen to meet the original 6.5% target and the later 6% of the 2010 goals. One of the more successful modifications to Mg is Mg_2Ni, but it still requires high temperatures for desorption and sacrifices considerable gravimetric density[3, 28]; another modification to MgH_2 is the addition of Al: MgAl by high-energy ball-milling has been shown to be able to lower the plateau pressure, and the addition of Al maintains the low cost aspect of the material [3, 28, 31]; this study begins with this composition and seeks to prototype it and additions to it through sputtering for rapid creation of new compositions - on the order of one hour to create a new material - with the aim of improving the thermodynamics and kinetics of absorption and desorption of hydrogen; with the aforementioned goals in mind, our target is to make an inexpensive material with a reversible capacity of 5 weight%, cyclable at 200C or less for at least 100 cycles, with a charing time of 5 minutes or less.

2

Theory

In order to design a hydrogen storage system, the properties of the materials to be used and their interactions with hydrogen must be understood. The key properties of a hydrogen storage material are: the thermodynamic stability of the hydride, the kinetics of hydrogen sorption, the maximum hydrogen capacity of the material, and the cycling ability of the material. The first two will be discussed in their respective sections, while the latter two will be addressed under microstructure.

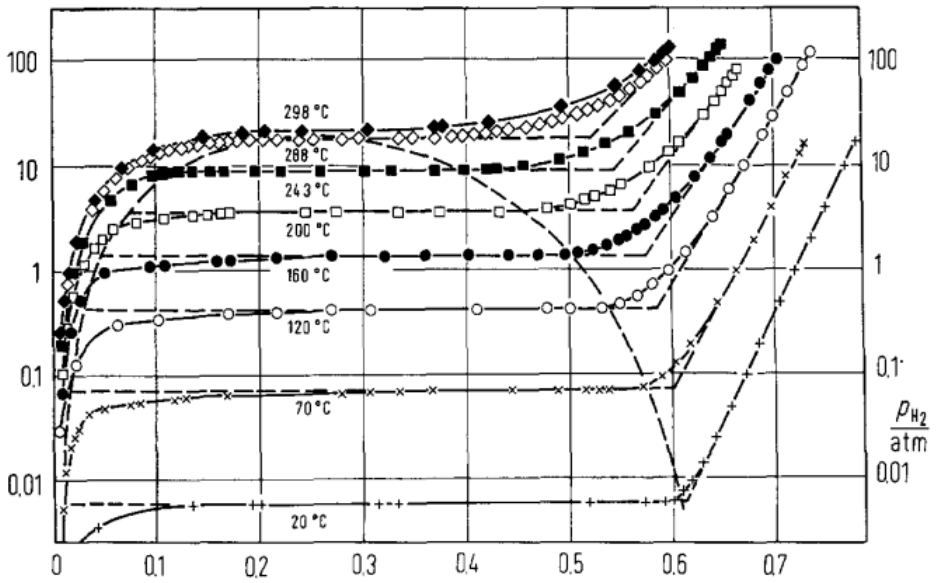

Figure 2.1: A series of Pressure Concentration Temperature (PCT) measurements on the Pd-H system reported by Frieske and Wicke [32].

2.1 Thermodynamics of Magnesium - Hydrogen

When referring to the thermodynamics of a hydrogen storage material, the discussion typically focuses on the enthalpy of hydride formation, as this property primarily dictates the temperatures and pressures at which hydrogen sorption can occur. During hydrogen absorption, hydrogen transforms a metallic phase into a binary intermetallic of that metal and hydrogen; for example, $Mg + H_2 \rightarrow MgH_2$. This reaction may be either exothermic or endothermic, depending upon the metal-hydrogen system in question; the energy released or absorbed is the change in Gibbs free energy, ΔG which can be expressed as

$$\Delta G = \Delta H - T\Delta S \tag{2.1.1}$$

where ΔH is the enthalpy of formation and ΔS is the entropy of formation. The entropy of formation ΔS is primarily from the loss of entropy of gaseous hydrogen and thus is approximately constant per mol of hydrogen evolved for

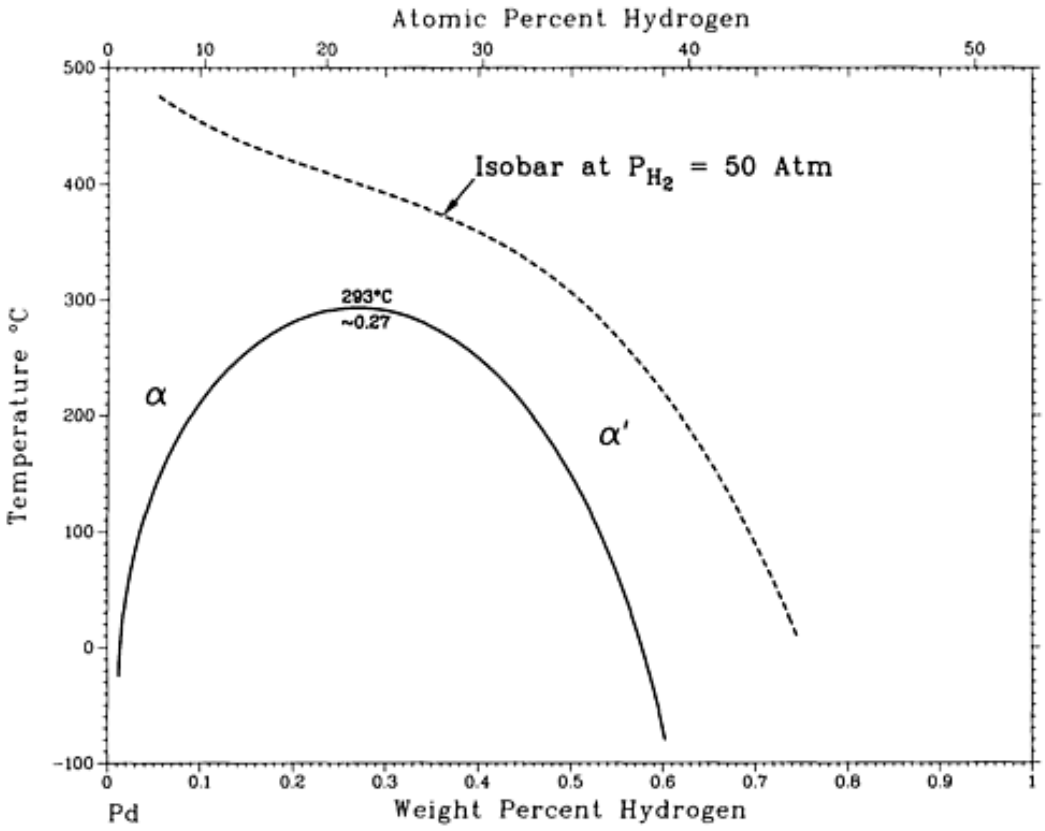

Figure 2.2: The Hydrogen-Palladium phase diagram[33].

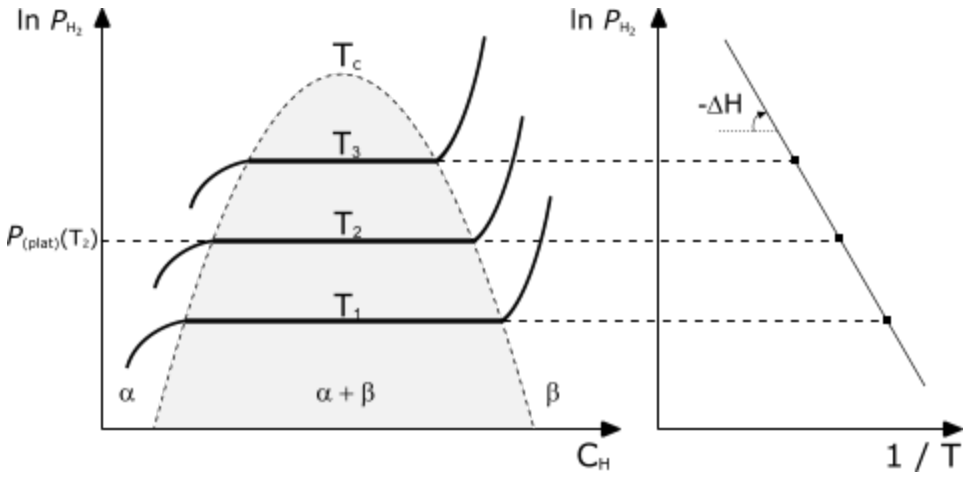

Figure 2.3: Pressure-composition isotherms (PCT) of hydrogen (α) absorbing into a material to form a hydride phase (β); the pressures $p_{(\mathrm{plat})}(T)$ of the plateaus where phase transformation occurs may be plotted as $\ln p$ vs $1/T$ to create a *van't Hoff* plot, from which the enthalpy of hydride formation ΔH may be obtained. Adapted from Schlapbach [34] and Gross [1].

all metal-hydrogen systems, that is $\Delta S^\circ \cong -\Delta S_{H_2} = -130.8$ JK^{-1}/mol H_2 [35–37]; thus the stability of the metal hydride is primarily based upon the enthalpy of formation. The behaviour of sorption can be described using the *van't Hoff* equation

$$\frac{d \ln K}{dT} = \frac{\Delta H^\circ}{RT^2} \tag{2.1.2}$$

where ΔH° is the enthalpy change in the standard state (1 bar pressure for gas), and K is the equilibrium constant [38], which can be easily derived from the definition of the equilibrium constant $K \equiv e^{-\Delta G^\circ / RT}$.

The hydriding behaviour of a material may be illustrated by examining a Pressure Concentration Temperature (PCT) measurement; PCT measurements - although not performed during this study due to their time-consuming nature as equilibrium measurements, and a focus on cycling behaviour - effectively demonstrate the relation between temperature, pressure and concentration of hydrogen within a hydrogen sorption material. Figure 2.1 shows a series

of PCT measurements reported by Frieske and Wicke in 1973 on the Pd-H system. In PCT measurements, which are isothermal, the pressure of H_2 is increased in very small increments and allowed to equilibrate; the pressure of H_2 in the system increases until the hydrogen sorption material begins to absorb hydrogen; this pressure is termed the plateau pressure, as the pressure then remains relatively constant while the metal becomes slowly hydrided, until the material is fully hydrided at that temperature, whereupon the pressure resumes its increase. Several isotherms can be put together and used to construct a phase diagram [39]: the dashed line in Figure 2.1 can be compared directly to the phase diagram shown in Figure 2.2, reproduced from the ASM Handbook.

If such a plateau pressure of an isotherm is considered, then it can be further shown that

$$\Delta\mu_{H_2(\text{plat})} = RT \ln[p_{H_2(\text{plat})/\text{atm}}] = \Delta G^\circ \tag{2.1.3}$$

where $\Delta\mu_{H_2(\text{plat})}$ is the relative hydrogen potential at the plateau, $p_{H_2(\text{plat})}$ is the partial pressure of H_2 at the plateau, and ΔG° is the change in Gibbs free energy in the standard state. This leads to another form of the *van't Hoff* equation

$$\ln[p_{H_2(\text{plat})/\text{atm}}] = \frac{\Delta H^\circ}{RT} - \frac{\Delta S^\circ}{R} \tag{2.1.4}$$

which can be used directly to plot plateau pressures against temperatures in a straight line the slope of which corresponds to the enthalpy of formation of the hydride, as seen in Figure 2.3; the intercept corresponds to the entropy of formation.

2.2 Kinetics of Hydrogen Sorption

The kinetics of a hydrogen sorption material refers to the movement of hydrogen atoms during sorption and desorption; for the absorption step this

includes adsorption of hydrogen gas onto the surface of a material, dissociation of the hydrogen molecules into atomic hydrogen on the surface of the material, diffusion of hydrogen across the surface or through grain boundaries, and subsequent nucleation and growth of hydride particles or possible diffusion of hydrogen through a hydride layer; desorption includes the reverse of these steps.

The rate controlling step could be any one of these series, and could be different for absorption and desorption. In this study several of these steps were considered for optimization during material design.

2.2.1 Dissociation of Hydrogen Gas

Hydrogen must interact with the surface of a material before entering the bulk of the material; hydrogen enters the metal matrix only as single atoms, so it must first adsorb onto the surface as H_2 and then dissociate into two H atoms. This dissociation step can be a rate limiting step for magnesium: Riemann showed in 1933 that hydrogen gas absorbed much faster into magnesium when it was partially atomized with a tungsten filament than it would normally be[40]. Palladium has been shown to dramatically increase the rate of dissociation of H_2[41, 42], and has become commonly included in hydrogen storage systems as a catalyst to reduce or remove the limitations from the dissociation step [43, 44]. A palladium layer may also serve the purpose of preventing oxidation of the underlying material; magnesium, for example, readily oxidizes and the resulting MgO layer does not allow hydrogen diffusion and must be cracked or perforated to allow sorption [45]; furthermore, hydrogen reduces PdO [46], preventing oxidation of Pd from seriously impeding its use in a hydrogen storage material.

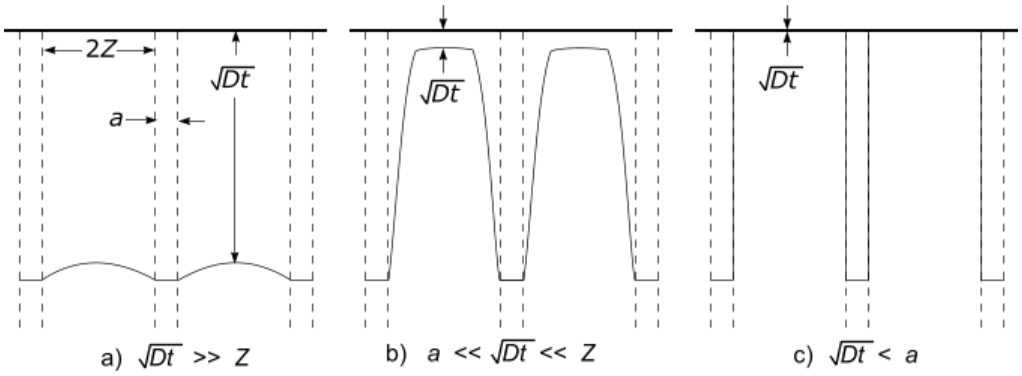

Figure 2.4: Diffusion profiles that develop between high-diffusivity-paths with various ratios of the diffusion distance in the lattice $\sqrt{Dt}$ to the separation Z, with the solute source at the top; adapted from Shewmon [47].

2.2.2 Bulk Diffusion

After dissociation on the surface of the material, hydrogen atoms must diffuse to wherever they will combine with magnesium to form a hydride; this involves diffusing along the surface, in grain boundaries or dislocations, or through the bulk material. Grain boundaries and dislocations serve as high-diffusivity-paths for hydrogen, and so most hydrogen travels through them [45, 47]; the resulting concentration profile of hydrogen within the bulk of the material depends on the ratio of the diffusion distance in the metal lattice, $\sqrt{Dt}$ where D is the diffusion coefficient and t is time, to the average separation of high-diffusivity-paths, Z. As shown in Figure 2.4, when the separation is large relative to the diffusion distance (case b), hydrogen does not diffuse to the midpoint nearly as easily as when the separation is relatively small (case a). Thus, in order to take less time for hydrogen to diffuse through the lattice, the average distance between grain boundaries and dislocations should be reduced; this essentially means that reduction in grain size, or grain refinement, will increase the speed of sorption. The average grain size can be altered in several ways, which will be discussed further in Section 2.3.

2.2.3 Nucleation and Growth

The process of transforming the bulk material to a hydride begins with the initial nucleation of hydride particles, and continues with the growth of those particles; this process is termed nucleation and growth. The concentration of particles initially nucleated can greatly affect the further growth of the hydride phase [1]; in the magnesium-hydrogen system, hydrogen diffuses much more rapidly through Mg than it does through MgH_2 - at 200°C, D_{HinMg} is ~10^{-9} m^2/s and D_{HinMgH_2} is ~10^{-19} m^2/s [48, 49]- and the nucleation of many particles can create a shell of MgH_2 through which hydrogen can diffuse only very slowly [45]. These differences in diffusion rates can make it difficult to determine a rate limiting step, as the hydriding rate is dependent upon the local concentration of hydrogen, which itself is dependent upon diffusion rates [1]. This can create a situation where additional driving force for hydriding can lead to slower overall absorption rates; at pressures above ~30 bar H_2 gas, magnesium absorbs hydrogen at a slower rate. Magnesium hydride has been shown to grow by migration of the hydride interface, fed by hydrogen diffusing along the phase interface rather than through the hydride layer [45]; this suggests that there should be an optimal initial nucleation concentration and grain size, to allow for fast, yet nearly-complete, hydrogenation of a grain.

2.3 Microstructure

There are several aspects of the microstructure of a hydrogen storage material which are important considerations, including the crystal structures of the various phases involved and their average grain sizes. The grain size is greatly affected by the method of material creation, and must further be prevented from changing dramatically through repeated hydrogen cycling.

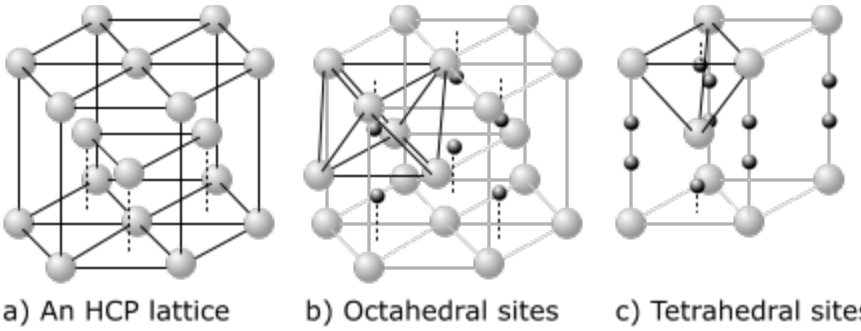

Figure 2.5: Atom positions in an Hexagonal Closed Packed lattice are shown in *a*; locations of interstitial sites are marked by smaller dark spheres, octahedral sites in *b* and tetragonal are shown in a segment of the previous lattices in *c*; adapted from Gross [1].

2.3.1 Crystal Structures

The crystal structures of the various phases of a hydrogen storage material are important both from structural effects within the phase and the interactions between phases. The crystal structure of magnesium is hexagonal close-packed (HCP), as shown in Figure 2.5a; within this structure there are several locations at which a hydrogen atom can sit interstitially - within the interstices of the lattice - and diffuse through the material by jumping between these sites. Beyond a fairly low concentration of hydrogen of less than 10 at.% (atomic percent), magnesium and hydrogen convert - at low temperatures and pressures - to α-MgH_2, which has a tetragonal structure [50, 51]; this phase is much slower, relatively, for hydrogen diffusion, as explained in Section 2.2.2.

The two materials utilized as alloying additions in this study were aluminum and titanium. The crystal structure of aluminum is face-centered cubic (FCC) which, also being a close-packed structure and having a similar size to Mg (being but one proton heavier), lends itself nicely to alloying substitutionally in low concentrations with magnesium, as shown in the Al-Mg phase diagram in Figure 2.7[52]. Titanium has a hexagonal-close-packed (HCP) structure,

which also allows it to be added substitutionally to the magnesium matrix, and has been shown to make metastable homogeneous alloys to fairly high concentrations of at least 20 at.%[53].

2.3.2 Reducing Grain Size

Due to the slow diffusion of hydrogen through magnesium hydride, geometric considerations become important, as explained in Section 2.2.2; as this means smaller grains are advantageous, reducing grain size becomes an important priority. Grain size is affected by the method of material fabrication, alloying additions, and other factors [54]; however, it is possible in many cases to create a material with very small grains that could be considered nanocrystalline (on the order of 1-100 nm in radius) simply by depositing a thin film of the metal, though the sizes are material dependent; this is achieved in large part due to the size restrictions of the thin film itself, and aided by low adatom mobility [55, 56]. Further grain refinement can be made with alloy additions. Size-mismatch of substitutional alloys will impede crystal growth, allowing more crystals to nucleate, resulting in more, smaller grains [57, 58].

2.3.3 Reducing Grain Growth

If a fine grained structure has been successfully created, retention of that structure throughout hydrogen cycling is critical. Grains will naturally grow in what is called normal grain growth, in which the average grain size d changes according to

$$d^2 - d_0^2 = ct \tag{2.3.1}$$

where d_0 is the average grain size at time zero and c being a strongly temperature dependent constant where $c = c_0 e^{-Q/kT}$ [56]. Grain growth is driven by the net reduction in free energy of grain boundaries, as increased grain size

results in net grain boundary area reductions; this defeats the advantage of having created a material with many high diffusivity paths.

During hydrogen cycling, however, grain growth is further driven by the increased temperatures at which these cycles are performed and recrystallization of grains transforming to and from hydrides; this results in nanocrystalline magnesium structures quickly agglomerating within 5 - 10 cycles into much larger grains [59, 60].

In the semiconductor field, grain growth is combatted using either grain boundary stuffing (where an element like nitrogen is used to passivate grain boundaries by reducing grain boundary diffusivity)[57, 61] or though alloy additions [62]. The latter technique holds promise in preventing agglomeration during hydrogen cycling from eliminating the advantage of creating nanocrystalline hydrogen storage materials.

2.4 Developing a Hydrogen Storage Alloy

The design of a hydrogen storage alloy must take into consideration a number of factors. The first and most obvious method of limiting choices is to consider the weight percentage of hydrogen stored; for mobile applications this is extremely important, and still worth considering for stationary applications. The list of binary metal-hydrides up to Zn shows that there are few that store above 5% hydrogen by weight (wt%); while metal-hydride target weight-percentages have been changing during the last half decade, most are focused above 5% due to existing technologies - such as compressed hydrogen tanks - holding large fractions of this, up to 4 weight% [14, 28].

The next major criterion which must be considered is the thermodynamic stability of the hydride, as this dictates the temperatures and pressures at which the hydrogen storage material must operate. Figure 2.6 shows a *van't Hoff* plot

Element A	Atomic Mass	AH_x	Hydride	Hydrogen wt%	ΔH (kJ/mol) [63]
Li	6.941	1	LiH	12.68%	-180
Be	9.012	2	BeH_2	18.28%	~0
B	10.811	3	BH_3	21.86%	-8
Na	22.990	1	NaH	4.20%	-112
Mg	24.305	2	MgH_2	7.66%	-74
Al	26.982	3	AlH_3	10.08%	-8
K	39.098	1	KH	2.51%	-116
Ca	40.078	2	CaH_2	4.79%	-188
Sc	44.956	2	ScH_2	4.29%	-200
Ti	47.880	2	TiH_2	4.04%	-136
V	50.942	2	VH_2	3.81%	-40
Cr	51.996	1	CrH	1.90%	-12
Mn	54.847	0.82	$MnH_{0.82}$	1.48%	-16
Fe	55.847	~0	-	0%	-
Co	58.933	0.51	$CoH_{0.51}$	0.86%	+30
Ni	58.693	1	NiH	1.69%	-9
Cu	63.546	1	CuH	1.56%	-
Zn	65.39	2	ZnH_2	2.99%	-

Table 2.1: A list of elemental metals up to Zn, their respective binary hydrides and hydrogen capacities, along with their enthalpies of hydride formation; enthalpies and hydrogen ratios taken from Herbst.[63]

Compound AB	Atomic Mass	ABH_x	Hydride	Hydrogen wt%	ΔH (kJ/mol) [63]
$LaNi_5$	432.371	6.7	$LaNi_5Hi_{6.7}$	1.54%	-30
Mg_2Ni	107.303	4	Mg_2NiH_4	3.62%	-64
Mg_2Fe	104.457	6	Mg_2FeH_6	5.47%	-79
FeTi	103.727	1.6	$FeTiH_{1.6}$	1.53%	-34
YNi_3	264.985	4	YNi_3h_4	1.50%	-46

Table 2.2: Selected ternary hydrides: hydrogen capacities and enthalpies of hydride formation; enthalpies and hydrogen ratios taken from Herbst [63].

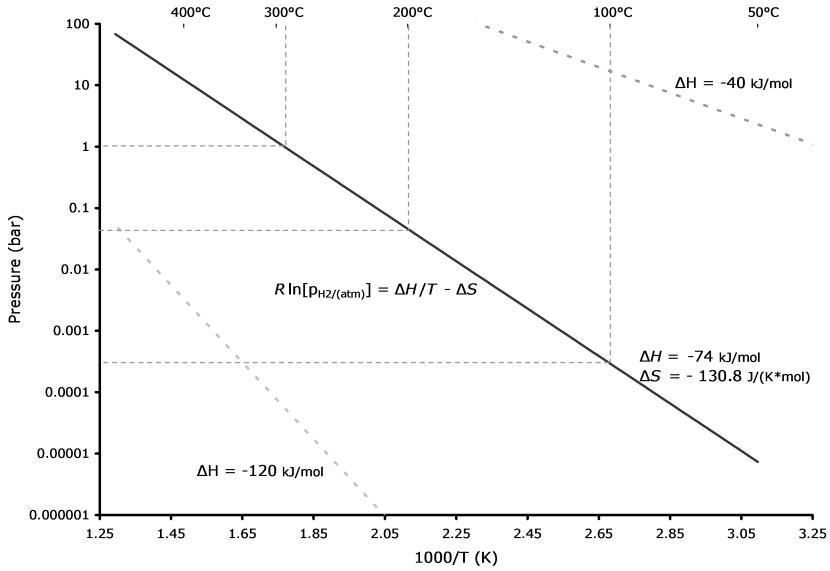

Figure 2.6: A *van't Hoff* Plot using $\Delta H = -74$ kJ/mol [63] and $\Delta S = -130.8$ JK^{-1}/mol [35], illustrating the relationship between operating temperature and pressures.

for Mg, which has an enthalpy of hydride formation (ΔH) of -74 kJ/mol, and lines of -120 kJ/mol and -40 kJ/mol are shown in dashed lines: From these, the relation between enthalpy of hydride formation, and operating temperature and pressure can be clearly seen. Anything more stable (more negative ΔH) than Mg quickly requires either very high temperatures or very low pressures, while any much less stable (less negative) than -40 kJ/mol requires very high pressures, or low temperatures; indeed -40 kJ/mol falls closest to the desired operating temperatures and pressures listed in many proposals, sometimes proposed as between -25 and -60 kJ/mol[13]. When comparing the desired ΔH to elements with hydrogen weight percentages above 5%, Mg is the closest to this criterion.

Comparing MgH_2 which has a weight percentage of 7.66 and a ΔH of -74 kJ/mol to several of the more popular ternary metal hydrides, listed in Figure 2.2, it is apparent that any advantages in enthalpy of formation are opposed by disadvantages of low weight percentages [1]. Furthermore, some of them contain very expensive elements, such as La, or elements that are difficult to work with, or which have even higher affinity for oxidation than Mg[28]; Mg has the additional benefit of being both inexpensive and in common use in alloys and other areas of industry [1, 13, 28]. For these and the aforementioned reasons, the magnesium - magnesium hydride system is a logical choice as a base storage material.

2.4.1 Alloy Additions

Having chosen a base hydrogen storage system, Mg to MgH_2, the issues of reducing grain size and reducing grain coarsening through alloy addition, as outlined in Sections 2.3.2 and 2.3.3, should be discussed. The basic idea is that through alloy additions, grain size may be reduced, and may also be prevented from increasing in size, again through alloy additions.

Element	Crystal Structure	Forms Intermetallic(s) with Mg	Issues
Be	hcp	-	expensive
Al	fcc	Many	-
Ca	fcc	Yes	-
Sc	hcp	Yes	-
Ti	hcp	No	-
Co	hcp	Yes	heavy
Ni	fcc	Yes	heavy
Cu	fcc	Many	heavy

Table 2.3: A list of elements lighter than Zn that are close packed, with their interactions with Mg listed.

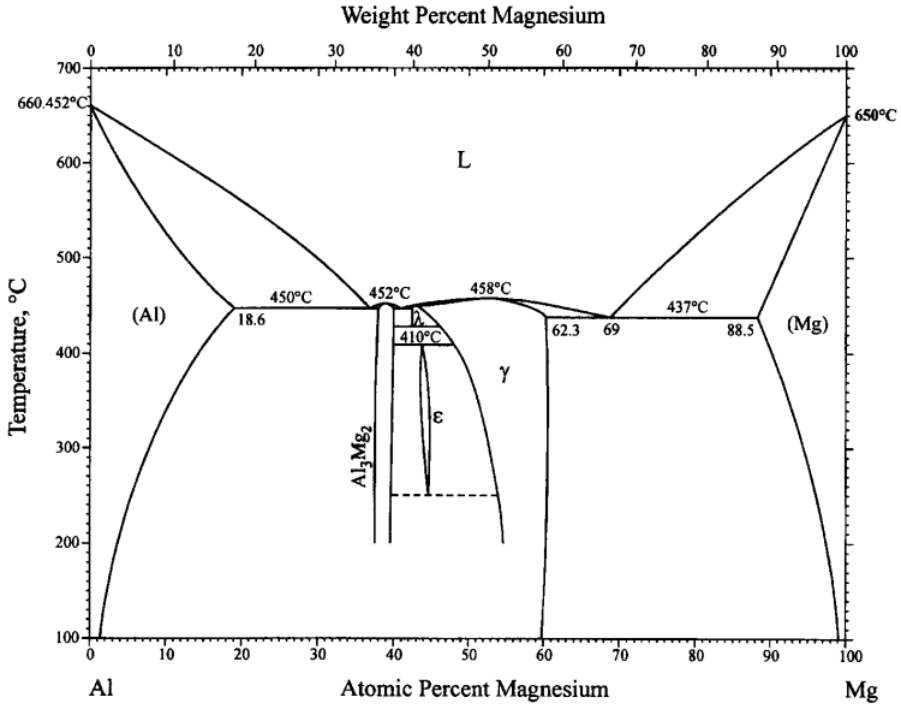

Figure 2.7: The Mg-Al phase diagram, Okamoto [52].

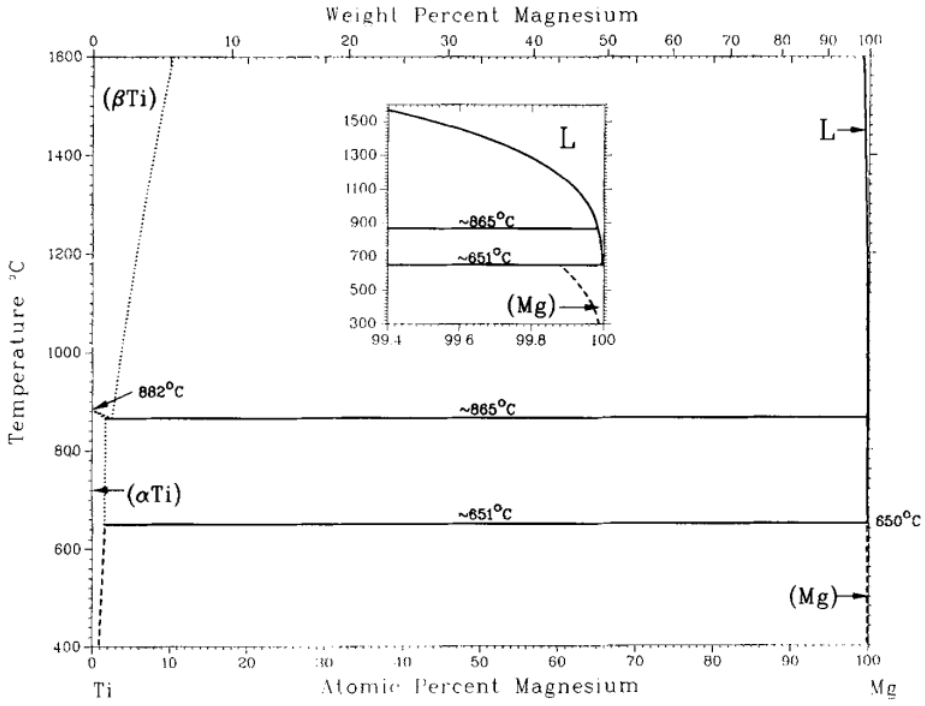

Figure 2.8: The Mg-Ti phase diagram, Murray [64].

Choosing alloy additions in order to achieve the desired grain size reduction is similar to the design of Bulk Metallic Glasses (BMG) in terms of the desire to avoid large crystallites from forming [67]. Like bulk metallic glasses, one of the primary criteria is that the alloying addition has a large negative heat of mixing, $\Delta H_{(mix)}$ or heat of formation, with Mg, meaning that the two will create one or more intermetallics upon mixing, releasing energy in the process. As the intended use is in a hydrogen storage system, alloy additions should take reactivity with hydrogen into account, preferably not having a more stable hydride than Mg, or having one that will not form as readily as MgH_2. Furthermore, as hydrogen storage in terms of weight percent is a concern, lighter metals should be considered, so as to not reduce the overall hydrogen weight% too significantly. This also relates to the criterion laid out in Section 2.3.1, which called for a slight size-mismatch, as Mg is one of the lighter elements, other light elements should be relatively close in size; this,

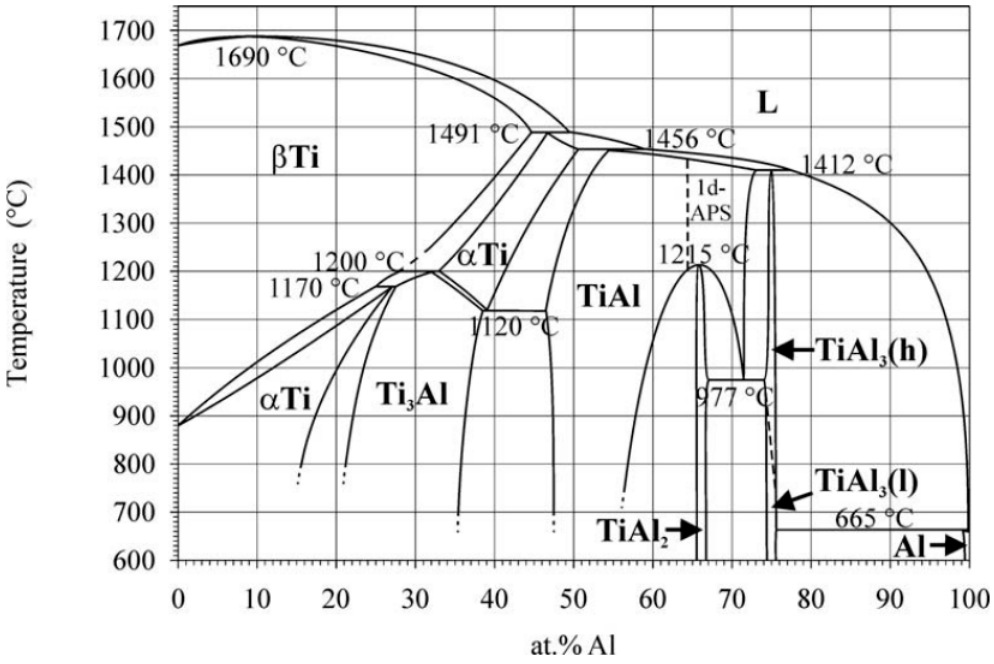

Figure 2.9: The Al-Ti phase diagram, Schuster [65].

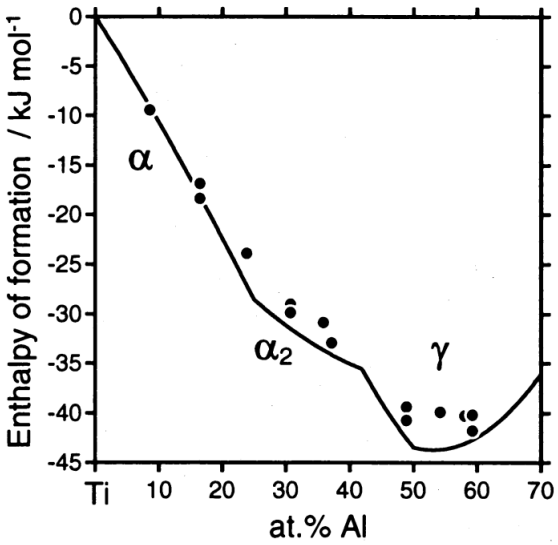

Figure 2.10: Enthalpies of formation of Al-Ti intermetallics at 298K, Ohnuma [66].

however, also requires that the alloying element have a crystal structure similar to magnesium, which has an HCP structure.

The list of elements in Table 2.3 shows possible combinations of light metals with close-packed structures; the obvious choice is Al, which is both light, forms intermetallics with Mg, and, referring to Table 2.1, has an enthalpy of hydride formation of -8 kJ/mol. The Mg-Al phase diagram, Figure 2.7, shows a number of intermetallics; Herbst lists several intermetallics and their heats of formation: $Mg_{17}Al_{12}$ with a $\Delta H_{(mix)}$ of -14 kJ/mol, Mg_2Al_3 with a $\Delta H_{(mix)}$ of -13 kJ/mol, and $MgAl_2$ with a $\Delta H_{(mix)}$ of -7 kJ/mol [63]; furthermore, these have hydrides associated with them, $Mg_{17}Al_{12}H_{24.9}$ with a $\Delta H_{(mix)}$ of -74 kJ/mol, Mg_2Al_3 $H_{4.4}$ with a $\Delta H_{(mix)}$ of -56 kJ/mol, and $MgAl_2$ H_8 with a $\Delta H_{(mix)}$ of +13 kJ/mol [63]; these intermetallic hydrides may be negligible to the hydrogen storage material however.

When considering a choice for a second alloy addition to further frustrate grain coarsening, what is desired is an element that does not form intermetallics with the host metal, but does with the first alloy addition, and which is also close-packed; choosing Ti first as the only light element on the list not forming intermetallics as can be seen in its phase diagram, Figure 2.8, its interactions with Al must be considered. Fortunately, Al and Ti form intermetallics as seen in the Al-Ti phase diagram, Figure 2.9, including Ti_3Al, TiAl, $TiAl_2$, and $TiAl_3$. Ti also forms a hydride, with a ΔH of -136 kJ/mol, as shown in Table 2.1; referring back to Figure 2.6, one can see that this can easily form thermodynamically in the main operating zone of MgH_2; however, in that temperature range, it is possible that it will be kinetically limited.

Following this reasoning, Mg with Al was chosen as a candidate as a hydrogen storage alloy; MgAl with Ti was subsequently chosen as a potentially better candidate. In order determine the potential benefits of these alloy additions on the hydrogen sorption behaviour of the material, a broad range of alloy additions was chosen to be studied, focusing on the magnesium rich end so

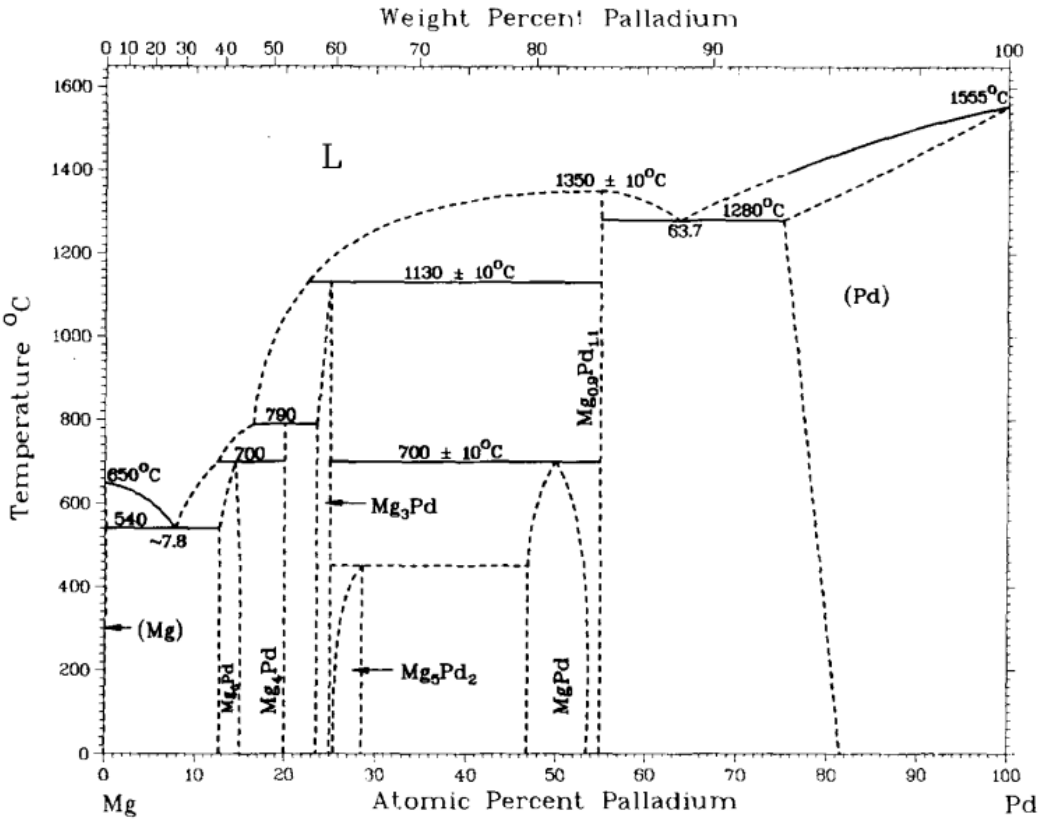

Figure 2.11: The Mg-Pd phase diagram, reproduced from Nayeb-Hashemi [68].

as to diminish the lowering of the maximum theoretical weight percentages of hydrogen storage.

Within the range of magnesium compositions to be studied in the MgAlTi system was the range of Al-Ti ratios available to be chosen; as the Al-Ti system has four main intermetallics, the ratios corresponding to those intermetallics, namely Al:Ti ratios of 3:1, 2:1, 1:1 and 1:3, were chosen; their enthalpies of formation, shown in Figure 2.10 indicate that around the 1:1 ratio Al and Ti will have strongest affinity for each other [66].

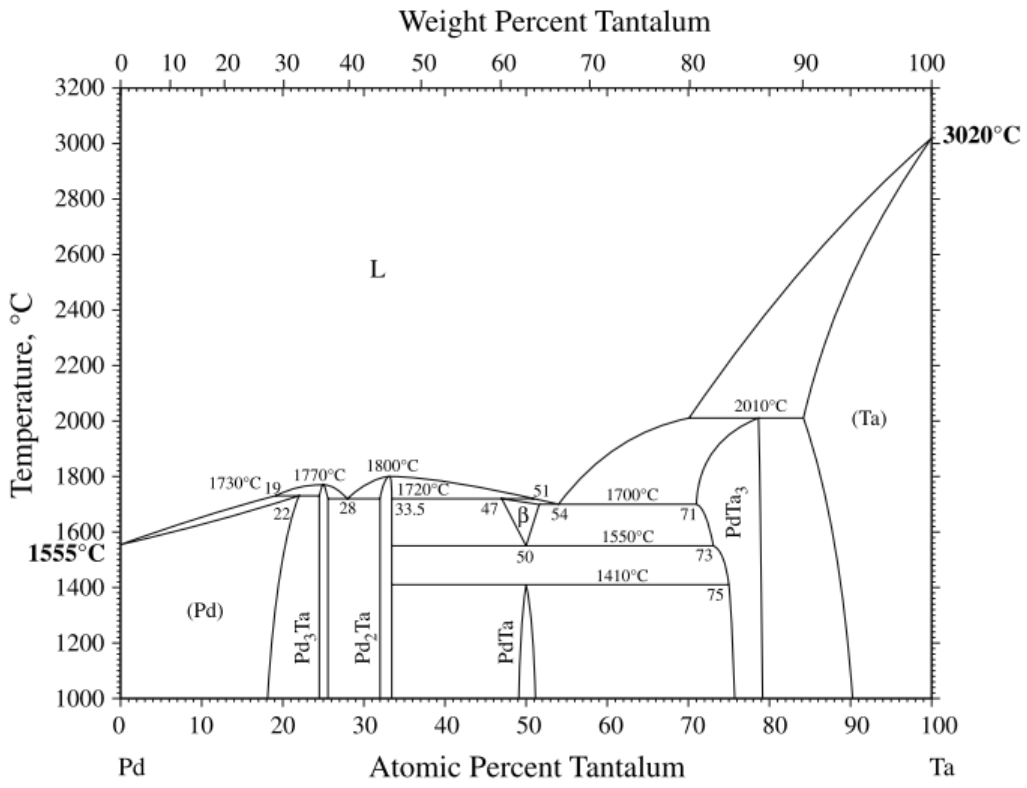

Figure 2.12: The Pd-Ta phase diagram, reproduced from Okamoto [69].

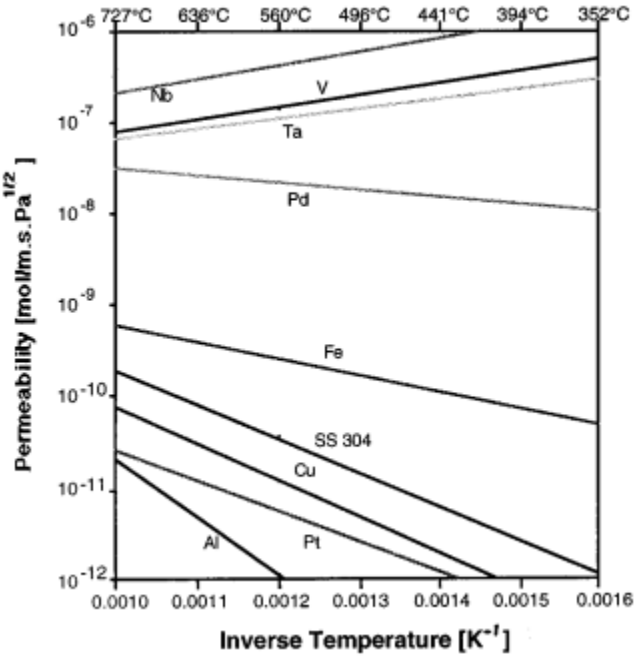

Figure 2.13: Hydrogen permeability of various metals; reproduced from Buxbaum [70].

2.4.2 Catalytic Layers

Having determined the hydrogen storage materials to be studied, the issue of a catalytic layer for dissociation must be addressed. As discussed in Section 2.2.1, Pd is well known as a catalyst for hydrogen dissociation and permeability to hydrogen and is often used in hydrogen applications. As palladium's surface properties are its primary desirable trait, the thickness of Pd used as a catalyst should be minimized, as it is both an expensive element and it will contribute negatively to the weight percentage of the material. However, as mentioned in Section 2.2.1, Pd also has the desirable property of oxidizing much less readily than Mg; it is thus possible to use it as a barrier to oxidation of magnesium. Therefore, it can be decided that the smallest Pd layer that should be used should be around where it will become a continuous film; while complete coating may not be completely necessary to eliminate oxygen

[71], it would prevent the undesirable accumulation of magnesium oxide. To determine the thickness to be used, an experiment using pure Mg with various thicknesses of Pd layers was designed; a film thickness of 1 nm was considered unlikely to be continuous, while 50 nm was considered to almost certainly be continuous (given the commonality of sputtering similarly dimensioned films); intermediate thicknesses would be tested (Section 5.1.2) to determine a final catalytic layer thickness.

The criterion of cycling stability resulted in an addition to the catalytic layer. Magnesium and palladium form several intermetallics on the magnesium-rich end of the phase diagram, Figure 2.11, including Mg_6Pd, Mg_4Pd, Mg_3Pd, and Mg_5Pd_2 [68], and at elevated temperatures of 200°C(473K) - which are a significant fraction of magnesium's melting point of 650°C(923K) - these are quite likely to form, especially considering that both Mg and Pd will be undergoing phase transformations to and from their respective hydrides during cycling. This would result in the slow dissolution and diffusion of the Pd layer into the Mg bulk, eliminating it as a catalyst layer and reducing the overall storage capacity of the system. The solution to this problem is to introduce a second layer between the Pd and Mg that inhibits the diffusion of those elements, yet does not inhibit hydrogen diffusion.

Tantalum (Ta) is a material commonly used with Pd in hydrogen applications such as gas separation [70, 72] as it has a high hydrogen permeability relative to Pd [73], as seen in Figure 2.13, and furthermore is resistant to oxidation. While Ta does form intermetallics with Pd, as seen in their phase diagram in Figure 2.12, the melting point of Ta, a refractory metal, is extremely high at 3290 K, so it is unlikely to diffuse or form intermetallics at the relatively low temperatures of 573 K; the Mg-Ta phase diagram is unexplored, but any possible intermetallics are unlikely to be formed at lower temperatures.

As Ta is a very heavy element at 180.95 g/mol and will consequently contribute fairly significantly to the total weight of the material even as only a thin layer;

Element	Molar Weight (g/mol)	Molar Volume (cm^3/mol)
Mg	24.305	14.00
Al	26.9815386	10.00
Ti	47.867	10.64
Pd	106.42	8.56
Ta	180.94788	10.85
H	1.00794	-

Table 2.4: A list of elements used in this study, their molar weights and molar volumes.

however, as it is capable of fulfilling part of the function of Pd, in that it does not oxidize and can prevent oxidation of the Mg surface, it was decided that the Ta film could simply replace half the Pd film; this was after confirmation (by neutron reflectometry, Section 5.1.4) that the Pd film was continuous and low in roughness, suggesting that halving its thickness would be possible without unduly affecting the surface characteristics.

2.4.3 Theoretical Maximum Storage Capacity

Having chosen several hydrogen storage materials, their theoretical hydrogen storage capacities should be investigated, both as the base material and as the catalyzed material actually tested, the first being of interest from an application standpoint and the latter as limits on actual experiments.

Hydrogen storage capacity as a weight percentage is calculated as the mass of the hydrogen stored divided by the total mass of the material in its fully hydrided state. As magnesium based materials, it is considered that only Mg will store hydrogen, and any other hydrides (like TiH_2 or tantalum hydrides) are non-reversible at operating conditions. For the base materials this makes calculating the maximum hydrogen storage a simple function; for $Mg_xAl_yTi_z$

Mg%	Al%	Ti%	Base H% (wt)	Overall H% (wt)	Caps Mass Frac.
100	0	0	7.7	6.9	10.6
90	10	0	6.9	6.2	10.5
85	11.25	3.75	6.3	5.7	10.1
85	10	5	6.2	5.6	10.0
85	7.5	7.5	6.1	5.6	9.9
80	20	0	6.1	5.5	10.4
85	3.75	11.25	6.0	5.4	9.6
70	30	0	5.3	4.8	10.3
70	22.5	7.5	5.0	4.6	9.7
70	20	10	4.9	4.5	9.6
70	15	15	4.8	4.3	9.2
60	40	0	4.5	4.1	10.2
70	7.5	22.5	4.5	4.1	8.8
60	30	10	4.2	3.8	9.5
60	20	20	3.9	3.6	8.9
60	10	30	3.7	3.4	8.3

Table 2.5: Base material hydrogen storage capacity, overall hydrogen storage capacity (including catalytic capping layers), and mass fraction of the capping layers of non-hydrided material of selected compositions.

the total hydrogen storage capacity H% (wt) is

$$\text{H\% (wt)} = \frac{2xM_H}{xM_{Mg} + yM_{Al} + zM_{Ti}} \tag{2.4.1}$$

where each M is the molar weight of each respective element, listed in Table 2.4.

Hydrogen storage capacity of complete films as used in experiments, however, must take into account the additional mass of the Pd and Ta layers; thus to reduce the effect of the capping layers upon overall storage capacity the thickness of the bulk material should be large relative to the thickness of the capping layers. The majority of the films in this study were free-standing films capped on both sides with 7.5nm of Pd and 7.5nm of Ta; main material thicknesses were 1.5μm - a figure arrived at after considering the time required for sputtering (less than an hour), the number of samples that could be created out of a sputter target (around 10) and the mass of base material created on a standard 4-inch wafer (greater than 20μg). Using this geometry one can calculate the overall hydrogen storage capacity by multiplying each element by the relative thicknesses of the layers and its percentage within those layers. The base material storage capacity, overall hydrogen storage capacity, and mass fraction of the capping layers compared to the non-hydrided material of various compositions spanning this study are presented in Table 2.5.

2.4.4 Theoretical Sorption and Desorption Models

Sorption of a material begins with the adsorption of hydrogen to the surface of the material and dissociation of the hydrogen gas (Section 2.2.1), followed by the formation of a metal hydride during nucleation and growth (Section 2.2.3). The characteristics of the sorption kinetics of a particular material are governed by which step is the rate-limiting step; the shape of the sorption curve can thus qualitatively indicate the rate limiting step of the reaction [74]. There

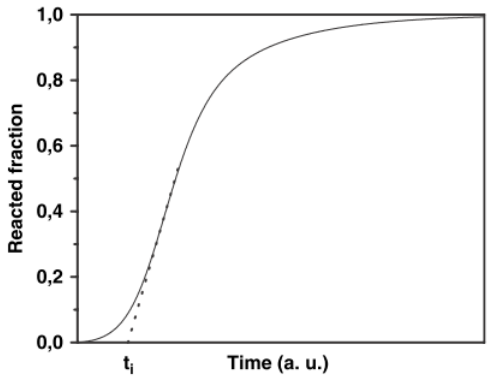

Figure 2.14: A kinetic curve displaying Kolmogorov-Johnson-Mehl-Avrami (KJMA) characteristics for dimensionality $n = 2,3$; the values of k have been scaled independently.

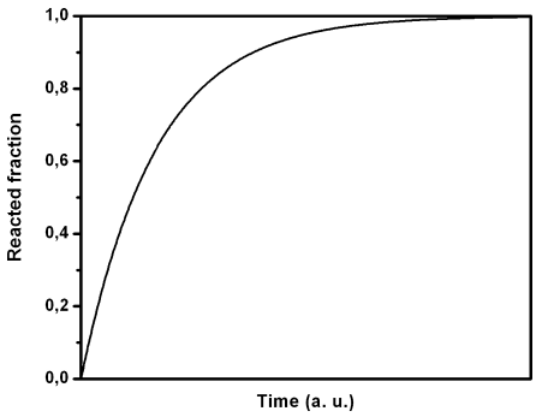

Figure 2.15: A kinetic curve displaying contracting volume (CV) characteristics for dimensionality $n = 2,3$; the values of k have been scaled independently.

are three main models to describe the kinetic steps involved in sorption:[74, 75] Surface reaction, Kolmogorov-Johnson-Mehl-Avrami or KJMA, and contracting volume or CV. We may express the various model shape mathematically using the reacted fraction of the material, α, versus time, t, with a dimensionality of growth, n, also known as the Avrami exponent.[28]

Surface reactions refer primarily to the chemisorption of hydrogen, as in the absorption of hydrogen into the metal lattice, resulting in a reacted fraction that is linear with time, which can be expressed as [74]:

$$\alpha = kt \tag{2.4.2}$$

Absorption curves appearing to be linear in nature are indicative of a rate-limiting surface reaction.

Both the KJMA and CV models describe the nucleation and growth steps; both models depend on the dimensionality of growth, n. The KJMA model assumes nucleation and growth occur randomly in the material and describes the process as [74]:

$$[-\ln(1-\alpha)]^{1/n} = kt \tag{2.4.3}$$

which yields the characteristic sigmoidal curves shown in Figure 2.14; the 3-dimensional ($n = 3$) model is easiest to visualize as hydride grains randomly nucleating and growing within a larger spherical particle; an example of a 2-dimensional model ($n = 2$) could be plate-like particles being hydrided, where there is no significant third dimension. The sigmoidal shape implies that the nucleation step is slow; this is common of first hydrogenation[74]. The intersection of the slope of the inflexion point and the x-axis is known as the incubation time (t_i).

The CV model assumes nucleation of grains occurs at the surface of a particle, growing inwards. This process is described by [74]:

$$1 - (1-\alpha)^{1/n} = kt \tag{2.4.4}$$

which yields characteristics shown in Figure 2.15; both models are relatively easy to visualize, the 3-dimensional l ($n = 3$) model being that of surface particles growing inwards eventually to form a continuous layer which continues to contract inwards, whence the model gets its name; an example of a 2-dimensional model ($n = 2$) is similar, but with a plate and in two dimensions; this is occasionally described as contracting area [76].

2.5 Theory of Experimental Methods

In order to properly understand results, it is necessary to have a basic understanding of the underlying theory behind the methods used to create and characterize the materials in question. The following section has brief descriptions of the methods used to characterize and create the materials in this study.

2.5.1 Physical Vapour Deposition (Sputtering)

Physical Vapour Deposition, or Sputtering, is a process whereby a vapour of individual high-energy atoms is created and allowed to deposit onto a substrate, as in Figure 2.16; this can result in extremely high purity films of a material, and the ability to mix various materials in ratios that would not naturally form through traditional alloying methods. This high-energy vapour is created by accelerating ionized gas, typically argon, towards a "target" of the desired deposition material, via an applied voltage on the target. Conservation of momentum causes atoms from the target to be ejected in the opposite direction; in the high-density configuration used the targets are in "guns" which are aimed at the target; a "gun", as shown in Figure 2.17, consists of a target material, to which a negative DC voltage is applied, a grounded shield above the edges of the targets, and sets of magnets below around the edge, with a

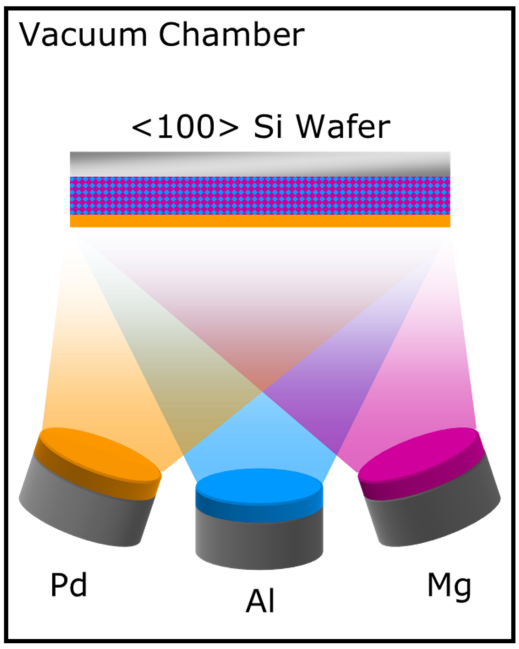

Figure 2.16: The basic layout and orientation of sputtering; In this example, an MgAl film with a Pd layer on top, the Mg and Al guns would be active at the same times with relative powers calculated to yield a certain ratio of Mg to Al; the Pd gun would be inactive during this time and then become active at following the Mg and Al deposition.

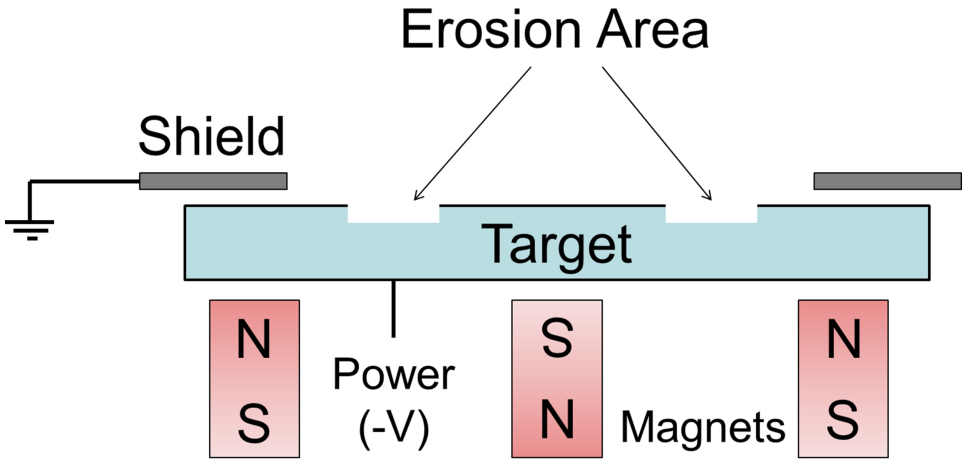

Figure 2.17: A cross section of a sputter gun.

set in the centre in opposition to the edge magnets[57]. This causes magnetic field lines to curve down towards the target; the electrons which flow when the breakdown voltage is exceeded spiral around the magnetic field lines, increasing the probability that they will collide with neutral gas and create ions, which in turn increases the bombardment rate of the target by accelerated ions and thus the rate of sputtered target atoms. Sputtered atoms tend to have energies of 10 to 50 eV, which allows for great surface mobility when arriving at the substrate[57].

The rate of sputtering is calibrated to a power curve, so that for a given input power a certain sputter rate, typically expressed in Å/s, may be calculated for a given target and gun. Calculating points to create the calibration curve was done using a thickness monitor, which has an oscillating piezoelectric crystal, the resonant frequency of which changes based on the deposited material; by inputting the density of the material and its acoustical properties, the thickness of deposited material may be calculated (automatically by the thickness monitor in our setup); by doing a deposition at a certain power for a specified time, a rate may be obtained. Then, by using the deposition rates and the density of the material being sputtered, the sputter rates required to create a material with a certain atomic ratio of different materials may be calculated, for example 80Mg20Al or 70Mg15Al15T, using the following relation:

$$material_A\% = \frac{R_A/\rho A}{R_A/\rho A + R_B/\rho B} \tag{2.5.1}$$

where R is the rate of deposition and ρ is the density of this material; in this case both densities are standard values, and the deposition rate of material B is fixed, so the deposition rate of A may be easily calculated; this can be extended to multiple elements relatively easily.

2.5.2 Scanning Electron Microscopy

Scanning Electron Microscopy, or SEM, is a technique for imaging objects, such as a film of deposited material, at the sub-micron scale, or 10^{-6} meters[77]. Using an electron beam to raster across the surface of an object, back-scattered, or secondary, electrons are collected to produce an image of the surface features of the object; the surface must be electrically conductive, which is inherent in the metal films in these studies[77]. SEM's typically have an energy dispersive x-ray spectroscopy capability, or EDXS, which collects and analyzes the x-rays produced by an electron beam bombarding the surface, to identify chemical species; the depth of analysis is typically $1-3\mu$m, and thus analyzes the bulk and substrate[78], and was used to verify the sputtered ratio of elements - such as 70Mg30Al - was as expected.

2.5.3 X-Ray Diffraction

X-Ray Diffraction, or XRD, is a technique where a collimated beam of x-rays is targetted on a sample[79]; the ordered planes of atoms in a crystalline structure of a material causes the x-rays to diffract according to *Bragg's* Law:

$$n\lambda = 2d\sin\theta \tag{2.5.2}$$

where λ is the wavelength of the x-rays, θ is the diffraction angle, and d is the distance between crystal planes; as crystals can have planes of different distance depending on the orientation, and different species of atoms have differing sizes, this leads to a characteristic set of diffraction angles for different materials which allow identification of the crystal species within the material[78].

Typical X-Ray Diffractometer setups involve either a small area-detector or a

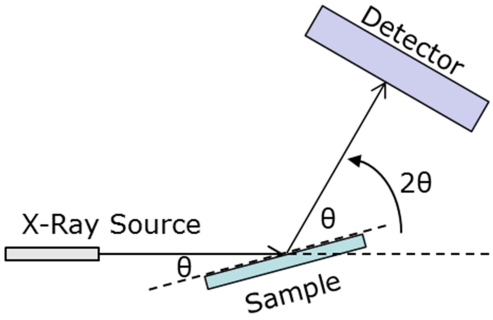

Figure 2.18: A typical setup of an X-Ray Diffractometer: the sample is at an angle θ with respect to the source, and the detector is at an angle 2θ with respect to the source.

point-detector that move relative to a source and sample so that the detector is constantly at twice the angle from the source as the sample is, in the 2θ condition[78]. The detectors count x-ray events and produce a scan over 2θ space, which may then be compared to reference values in databases.

2.5.4 Neutron Reflectometry

Neutron Reflectometry, or NR, is a materials characterization technique which uses a neutron beam to determine the structure and nature of layers in a thin film, with sub-nanometer resolution to a depth of 300nm[80]. Neutrons are reflected off the surface of a film and at interfaces of layers of materials with different refractive indices, such as the difference between a Pd capping layer and an MgAl layer, or between an MgAl layer and its Si substrate.

The setup of a neutron reflectometer, shown in Figure 2.19, requires a source of thermal neutrons (in this case a nuclear reactor), which are frequency selected and subsequently constrained into a narrow beam, which is reflected off the sample towards a neutron detector, which rotates along with the sample at an angle expressed in reciprocal space as q.

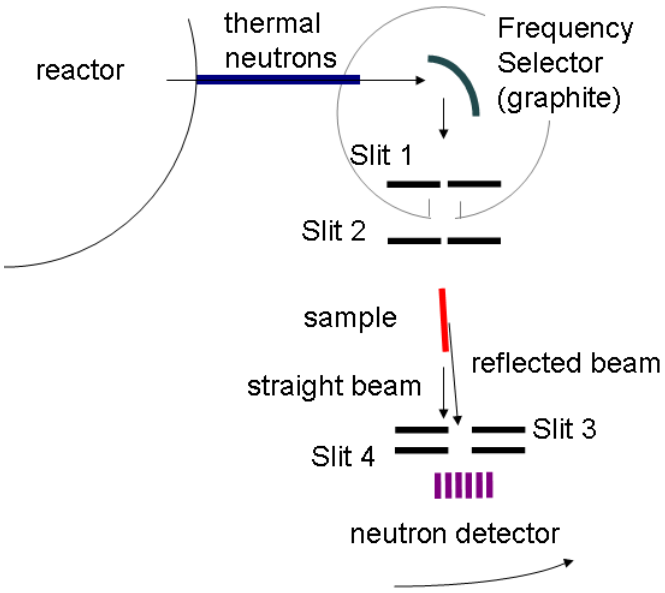

Figure 2.19: The setup of the D3 reflectometer at the Neutron Research Reactor NRU in Chalk River, Ontario; two slits are used to constrain the beam in two dimensions.

The recorded reflections produce a series of oscillations, in this case from $q = 0$ to $q = 0.1\text{Å}^{-1}$, known as Kiessig oscillations, which generally correspond to the characteristic thicknesses within the sample; they also contain information about the scattering length density (SLD) of the layers within the material, which is effectively the coherent nuclear scattering length, b, times density ρ, which is dependent on the elements and isotopes in the material. The Parratt recursion algorithm can be used to fit a layer model by adjusting the layer thickness and SLD, as well as the roughness of the interface between layers[80, 81]. This reveals a profile of the scattering length density with depth.

As the layer model finds the SLD of the individual layers, and the SLD is dependant upon the elements within that layer, information about composition can be obtained; specifically, for the case of MgAl in hydrogenated (or hydrided) and unhydrogenated states, the following relation may be used:

$$\text{SLD} = \rho N_A \frac{(1-x)b_{Mg} + xb_{Al} + yb_H}{(1-x)u_{Mg} + ub_{Al} + ub_H} \tag{2.5.3}$$

where N_A is Avogadro's constant, and u_{Mg}, u_{Al}, and u_H are the molar weights of Mg, Al and H[80]; between the two states, hydrogenated and unhydrogenated, the relative composition of each element may be determined. As the film expands, the density ρ changes; it is thus assumed that density change is inversely proportional to film thickness.

2.5.5 DSC-TGA

Differential scanning calorimetry, or DSC, and Thermogravimetric Analysis, (TGA), are two techniques for analyzing a sample in an inert atmosphere while varying temperature; in DSC, the temperature of the sample and its sample cup are compared to that of an empty sample cup; in this way, the temperature differences can be correlated to the mass of the sample, and heat flows - such as enthalpies of reaction during a phase change from a hydrided to unhydrided phase - may be observed[82]. TGA uses balance arms to measure the weight of the sample while the temperature changes, allowing slight weight changes to be correlated with temperature, for example the release of hydrogen from a metallic hydride causing the weight to drop. The two can be combined into a unified instrument, a DSC-TGA, in order to measure these properties on the same sample simultaneously. This involves having two balance arms in an inert atmosphere, with temperature probes below each of two sample cups, which may be compared to each other. The sample cups are made of a material which will not react with the sample material, like alumina or platinum; an inert gas, like Ar, is flowed during desorption so as to avoid a reaction with the materials, while transporting hydrogen away; in the machine used, this was limited to ambient pressure. DSC measures heat flow from the sample during a heating ramp, and is a common method used in determining absorption and

desorption temperatures [83], while TGA allows direct measurement of the mass-fraction of hydrogen absorbed or desorbed [84].

2.5.6 HPDSC

HPDSC, or High Pressure Differential Scanning Calorimetry, is essentially the same as the DSC portion of DSC-TGA but with the ability to adjust the pressure from vacuum to many atmospheres. As explained in Section 2.1, the *van't Hoff* equation can be used with several points of desorption plotted with pressure against temperature to determine the enthalpy and entropy of formation of the hydride. This is useful to verify the species of hydride was that which is expected, and to determine if any chemical optimization occurred.

2.5.7 Sieverts Apparatus

The Sieverts Apparatus is a system designed to allow the repeated testing of hydriding and dehydriding, in order to determine the absorption behaviour with respect to time, and the amount of hydrogen absorbed by a sample, typically expressed in weight percentage, as in the weight of hydrogen absorbed over the weight of the unhydrided sample. The sample is put in a known volume and vacuumed out; another known volume is pressurized to some level; and then the two volumes are opened to each other, with the total volume (including the gas lines) being known. With the expected equilibrium pressure before absorption being calculable, and pressure being monitored precisely, the weight of hydrogen absorbed by the sample can be determined using the molar mass of hydrogen and the ideal gas law; by knowing the weight of the sample beforehand, the weight percentage of hydrogen absorbed is thus calculable. This can be plotted against time to determine kinetic information, as described in Section 2.4.4.

3

Literature Review

3.1 MgAl

During the course of this study the material in literature relating to MgAl based hydrogen storage materials has developed at a steady rate; while there was already a body of research on MgAl hydrogen storage compounds at the beginning of the study, and since then a review of the field has been published. The research relevant to the MgAl results in this study will be reviewed, focusing on the review of MgAl by Andreasen.

Andreasen's review examines the various aspects of creating and testing a hydrogen storage material with relation to MgAl. As commercial alloys with de-

sired compositions are typically not available, the materials under study must first be created; the creation of alloys with desired compositions is typically done via ball-milling, although arc-melting has been used in some studies.[28] Ball-milling for short periods with low Al content yields a mixture of hcp Mg and fcc Al, giving way to γ-phase MgAl, which is $Mg_{17}Al_{12}$ or $Mg_{58}Al_{42}$, and increasing this Al content changes the produced first to β-phase MgAl - Mg_2Al_3 - and finally an fcc solid solution of Mg in Al.[28, 31]

Hydrogenation of MgAl has been focused almost entirely on MgH_2; AlH_3 is not seen, as it cannot form during absorption due to the temperatures at which MgAl is absorbed exceeding its decomposition temperature of approximately 150°C;[28] Magnesium alanate, or $Mg(AlH_4)_2$, which had received attention due to its high gravimetric storage of 9.3%,[85] has been observed only in reactions utilizing a hydrogen plasma, and not in any of the more common hydrogenation methods.[28] MgH_2 has a theoretical gravimetric capacity of 7.6%, and as alloying additions do not contribute to hydrogen storage, this is necessarily lowered by alloying.

The value found for the enthalpy of hydride formation of MgH_2 by Zeng et al.[86] was in the expected range, at -77.5 kJ/mol; enthalpies of formation of hydrogenated MgAl were found to have been modified by the alloying process, with values of -77.7 kJ/mol and even -62.7 kJ/mol having been found, as seen in the van't Hoff plot in Figure 3.1[28]. In general these studies found a lowering of the desorption temperature needed compared to pure Mg[28].

Kinetic studies were also performed, using the KJMA approach, which found an Avrami exponent of 1/2, which is interpreted as diffusion-limited one-dimensional growth.[28] This had also been proposed as a result of consistent hydrogenation data across a wide range of compositions.[28, 31] Kinetics generally were found to be improved with the addition of Al to the Mg system, in both absorption and desorption.[28]

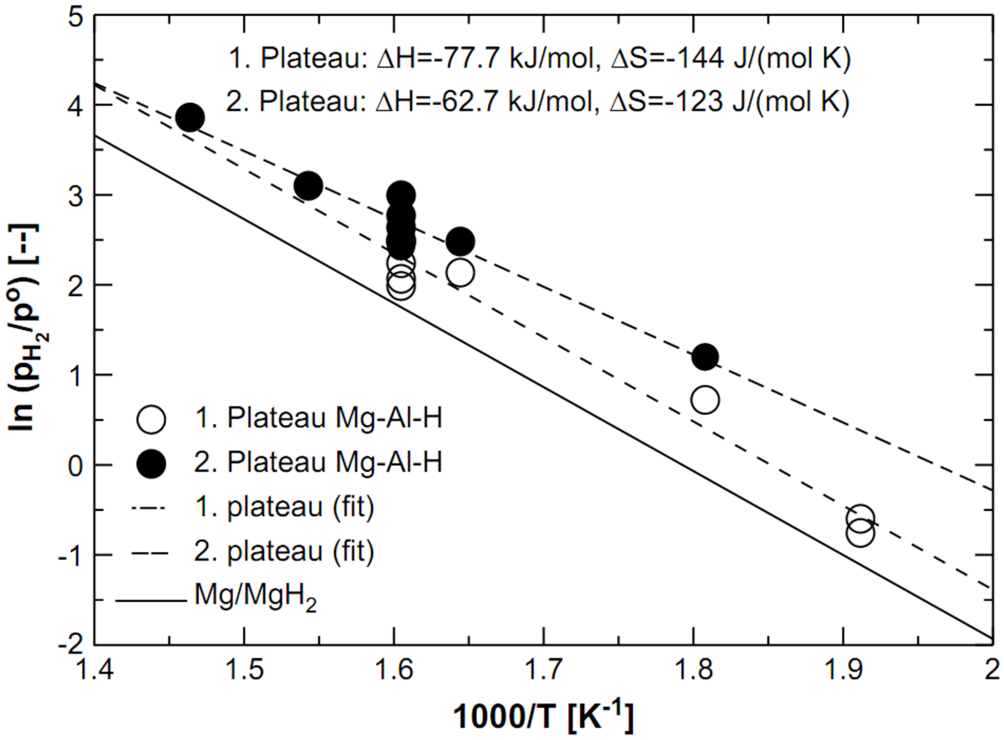

Figure 3.1: A van't Hoff plot of hydrogenation data of MgAl, from Andreasen[28]; the solid line is pure Mg.

3.2 MgAlTi

Unlike MgAl, MgAlTi hydrogen storage materials remain relatively unstudied; there are, however, two main papers that have covered this particular set of elements with relation to hydrogen storage, one by P. Vermeulen et al.[37] and one by R. Gremaud et al.;[85] these papers and their relevance to this study will be examined in turn.

3.2.1 P.H.L. Notten et al.

Vermeulen et al. examined ternary MgTiX alloys, where X = Al and Si, created via sputtering, with the aim of destabilizing the hydride.[37] They found, in a range of alloys $Mg_{1-x-y}Ti_xAl_y$ with $x < 0.6$ and $y < 0.6$, that the plateau pressure was increased, and the gravimetric capacity was maintained near 6 weight percent.

3.2.2 R. Gremaud et al.

Gremaud et al. created what they termed Ti-doped Mg-Al gradient thin films, where a gradient of Mg_xAl_{1-x} was formed from $x = 0$ to $x = 1$, which were hydrogenated and subsequently characterized optically, and via conductivity of the film.[85] It was found that $Mg(AlH_4)_2$ could form in specific ranges of x, but that MgH_2 is favoured for ranges of x above 0.61.[85]

3.3 Papers To Which This Study Contributed

During the course of this study, neutron data and samples from the MgAl section were contributed to three papers by Fritzsche et al.[80, 87, 88], and

sieverts cycling data from the MgAlTi section was contributed to Kalisvaart et al.[89]

4

Experimental

4.1 Sample Preparation

4.1.1 Sputtering

Samples were created using magnetron co-sputtering to deposit thin films onto {100} oriented Si wafers 4" in diameter. Two different sputtering machines were used during the course of this research, the first being and AJA International Orion 5 with 4 sputter-guns (3 DC and 1 RF), which was later upgraded to 5 sputter guns (4 DC and 1 RF), and an AJA International Orion 8 with 6 sputter guns (4 DC and 2 RF). Sputter targets used were of 99.98% purity or

higher. Si wafers were cleaned in a Piranha solution, consisting of three parts 95% H_2SO_4 and one part 50% H_2O_2 for 30 mins.

The sputter machines used allowed for the programming of sputter powers and times of the different guns independently in layers; a gun could be lit and warmed up while other guns were sputtering, so that immediately upon the completion of the layer being sputtered the following layer could begin. This technique prevented oxidation of the surface of the first layer before the second layer began.

Initial samples for this study were simple films designed to determine basic properties of the sputtered MgAl material; these consisted of Mg co-sputtered with Al at various composition ranges from pure Mg to 50Mg50Al, atomic percentage, by holding the Mg sputter rate constant and sputtering with Al at different rates; this was done with both Mg and Al targets in DC guns, and an Mg rate of approximately 4.0Å/s. These were sputtered onto a clean Si wafer, under 4 mTorr pure Ar, flowing at 12 standard cubic centimetres per minute (SCCM). Thicknesses of these films were 1.5μm. Samples of pure Mg in this style - for testing the catalytist layer - added various thicknesses of a pure Pd top layer, sputtered from a DC gun, between 0nm and 50nm in thickness.

Samples for initial MgAl hydrogen testing settled on a 15nm Pd capping layer [64], at compositions ranging from pure Mg to 50Mg50Al (atomic percentage), with the same thickness of 1.5μm; sputter conditions were maintained. These samples, however, required being free of their substrate; a common method from microfabrication was adopted, sputtering onto photoresist[57], except instead of exposing and removing only certain areas of the sputtered film, the entire layer of photoresist was dissolved, resulting in a free-standing film weighing in the 20-30μg range. Samples were made for X-Ray Diffraction (XRD) directly on Si that were exactly half the thickness, with capping layers on top but not on bottom, to simulate the sorption profile that the free-

standing films would see, as those could be absorbed from both sides, while the on-Si films would be absorbed from only one side.

Neutron reflectometry experiments required smaller geometries (Section 5.1.4), so reduced thicknesses of 50nm of various Mg-Al compositions sputtered directly onto Si, with a 10nm Pd capping layer were made; these were considered to be analogous to the surface of larger samples. Later samples for neutron reflectometry added a Ta diffusion barrier between the MgAl and the Pd; Ta diffusion barriers were consequently added between Pd and Mg-Al on samples intended for hydrogen-testing, with the thicknesses cut in half, for 7.5nm each of Ta and Pd.

A final set of films, those of the Mg-Al-Ti system, was sputtered similarly to the final revision of Mg-Al: films were sputtered onto photoresist covered wafers; 7.5nm Pd, 7.5nm Ta, 1.5μm co-sputtered Mg-Al-Ti of a range of compositions, 7.5nm Ta and finally 7.5nm Pd.

4.1.2 Hydrogen Sorption

Hydrogenation for Differential Scanning Calorimetry and Thermo-Gravimetric Analysis (DSC-TGA) was done in a custom-built hydrogenation system. A stainless-steel tube approximately 2.5cm in diameter and 70cm long was run through a tube furnace, with inlet on one end and outlet on the other; on the inlet were attached Ar and H_2 gases through valves; a thermocouple approximately 20cm long was placed in through the outlet, towards the hot-zone. Released samples were placed in a steel boat covered by a steel lid with a vent hole; this was then slid into the tube from the inlet side until it touched the thermocouple, to ensure the temperature of the steel boat was known to an approximate value.

The tube was filled with Ar at ~6.5 bar absolute and vented to 1bar several

times; it was then filled with H_2 gas at >20bar, vented to ~1bar, and finally filled with ~70bar (1000psi gauge) H_2. It was then heated until the steel boat was 125°C, for ~24 hours, and then allowed to cool slowly to ~30-40°C before being removed (to minimize water condensation onto the thin films).

4.2 Material Characterization

A number of instruments were used for material characterization during the course of this thesis work, grouped generally into two categories: those for determining the sorption behaviour of the materials (including kinetics and thermodynamics) and those used to observe the microstructure. In the first category was a DSC/TGA, a high-pressure DSC and two Sieverts-type instruments. Microstructure characterization was done primarily through X-ray diffraction, and some initial SEM micrographs. Neutron reflectometry provided direct insight into the behaviour of hydrogen within the structure of the thin film.

4.2.1 Differential Scanning Calorimetry and Thermo-gravimetric Analysis

Initial hydrogen-loading experiments were performed using an SDT Q600 from TA Instruments, which allowed for simultaneous differential-scanning-calorimetry (DSC) and thermo-gravimetric analysis (TGA). The apparatus was not rated to use hydrogen, so released thin-film samples between 10mg and 25mg were crushed and put into 90μl sample cups, and absorbed with hydrogen in the hydrogen sorption furnace. Two beams, one with a sample and one empty standard were used; a separate sample cup from the one in the furnace was tared on the beams, due to the 24 hour duration of hydrogenation, allowing

experiments to be run more efficiently.

Samples were removed from the furnace at 30-40°C, exposed to air for 15 minutes time, during which they were transferred to the tared sample cup. The time exposed to air was kept as close to the same time as possible, in order to reduce any experimental error due to water condensation on the thin film. Sample cups were placed onto the beams, moved into the sample chamber, through which argon was flowed at 200 SCCM. The samples were ramped at various rates from 0.1°C/min to 20°C/min, and then typically held at a constant temperature for 10 hours or until desorption was completed. Data points were automatically acquired and temperatures were automatically controlled using TA Instrument's software.

4.2.2 High-Pressure Differential Scanning Calorimetry

Determination of the enthalpy of hydride formation was performed using a DSC Q50 from TA Instruments; the system was capable of using hydrogen or helium at up to 69bar (1000psi), or being pumped to low vacuum. The pressure gauge was determined to be considerably less accurate near atmospheric pressure, so primarily pressures above 2bar were tested. The sample chamber was fed by gas lines with manual valves, so constant volume measurements were taken, rather than constant pressure. An empty sample cup and sample on two temperature sensors provided calorimetry measurements, again logged using TA's software, which also provided automatic heating control. Heating ramps were primarily used, as cooling was provided only by the ambient air surrounding the containment vessel.

Samples of 2-5mg of released, crushed, films were placed in 40μl platinum pans with covers. The requirement to use heating ramps necessitated the use of hydrided samples that subsequently dehydrided at high temperatures, and - for the aforementioned accuracy issues - at above 2bar hydrogen. After

several cycles of vacuuming the chamber followed by helium, samples were first hydrided by pressurizing to ~34bar (500psi) hydrogen and ramping to 125°Cat 20°C/min; after 30min or the levelling of the heat-flow signal to zero, the chamber was allowed to cool to 30°C; the pressure was then dropped to various pressures ranging from 2bar to 20bar, and ramped at 5°C/min to 500°C.

The sharp endothermic hydrogen desorption peak which resulted from these tests was then used as a point on a *van't Hoff* plot; as the peak onset was ambiguous and the peak very thin, the peak temperature and pressure was used; an example is shown in Figure 2.6. These plots were used primarily as a quick verification of enthalpy of hydride formation, confirming the hydride being formed as MgH_2.

4.2.3 Hydrogen Kinetics Measurements and Cycle Life Determination

Kinetic cycling measurements were carried out on two PCTPro2000 Sieverts-type instruments from HyEnergy Scientific Instruments. A kinetic cycle consisted of a hydrogen absorption step, followed by a desorption step. Released and crushed thin film samples of 15-20mg were used in a sample holder consisting of a half-inch VCR (vacuum coupling radiation laboratory fitting) cap; after attachment to the system, the sample volumes were calibrated and flushed using helium, and heated to a temperature for cycling, typically 200°C. Absorption steps involved vacuuming out the small sample holder and gas lines, totalling 11.9ml, and pressurizing this volume with hydrogen, typically 3bar; as gas was absorbed the pressure would drop, ending typically around 1.5bar. The subsequent desorption steps involved evacuating a large volume of ~1025ml, opening it to the sample volume, allowing the remaining gas to expand, resulting in a starting pressure for desorption of ~5mbar; desorption of hydrogen

raised the pressure typically to 15-20mbar; after desorption, the sample was further evacuated for 5 minutes to remove any excess hydrogen. Both absorption and desorption steps were stopped using rate-limiting checks of 0.005 wt%/min over a 4 minute period. These parameters were controlled by the HyEnergy software, as was data logging.

The samples were allowed to cycle for differing numbers of cycles and time lengths depending on performance; final samples using Mg-Al-Ti alloys were allowed to cycle for at least 120 cycles.

4.2.4 X-Ray Diffraction

X-Ray Diffraction (XRD) was used to for phase determination, and was performed on a Bruker AXS diffractometer (Bruker Discover 8) with a Cu Kα source ($\lambda = 1.5406$Å), in the Bragg-Brentano configuration, shown in Figure 2.18. Early samples were on-wafer films representing half of a released film, as-sputtered and after hydrogen absorption, as the released film pieces would not pack into powder sample cups. Later samples cycled many times in the Sieverts apparatus were measured on-wafer before release, and were measured in a powder sample cup after many cycles, as they had degraded into pseudo-powder, in either absorbed or desorbed state. The XRD software package DIFFRACplus EVA (made by Bruker) and its database was used for peak identification.

4.2.5 Neutron Reflectometry

Neutron reflectometry was performed at Chalk River, Ontario, in the National Research Universal (NRU) reactor on the D3 reflectometer (Figure 2.19) as part of a collaboration between NINT (National Institute of Nanotechnology) and the Canadian Neutron Beam Center (CNBC). The D3 reflectometer used

a focusing pyrolytic graphite monochromator with a neutron wavelength of $\lambda = 0.237\text{n}m$, and a pyrolytic graphite filter, which reduced higher order multiples of the wavelength.

As-sputtered samples and samples absorbed with hydrogen were shipped to Chalk River and measured under the beam; the absorbed samples were further desorbed in a cell with 1bar Ar atmosphere and an attached heater to allow desorption at up to 200°C. Data was analyzed using the PARRAT32 software package, to determine scattering length density (SLD) profiles of the films.

4.2.6 Scanning Electron Microscopy

A Scanning Electron Microscope (SEM) was used to examine the morphology of initial films, to give a rough estimate of the crystallinity and roughness of the films. This was done on a Hitachi S-4800, on as-sputtered samples which were directly on silicon.

5

Results

Results of this study are laid out in two sections: MgAl and MgAlTi. The first section, MgAl, developed some of the basic methods used in both MgAl and MgAlTi, as well as other hydrogen storage alloys developed in our research group, including the Pd catalytic layer thickness and subsequent Ta diffusion barrier; it was during this study that additional equipment such as the Sieverts apparatus became available, and consequently the studies performed evolved over the course of the research. Neutron Reflectometry performed on the MgAl films at the Canadian Neutron Beam Center (CNBC), provided direct insight into the interaction between catalytic layers and hydrogen storage layers, and interaction between hydrogen and these layers (see Section 4.2.5); this insight was what instigated the move to a bilayer catalyst. The dependence of each

study upon the previous is self-evident; consequently, studies are arranged approximately chronologically, grouped, however, by type. The second section, MgAlTi, is also grouped by study type; these studies progressed concurrently, largely due to the multi-day run-time of Sieverts kinetics measurements.

5.1 MgAl

The first material investigated was MgAl; as discussed in Section 2.4.1, the high-Mg end of the MgAl phase space was of primary interest; it was primarily divided up by percentages of 10, ranging from Pure Mg to 50Mg50Al, with further divisions on the low end as necessary. The goals in designing this alloy series were to investigate good candidates for storage alloys, and to determine the required Pd catalytic layer, as discussed in Section 2.2.1. Initial characterization of the materials was done using Scanning Electron Microscopy (SEM).

5.1.1 Scanning Electron Microscopy

The initial characterization tool used on MgAl films was scanning-electron-microscopy, or SEM, of non-capped 1.5μm MgAl films sputtered directly onto a Si wafer. The purpose of performing SEM was twofold: one, to investigate the overall roughness of the films; and two, to examine the surface characteristics to gauge the effect of sputtering a thin Pd capping layer onto the surface; a surface with sharp peaks may affect the Pd layer significantly, as material will tend to diffuse to sharp valleys and away from peaks [47]. Two separate SEM runs were performed, the first by Reza Mohammadi and the second by Colin Ophus.

As seen in Figure 5.1, pure Mg is quite rough; adding 5% Al makes the crystals

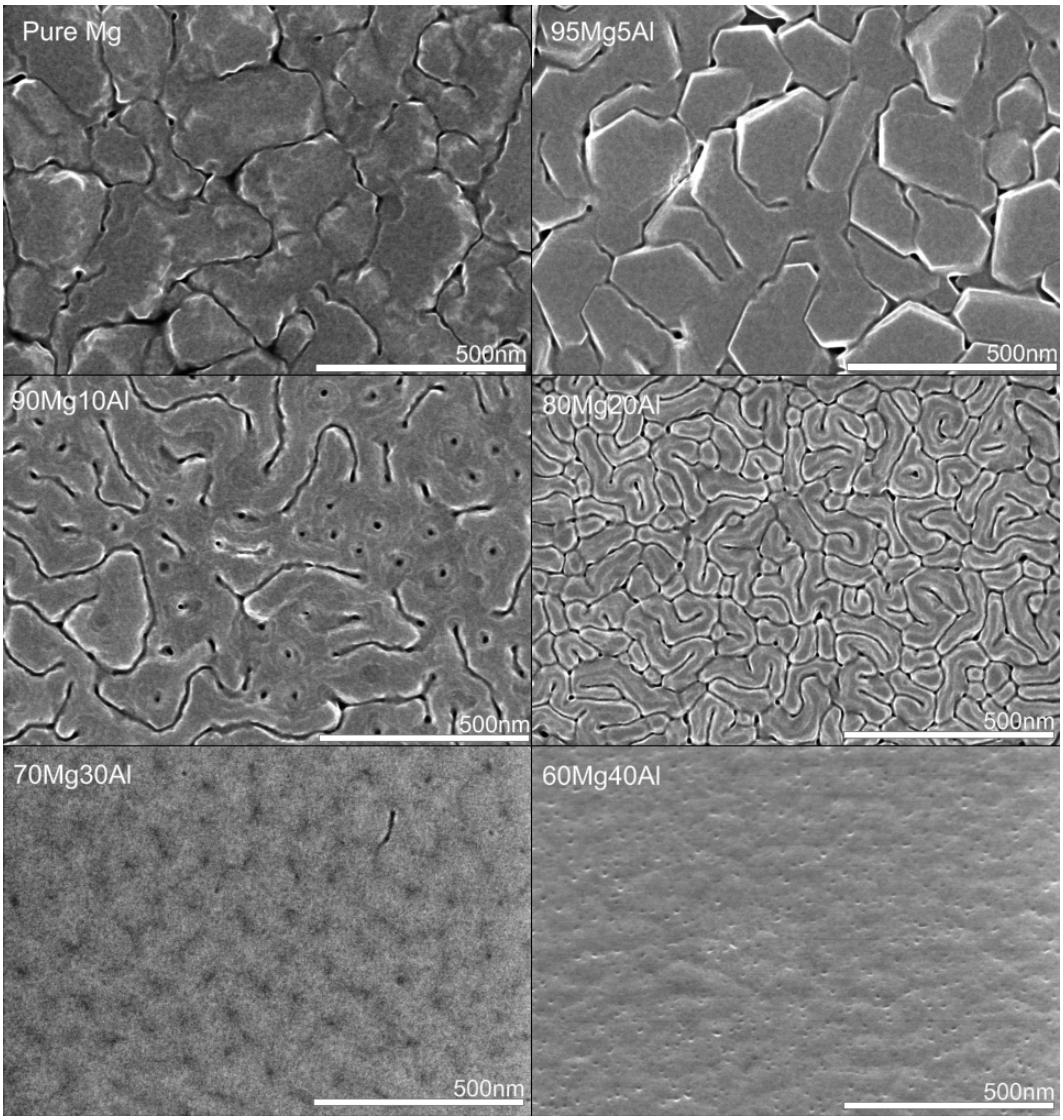

Figure 5.1: SEM micrographs of a range of uncapped MgAl compositions from Pure Mg to 40%Al in plan view at 100k magnification. The films become smoother towards higher Al percentage, as the film becomes amorphous[90]

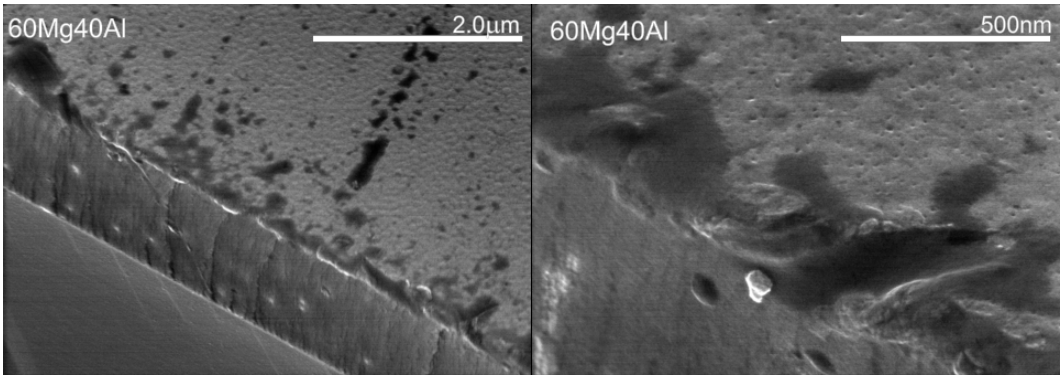

Figure 5.2: SEM micrographs of the side of a cleaved, uncapped 40%Al film.

more distinguishable, and further Al addition reduces the crystal size and decreases the overall roughness. From these images it cannot be determined if the higher Al concentrations are amorphous or nanocrystalline; investigation by XRD can elucidate that particular question. The first five images, pure Mg through 30% Al were part of the first run of SEM, and the 40% Al was part of the second run. Figure 5.2, a view of the edge of the cleaved film, further illustrates the relatively low roughness of the 40% film, and provided the first view of the films internal structure. These images pointed to the 20% to 40% range as a promising range of study, as they appeared to have both the smallest grain size (and hence the most grain boundaries, as discussed in Section 2.3.2) and have the most promise of a supporting a continuous Pd cap layer due to low roughness.

5.1.2 Differential Scanning Calorimetry and Thermogravimetric Analysis

The DSC-TGA or differential scanning calorimeter with thermogravimetric analysis was the initial tool used in conjunction with a hydrogen sorption furnace (see Sections 4.1.2 and 4.2.1) for determination of hydrogen storage in terms of weight percentage and kinetics.

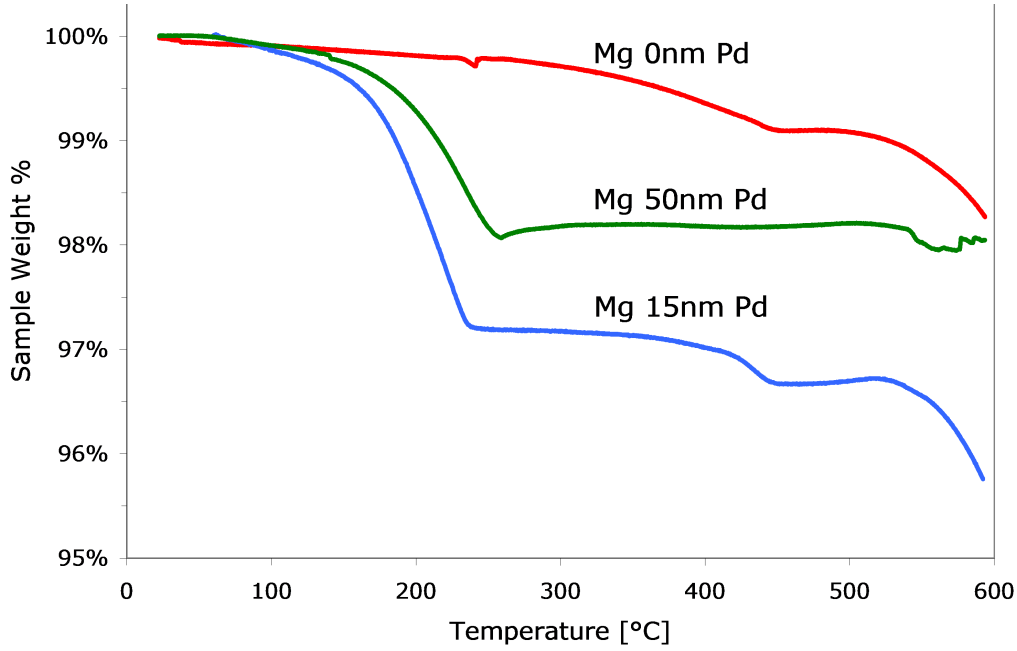

Figure 5.3: Thermogravimetric curves (TGA) for various thicknesses of Pd on top of pure Mg.

DSC-TGA determination of Pd thickness

The first study performed was a series of Pd caps of varying thickness, from no cap to 50nm thick on pure Mg, to determine the optimal thickness of Pd for use as a catalyst; while it had been observed earlier (Section 5.1.1) that the higher Al concentrations might be best for a continuous capping layer, in the interest of isolating catalytic variables, pure Mg was chosen as a base layer. Figure 5.3 shows several DSC-TGA runs with varying thicknesses of Pd; it is reasonably clear that the 15nm Pd capped film desorbed faster than either the 50nm capping layer or the film without a cap. It is suspected that the thin film adsorbs water from the air onto its surface and that its high surface area allows for this to be a significant fraction of the weight; this was mitigated by transferring samples at 30-40°C, as described in Section 4.1.2.

The 15nm Pd cap achieved the intended result, so this thickness was chosen to

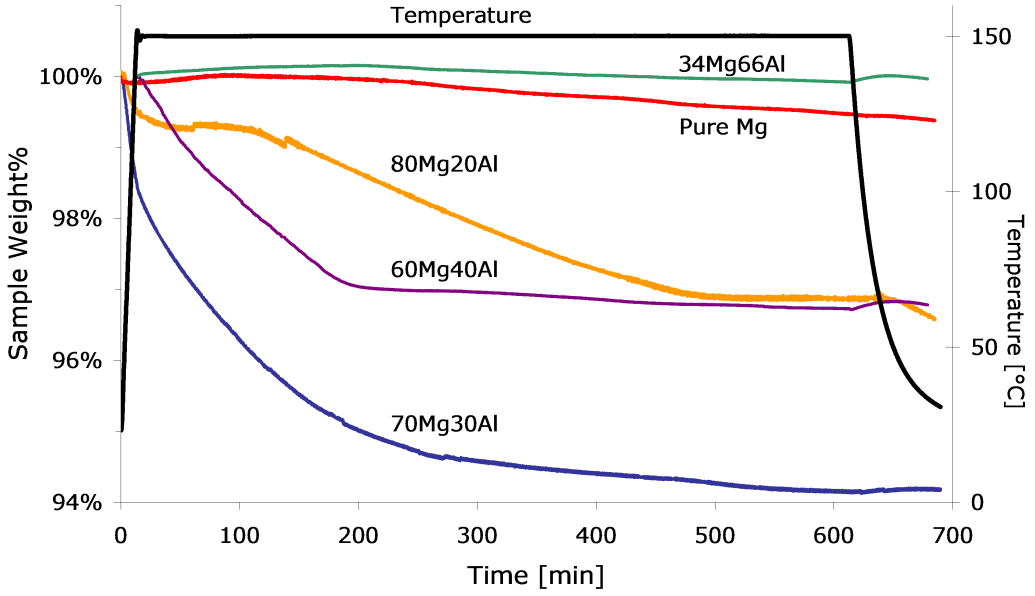

Figure 5.4: DSC-TGA weight percentages, compared to initial sample weight, during desorption of Pure Mg, 80Mg20Al, 70Mg30Al, 60Mg40Al and 66Mg34Al. The temperature profile is shown in black against the right axis.

be used as a Pd capping thickness for subsequent DSC-TGA experiments, as it also erred towards a thicker film in the interest of preventing film oxidation.

DSC-TGA Isotherms

The first examination of the MgAl system was using the DSC-TGA, specifically examining the desorption behaviour of a range of compositions under isothermal conditions at elevated temperatures; 150°C was chosen as an aggressive starting temperature compared to typical literature values of 250-350°C for Mg based items; samples were ramped at 10°C/min until they reached 150°C, where they were held at temperature for 600min or until desorption was observed to have stopped. Samples of 1.5μm capped on both sides with 15nm Pd were used in this series, as described in Section 4.1.1, and were sorbed with hydrogen at 125°C for 24 hours as described in Section 4.1.2.

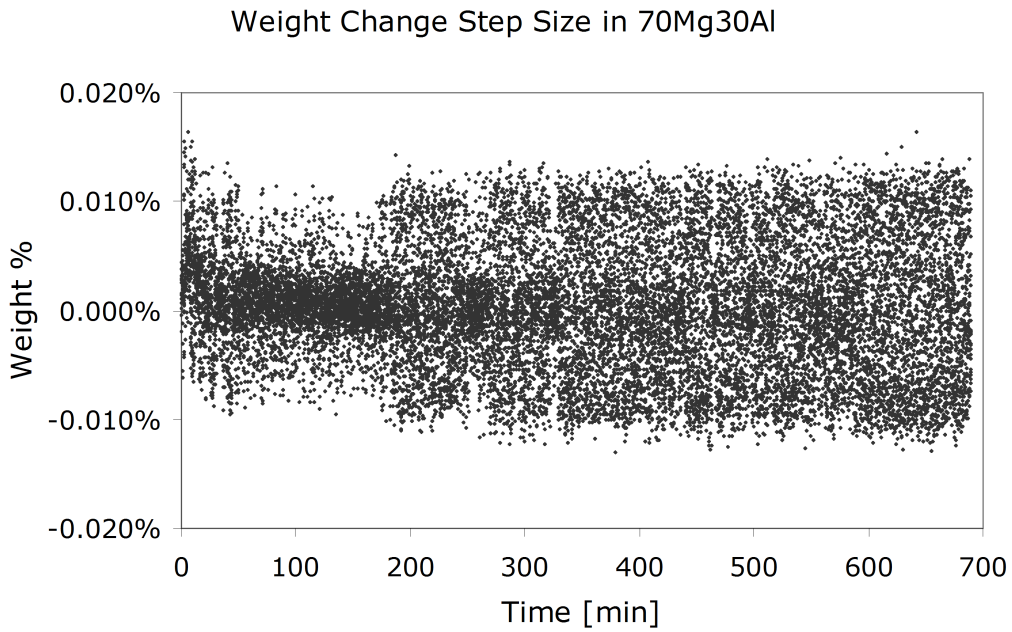

Figure 5.5: Change in weight percentage per time step for a 70Mg30Al film during DSC-TGA desorption, according to the temperature profile in Figure 5.4. Points significantly outside the displayed range were filtered.

During this series of experiments, certain issues with the DSC-TGA sample preparation were identified: unless well packed in the sample cups, the thin film had a tendency to be picked up by the flowing Ar gas (see Section 4.1.2), which caused the film to be partially blown out of the sample cups. These events were clearly visible in the data as vertical drops; changes in the data were observed to be often 10-100 times as great as the maximum typical changes, an example of which, the 70Mg30Al sample in this series, is shown in Figure 5.5; consequently these points were filtered by removing points more than 5 standard deviations away from the typical step size, and the data normalized to the original weight percentage.

Isothermals at 150°C for various compositions of MgAl are shown in Figure 5.4; the sample weight percentages relative to their initial weight are graphed, and the temperature profile is shown in black against the right axis. As the desorption proceeded slowly, the DSC portions of the DSC-TGA results occurred over the whole desorption time, resulting in slow curves which were only slightly above the background. The pure Mg sample showed little desorption at this temperature, as expected given literature values for Mg. Addition of Al to the Mg showed a dramatic increase in desorption ability with 80Mg20Al; desorption started slowly, and slowly increased until an approximately linear rate was achieved, before trailing off at the completion of desorption by 500mins; this could indicate a nucleation and growth mechanism. In the slightly higher Al compositions of 70Mg30Al and 60Mg40Al the initial slow desorption is not observed, and in fact the 70Mg30Al shows rapid desorption initially; however, this could be partially due to absorbed water vapour as previously mentioned; 70Mg30Al is nonetheless faster than the 80Mg20Al with approximately 300mins to main desorption; the desorption curve shows a gradual slowing of desorption in this case, until full desorption near 600 mins. The 60Mg40Al sample displays slightly slower desorption characteristics than early in the 70Mg30Al desorption, but shows a relatively linear desorption, similar to the 80Mg20Al. The 34Mg66Al, an examination of the 1:2 Mg:Al

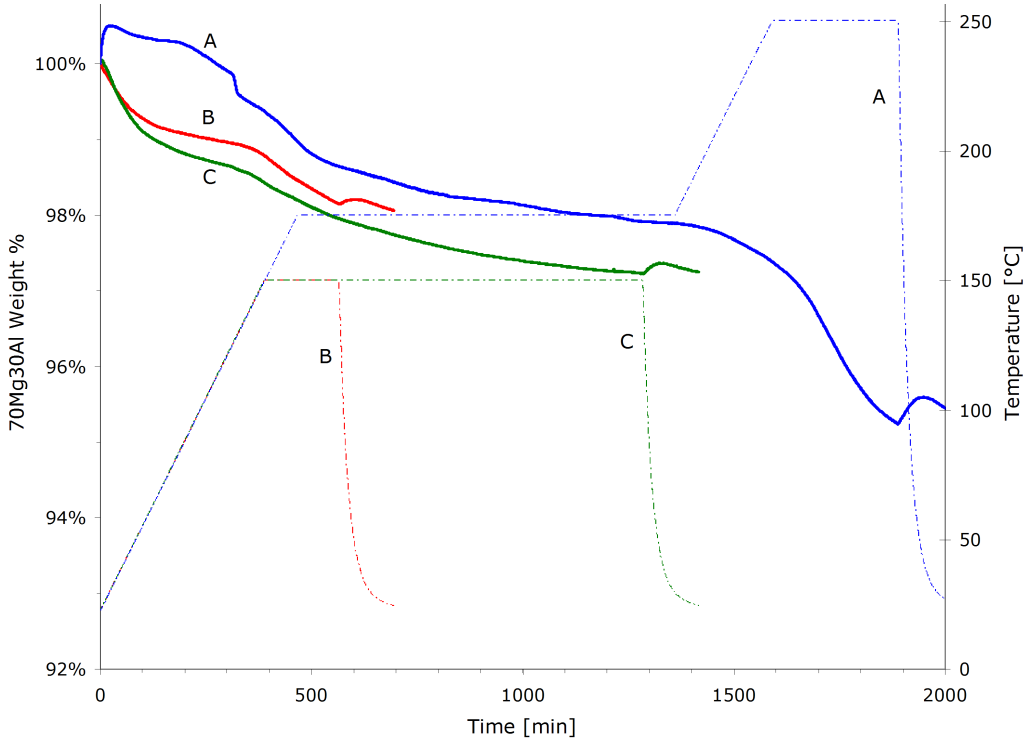

Figure 5.6: DSC-TGA weight percentages (as compared to initial sample weight) of three 70Mg30Al samples with different temperature profiles; temperatures are shown as dashed lines against the right axis, labelled according to their sample; the apparent increase of the sample weight with decreasing temperature is due to thermal drift and is inversely proprtional to the weight of the sample.

ratio, demonstrated no ability to desorb at these temperatures. The results of this study encouraged focus on the 80 percent Mg to 60 percent Mg range, and these were investigated further in the following sections; desorption at the relatively low temperature of 150°C was demonstrated for these compositions versus pure Mg and higher Al content films, indicating that the design principles were sound.

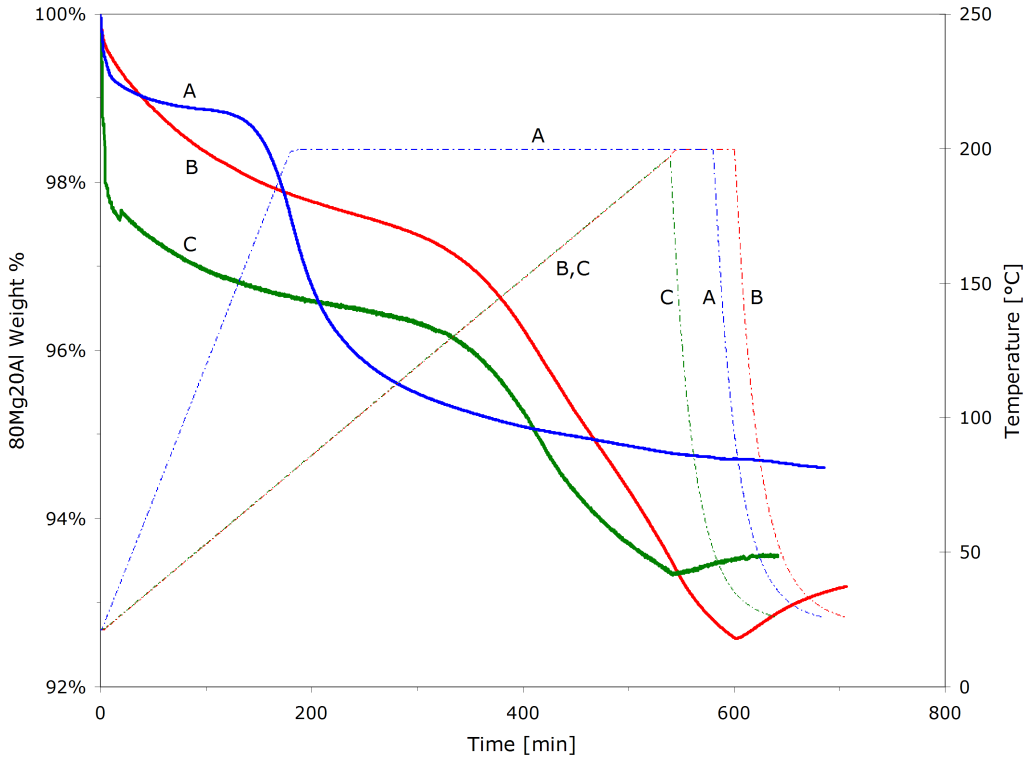

Figure 5.7: DSC-TGA weight percentages (as compared to initial sample weight) of three 80Mg20Al samples; their corresponding temperature profiles are labelled and shown as dashed lines against the right axis; the apparent increase of the sample weight with decreasing temperature is due to thermal drift and is inversely proprtional to the weight of the sample.

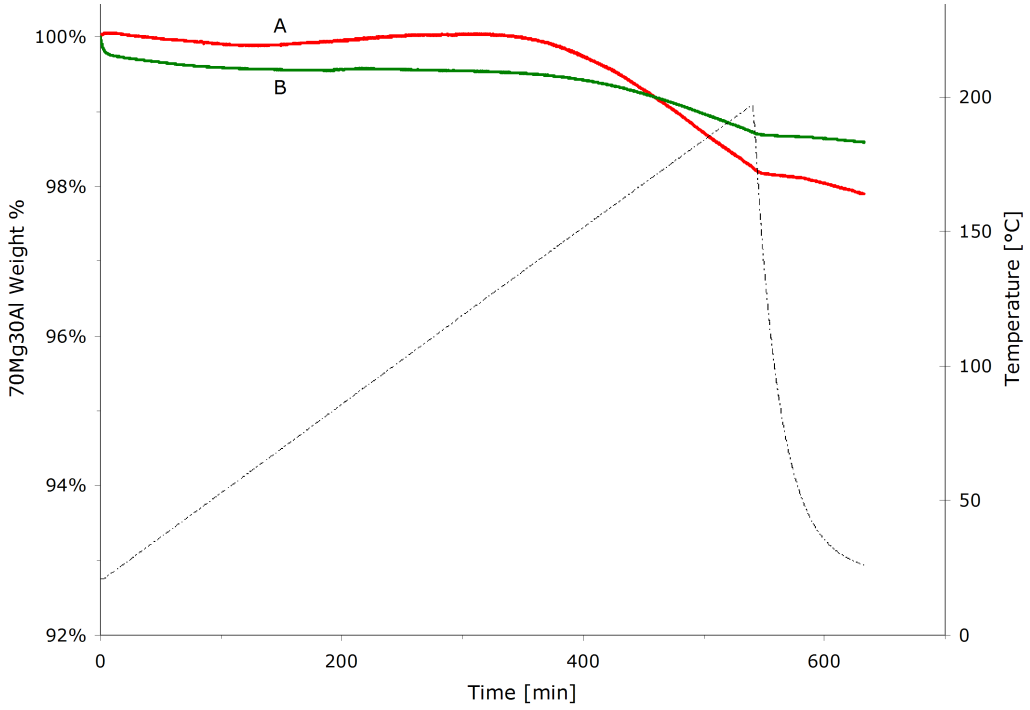

Figure 5.8: DSC-TGA weight percentages of two 70Mg30Al samples, with a common temperature profile in black against the right axis; the apparent increase of the sample weight with decreasing temperature is due to thermal drift and is inversely proprtional to the weight of the sample.

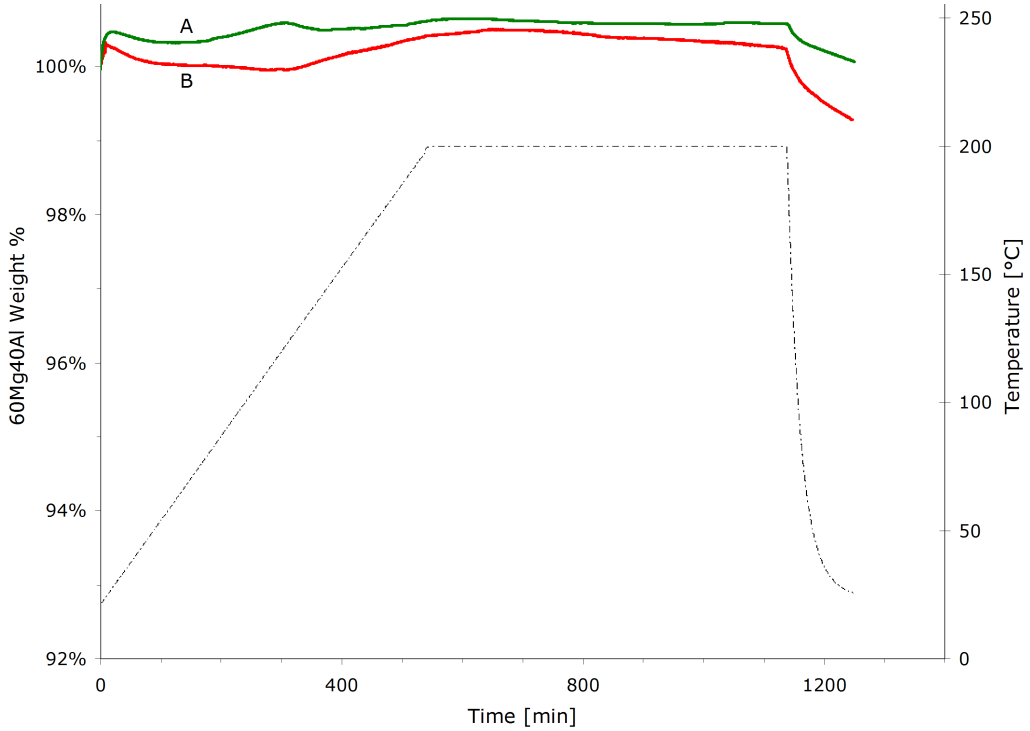

Figure 5.9: DSC-TGA weight percentages of two 60Mg40Al samples, with a common temperature profile in black against the right axis; the apparent increase of the sample weight with decreasing temperature is due to thermal drift and is inversely proprtional to the weight of the sample.

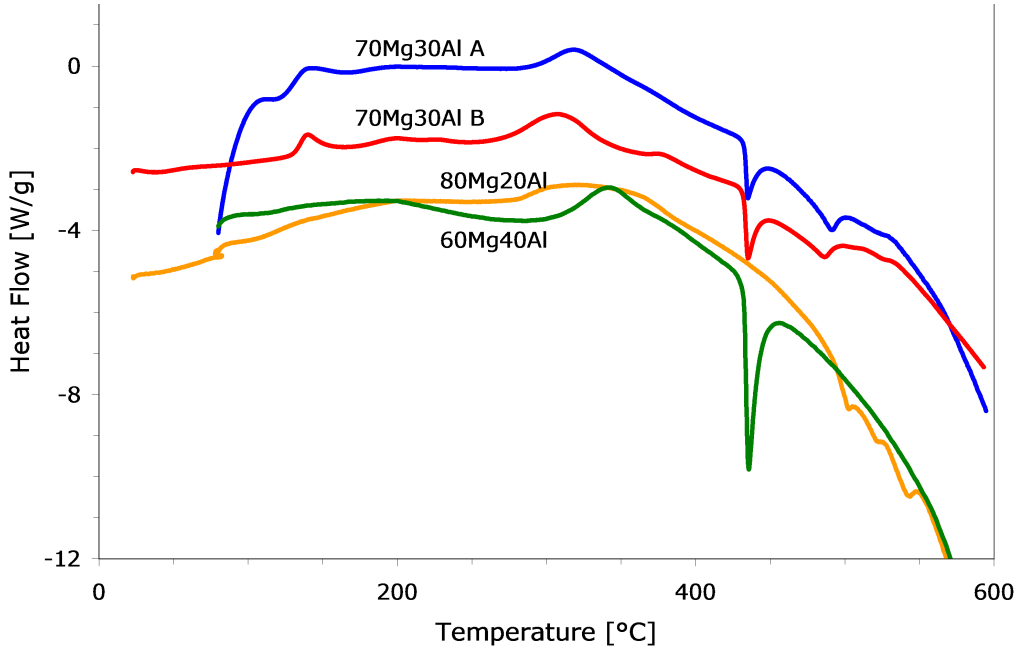

Figure 5.10: DSC-TGA heat flow of an 80Mg20Al, a 60Mg40Al and two 70Mg30Al samples; this graph is exothermic up.

DSC-TGA Investigation of MgAl Desorption Properties

Having demonstrated that the 80Mg20Al, 70Mg30Al and 60Mg40Al compositions were of most interest in the previous series, these compositions were investigated for their general desorption characteristics. Specific goals were to determine if the hydrides were single phase or multiple phases, by looking for separate events in desorption rates at different temperatures along temperature ramps, and observing the DSC portion of the data; to determine if the hydrides were kinetically limited below certain temperatures; and to determine more accurately the maximum weight percentage stored by each composition.

For this series, several methods were utilized in sample preparation to eliminate errors previously observed in data; first, using lids on the sample cups was tried, but this was observed to create slight initial increases in weight percentage, as shown in Sample A of Figure 5.6; this was later found to be

a result of trapped atmosphere in the cups causing the cups to be slightly buoyant in the Ar atmosphere of the DSC-TGA chamber; consequently this approach was abandoned. Secondly, as previously mentioned, the samples were removed at 30-40°C from the hydriding furnace to mitigate water adsorption onto the surface of the films. However, it was observed that variations in duration between the sample exiting the furnace and entering the chamber caused different initial desorption curves; this time was thus set to 15 minutes, as described in Section 4.2.1, as some time was required to transfer the sample into a tared DSC-TGA cup; an apparent consequence of the elevated temperature and conservative time estimate for sample preparation was that overall weight percentages were observed to drop during this series as compared to the previous series. These results further prompted the move to a Sieverts apparatus for subsequent experiments.

The first samples investigated were 70Mg30Al, as they appeared the most promising range in the previous series; these 70Mg30Al samples have a maximum theoretical weight percentage of ~5wt% (Table 2.5). These samples were investigated under various heating conditions, as shown in Figure 5.6; all samples were ramped at 0.3°C per minute to their isothermal temperatures. As the DSC-TGA allowed us to change temperature profiles and settings as data was collected, Sample A was exposed to 250°C after it showed behaviour that was inconsistent with the previous series; this showed that significant quantities of hydrogen were unable to desorb at 175°C, a temperature slightly higher than the previous series; the initial bump was found to be due to buoyancy of trapped atmosphere in the sample cups, which in turn was due to using cup lids for this particular sample. Samples B and C were observed under similar conditions, the first having a similar isothermal length to the previous series, and the second having an extended isothermal period. Weight percentages were observed to be significantly lower than previously observed; this is likely due to the aforementioned elevated temperatures. Despite this, it was observed that desorption accelerated just before reaching the setpoint

of 150°C; this indicated that at least 150°C appeared necessary for timely desorption, and Sample A indicated that for maximum hydrogen capacities slightly higher temperatures may be necessary. Initial desorption also indicated either the presence of a second hydride phase, or of hydrides located in a more favourable location for desorption.

The second set of samples were 80Mg20Al, with a theoretical maximum weight percentage of ~6wt% (Table 2.5), were investigated under slightly different temperature profiles, shown in Figure 5.7; the extended isotherm was observed to be of limited use in the previous samples, and heating rates were varied; Sample A was ramped at 0.1°C/min and held under isothermal conditions, while B and C were ramped at 0.33°C/min; the isothermal was abandoned for Sample C. Acceleration of desorption was observed at approximately 150°C in Sample A, while in Samples B and C it was observed to be closer to 125°C. The start of Sample C shows the characteristic that was attributed to adsorbed-water desorption, leading to uncharacteristically high weight percentages. Sample B also shows weight percentages which should be theoretically impossible, strengthening the conclusion that the samples had been contaminated by water in some fashion.

After the testing parameters had been adjusted in the previous samples, 70Mg30Al was re-examined; as shown in Figure 5.8 both Samples A and B were heated at 0.33°C/min to 200°C without an isothermal hold; minimal desorption was observed, though what was observed was consistent with the previous samples in the appearance of acceleration of desorption slightly before 150°C.

The 60Mg40Al samples were heated under similar conditions to the previous samples, ramped at 0.33°C/min to 200°C, with an additional isothermal hold; the sample showed no significant desorption, as can be seen in Figure 5.9. This is in contrast with the first series which showed significant desorption, and underscores the difficulty in obtaining repeatable DSC-TGA results on thin films.

In an effort to further utilize the DSC-TGA and avoid looking directly at weight percentages, several runs on this series of samples (80Mg20Al, 70Mg30Al, 60Mg40Al) were done where the samples were heated up to 600°C, to investigate possible phase changes. The results' most obvious feature, shown in Figure 5.10, is the melting point of mixed MgAl (see the phase diagram, Figure 2.7) at 437°C; before this, however, the 70Mg30Al samples show slight exothermic peaks where desorption was previously observed to accelerate, around 125°C. Broad exothermic peaks were observed in all samples above 300°C, possibly indicating the materials are recrystalizing from their sputtered metastable state.

The difficulties experienced with the DSC-TGA results indicated a unified absorption and desorption solution was required. As the Sieverts apparatus fulfilled this function, further capacity and determination of cycling ability was delayed until the Sieverts apparatus became available.

5.1.3 X-Ray Diffraction

The X-Ray Diffractometer (XRD) was used in determining the phases present in the as-deposited and hydrided films; these films were analogous to half the previously investigated films sputtered directly onto silicon, as described in Section 4.1.1. The as-deposited films were expected to be highly textured for a specific crystal orientation, as a typical sputtered film is in the as-deposited state (Section 2.5.1); the hydrided films were expected to retain some of this texture as they were tested after their first hydrogenation; the texture is expected to disappear if the film is exposed to elevated temperatures for long enough, as it undergoes annealing. The curves in the various figures in this section have all been scaled independently in order to display their features; as a consequence of this and of their textured nature, their relative peak heights are not indicative of any compositional information.

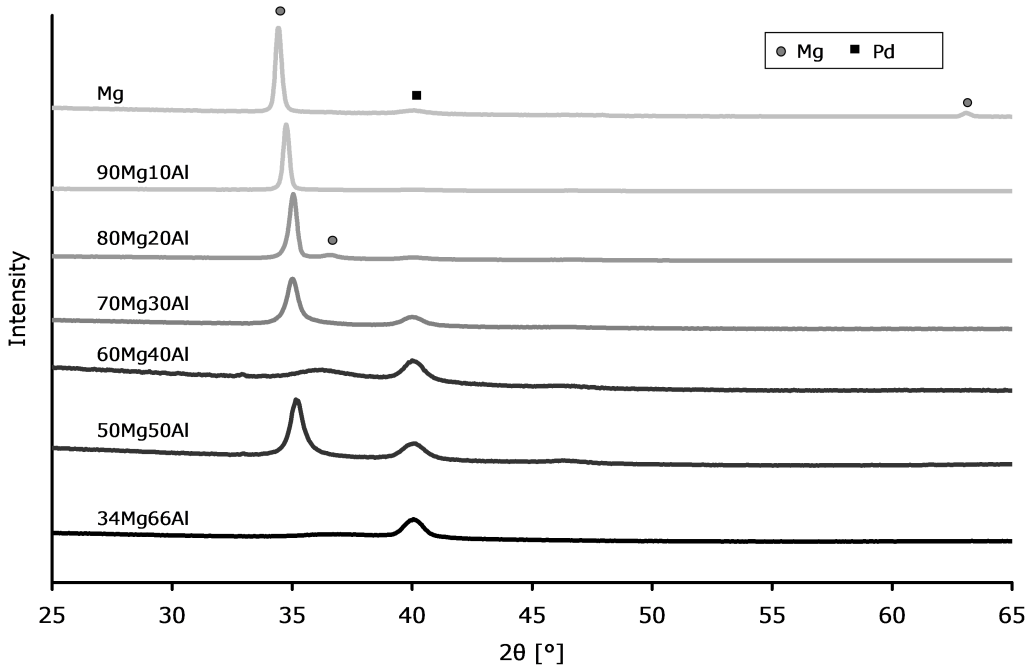

Figure 5.11: X-Ray Diffraction curves of a range of as-deposited Mg-Al compositions; the curves in this figure have been scaled independently to demonstrate the shift of the Mg {0002} peak.

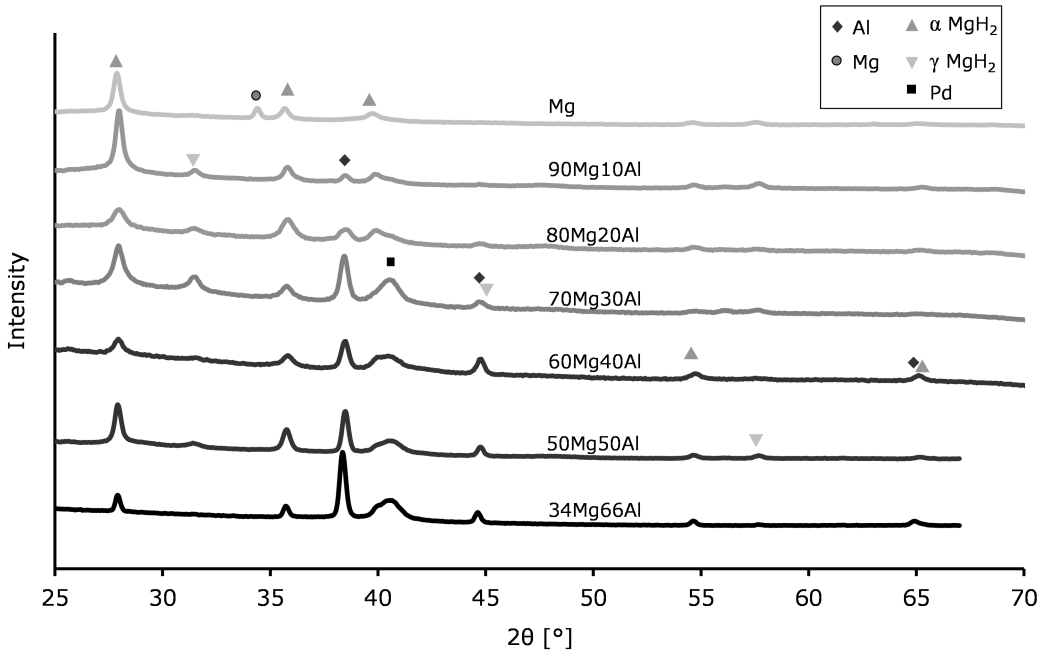

Figure 5.12: X-Ray Diffraction curves of a range of sorbed Mg-Al compositions.

The as-deposited films, shown in Figure 5.11, look relatively similar showing primarily Mg (JCPDS Card no. 89-4244) and a Pd (JCPDS Card no. 46-1043) peak. The pure Mg curve shows a strong Mg peak and a Pd peak; the Mg peak is observed in the subsequent films to shift to slightly higher angles as Al (JCPDS Card no. 4-787) composition increases: as XRD peaks are based on the lattice spacing of the material this is expected as Al, which has a smaller lattice spacing than Mg, is substituted for Mg, thus making the overall lattice smaller, leading to a higher angle for the peak (Section 2.5.3). The palladium peak, at approximately 40°, is the other main feature of the as-deposited scan. This peak does not move, as expected, as it is due primarily to the top 15nm Pd layer. As it is a pure top layer with only slightly different substrates, the peak is approximately the same in each layer, and can be used as a very rough gauge of the relative intensity of the Mg peaks. While the peaks should be similar in height and breadth for a similar top layer, the underlying films can greatly affect the texture, and often have roughness greater than the thickness

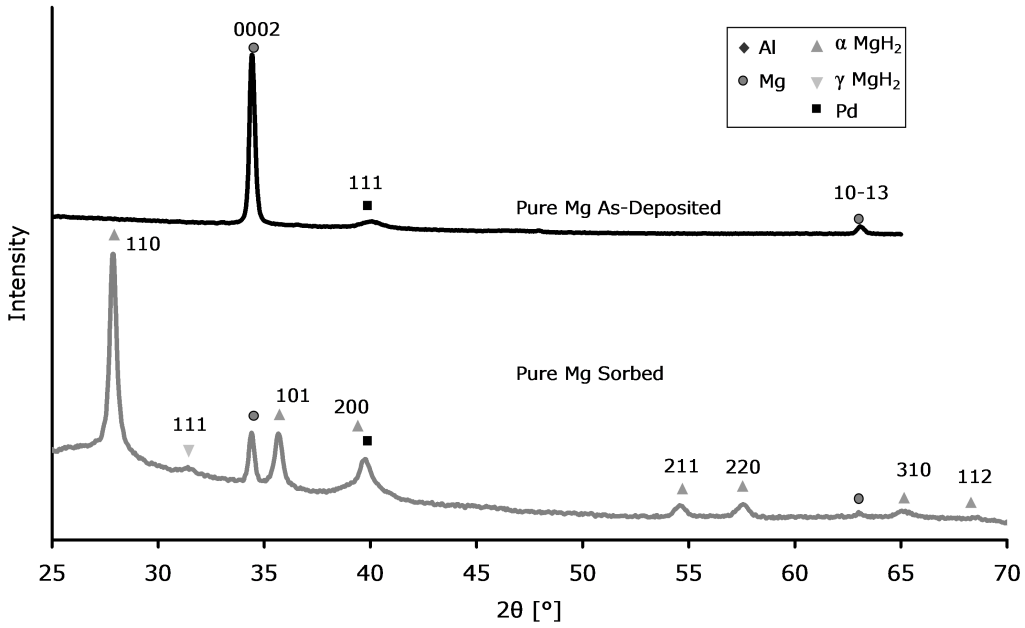

Figure 5.13: X-Ray Diffraction curves of as-deposited and sorbed Pure Mg, scaled independently for comparison of peak locations.

of the 15nm Pd top layer. In the 90Mg10Al and 80Mg20Al, the Pd peak, though not visible with the scaling required, is of the same intensity as the Pd peaks in other compositions.

The sorbed films are somewhat more complicated, as the film was hydrided and, during the process, exposed to high temperatures, allowing it to relax. Consequently there are five easily identifiable phases in this series: textured-Mg that was not sorbed, visible only in the Pure Mg; Al, two peaks of which become increasingly dominant with addition of Al and a third peak at higher angles more visible in the higher composition; α-MgH_2(JCPDS Card no. 12-697), visible in peaks at 27.9°, 35.7°, 39.9°, 54.6° and 57.8°, the phase expected from hydriding Mg; a γ-MgH_2 phase (JCPDS Card no. 35-1184), which appears as three peaks at 31.5°, 45.0°, and 31.5° strongly in the 90Mg10Al, 80Mg20Al and 70Mg30Al, and somewhat more faintly in the 60Mg40Al and 50Mg50Al; and finally the Pd peak from the top layer at 40°, which remains

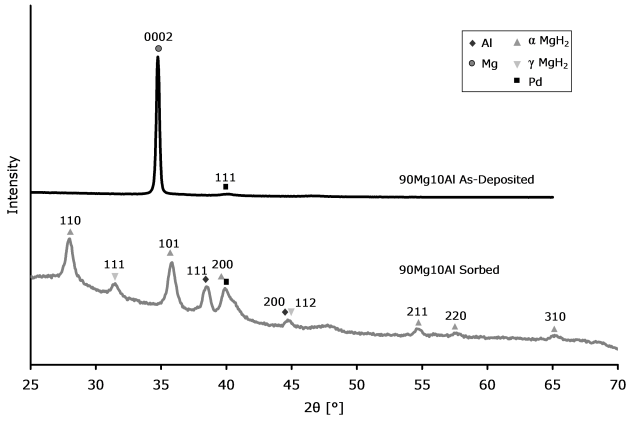

Figure 5.14: X-Ray Diffraction curves of as-deposited and sorbed 90Mg10Al, scaled independently for comparison of peak locations.

constant through the compositional range.

When comparing the as-deposited to sorbed film in the pure Mg, it can be seen that the film did not fully convert to MgH_2, as the two Mg peaks are still apparent (Figure 5.13), however the α-MgH_2 peaks are dominant. A γ-MgH_2 peak is present, but very small.

The 90Mg10Al patterns (Figure 5.14) indicate the sorbed film was indeed fully sorbed, as there is no residual Mg peak. The {111} γ-MgH_2 peak is fairly strong in this composition, although the α-MgH_2 peaks are stronger. This suggests that the main hydride component is α-MgH_2, but that γ-MgH_2 is also significant. A pair of weak aluminium peaks are present, indicating some of the Al precipitated.

The as-deposited 80Mg20Al film, (Figure 5.15), has a broader {0002} Mg peak, and an additional {10-11} Mg peak, suggesting a less textured matrix than the 90Mg10Al. As in the 90Mg10Al, the sorbed film shows both γ-MgH_2 and α-MgH_2; the Al peak is also stronger, as would be expected of a film with higher Al content.

The 70Mg30Al film has several notable differences from the previous films

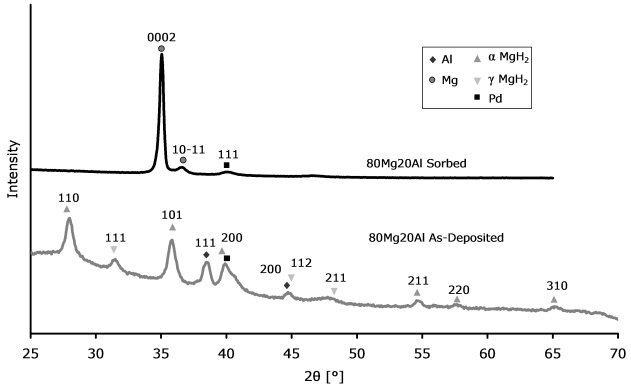

Figure 5.15: X-Ray Diffraction curves of as-deposited and sorbed 80Mg20Al, scaled independently for comparison of peak locations.

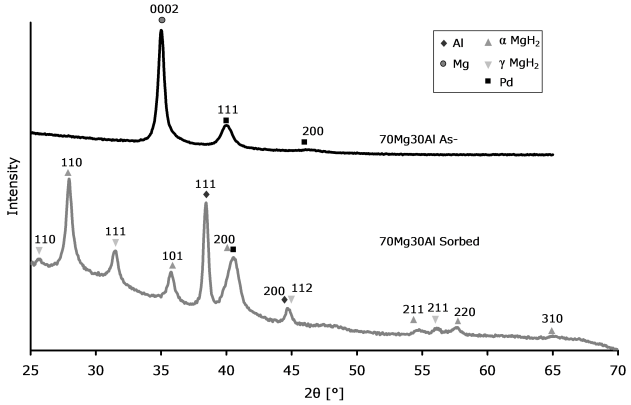

Figure 5.16: X-Ray Diffraction curves of as-deposited and sorbed 70Mg30Al, scaled independently for comparison of peak locations.

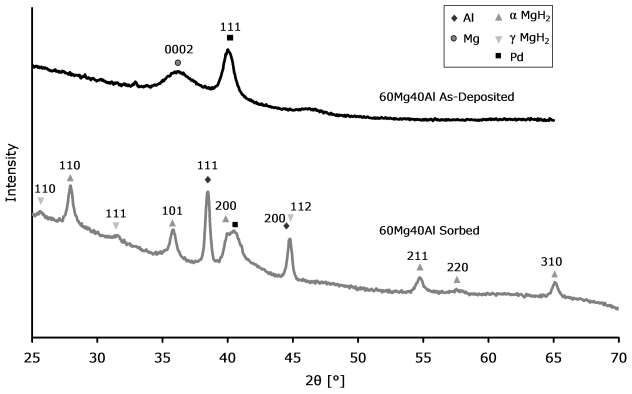

Figure 5.17: X-Ray Diffraction curves of as-deposited and sorbed 60Mg40Al, scaled independently for comparison of peak locations.

(Figure 5.16): It appears to be less textured than the previous films, having a {0002} Mg peak that is only several times the height of the Pd {111} peak in its as-deposited state; and the sorbed film has sharper, stronger Al peaks. α-MgH_2 and γ-MgH_2 remain in similar ratios as the 80Mg20Al.

The 60Mg40Al has a broad and short {0002} peak in the as-deposited compared to the Pd peak (Figure 5.17); this suggests that the film is less textured. When comparing the as-deposited to the 70Mg30Al, the γ-MgH_2 signal has decreased, and the Al signal has increased, especially the Al {002}, with respect to the Pd peak.

The 50Mg50Al as-deposited is more similar to the 70Mg30Al than to the 60Mg40Al, the Mg {0002} peak once again being strong (Figure 5.18). In the sorbed state it shows sharpened peaks for the α-MgH_2 and Al, likely indicating the phases are agglomerating into larger particles. The γ-MgH_2 is still present, but it has decreased until only the {111} is still prominent.

The final composition in this series , 34Mg66Al - approximately 1:2 Mg:Al - is obviously quite different than the previous compositions when even casually looking at the pattern (Figure 5.18): the Mg {0002} has nearly disappeared, being a flat, broadened bump next to the {111} Pd peak, indicating that the

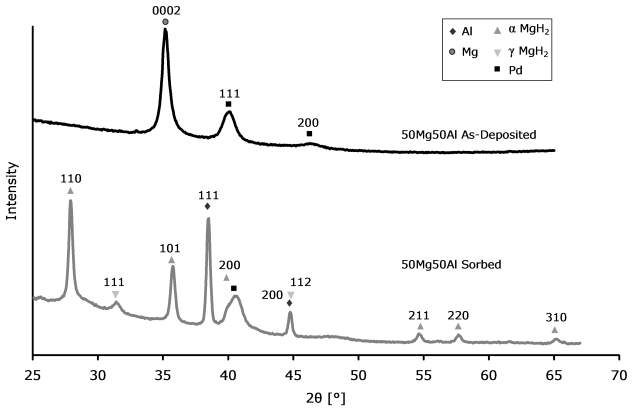

Figure 5.18: X-Ray Diffraction curves of as-deposited and sorbed 50Mg50Al, scaled independently for comparison of peak locations.

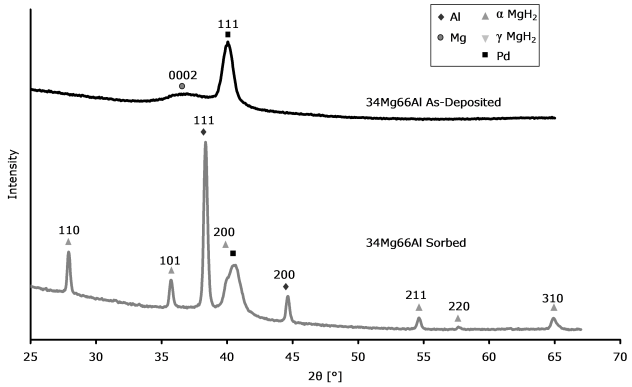

Figure 5.19: X-Ray Diffraction curves of as-deposited and sorbed 34Mg66Al, scaled independently for comparison of peak locations.

Mg grains are less prominent.

5.1.4 Neutron Reflectometry

Neutron reflectometry was performed on several samples of MgAl to investigate the nature of the physical geometry - including layer interface effects - of the film before and after sorption, and to determine where the absorbed hydrogen was located. Neutron reflectometry (NR) measures the reflectivity of a sample to neutrons at small angles; the reflectivity curve is a result of the geometry of the film, and can be fit with a Scattering Length Density (SLD) profile using the Parratt recursion algorithm (Section 2.5.4). The SLD of a given layer is dependent upon the material; particularly, hydrogen has a negative scattering length, so its addition to a layer should lower the SLD; density is also a factor, and so film expansion must be taken into account (Section 2.5.4).

A number of NR measurements were performed upon various MgAl films, however for the purposes of this study a single set of measurements will suffice; the 70Mg30Al set will be considered. Films were nominally 50nm of 70Mg30Al with a 10nm Pd cap. The reflectivity of the as-deposited 70Mg30Al is shown in Figure 5.20, and the reflectivity of the sorbed 70MgAl30 is shown in Figure 5.21; the corresponding SLD's are shown in Figure 5.22 and Figure 5.23 respectively. The frequency of the troughs of the reflectivity relates to the thicknesses of the layers within the stack (Section 2.5.4).

The SLD profile of the as-deposited film indicates that the nominal thickness was slightly off, with the Pd layer ~100Å as expected, and the MgAl layer slightly lower than expected at ~380Å. As a sanity check, the Pd SLD can be compared to the expected value for Pd of $4.02 * 10^{-6}$ (Section 2.5.4); the two values are the same in this case. There is additionally a thin spike between the MgAl layer and the Si substrate, which is SiO_2, the surface oxide of the Si.

The sorbed film's SLD profile is markedly different, as expected: the whole film is ~100Å thicker; the Pd thickness is slightly increased by ~75Å, and has a slightly less defined interface between it and the MgAl layer; and the MgAl layer is both thicker by ~25Å and has a significantly lower SLD of $\sim 1.5 * 10^{-6}$. This indicates the hydrogen has located itself in the MgAl layer. To verify that the drop in SLD is not due entirely to the lower density of the expanded film, the expected SLD from pure expansion can be calculated as $2.12 * 10^{-6}$, which is higher than the observed SLD, indicating the net difference is from hydrogen.

As an additional verification of the experimental methods, the composition of the MgAl can be calculated; it is nominally 70Mg30Al, but can be calculated more precisely using the SLD of the layer and the expected SLD's of Mg and Al (Section 2.5.4). This results in a calculated composition of 86.9Mg13.1Al; while this is significantly different from the nominal, it is considered within the error of the sputter machine for short sputtering durations (less than two minutes), as the mechanical apparatus to open and close guns are not instantaneous or always equal (Section 2.5.1).

5.1.5 Kinetics

Kinetic measurements were performed in order to determine the hydrogen storage capacity and cyclability of several MgAl compositions. Experiments were conducted with a Sieverts apparatus in accordance with Section 4.2.3: a 1.5μm released film of MgAl alloy with 7.5nm Pd and Ta caps, all totalling 20-30mg (this method is obviously not suited for mass production, but it is a useful rapid characterization method). The measurements cycle the material through absorbed and desorbed states at temperature, in order to determine hydrogen sorption capability over a large number of sorption and desorption cycles. The number of cycles performed is in the hundreds (realk world mobile

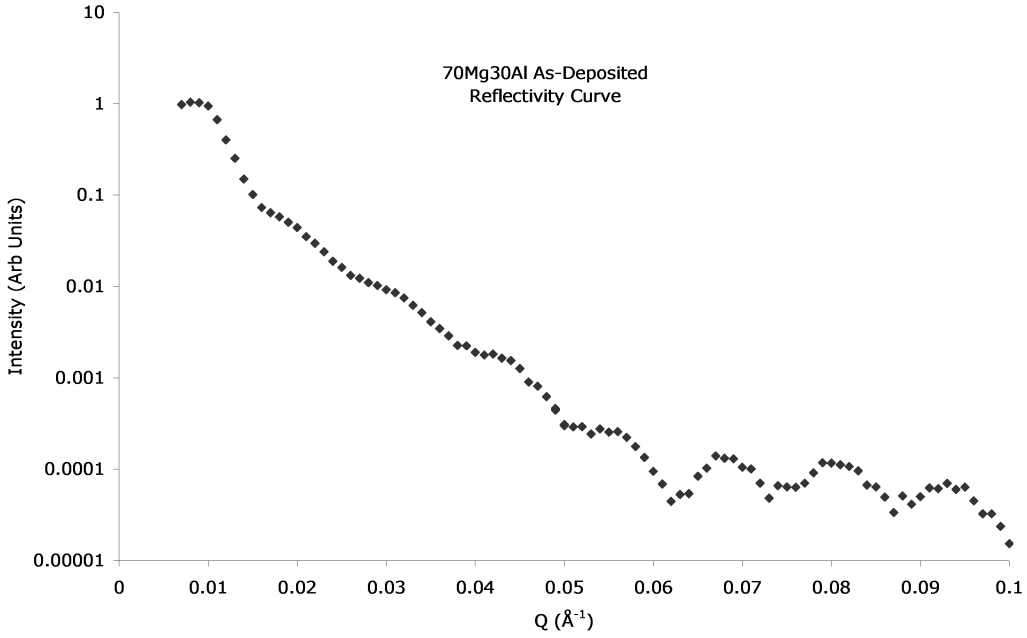

Figure 5.20: The NR reflectivity curve of as-deposited 70Mg30Al.

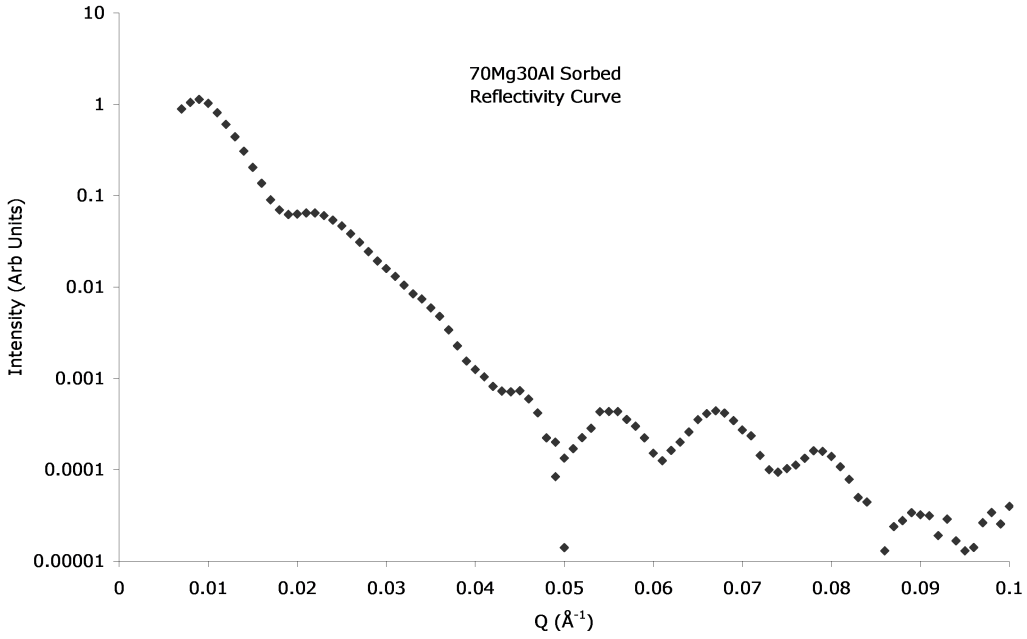

Figure 5.21: The NR reflectivity curve of 70Mg30Al sorbed at 200C.

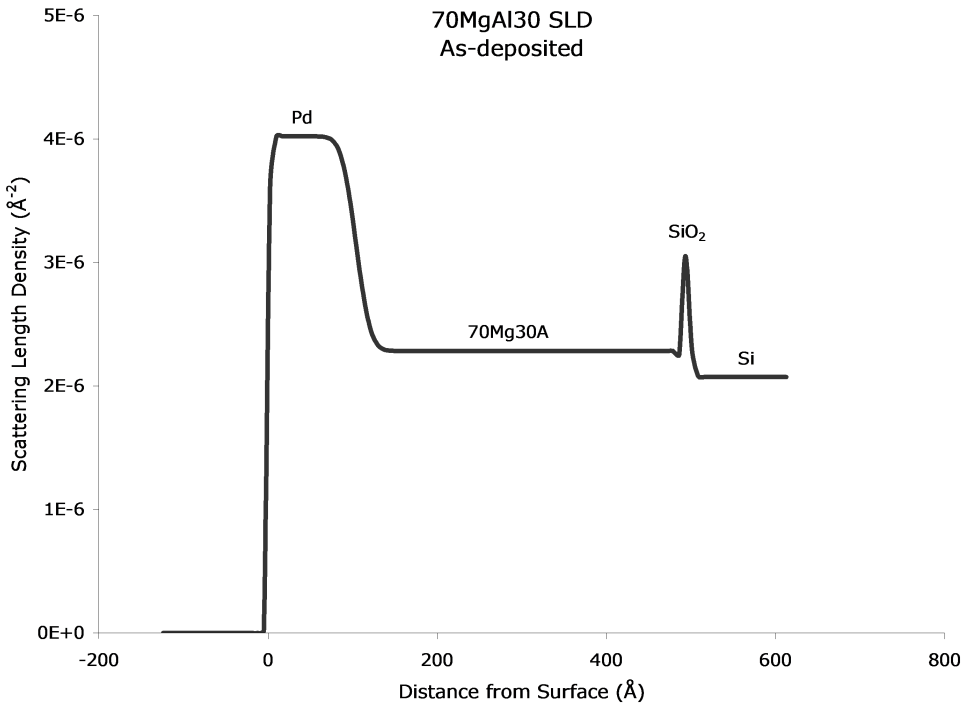

Figure 5.22: The Scattering Length Density (SLD) profile fit corresponding to the reflectivity of as-deposited 70Mg30Al, shown in Figure 5.21. The SLD indicates the thicknesses and roughnesses of each layer of the film, and can be used to determine their composition.

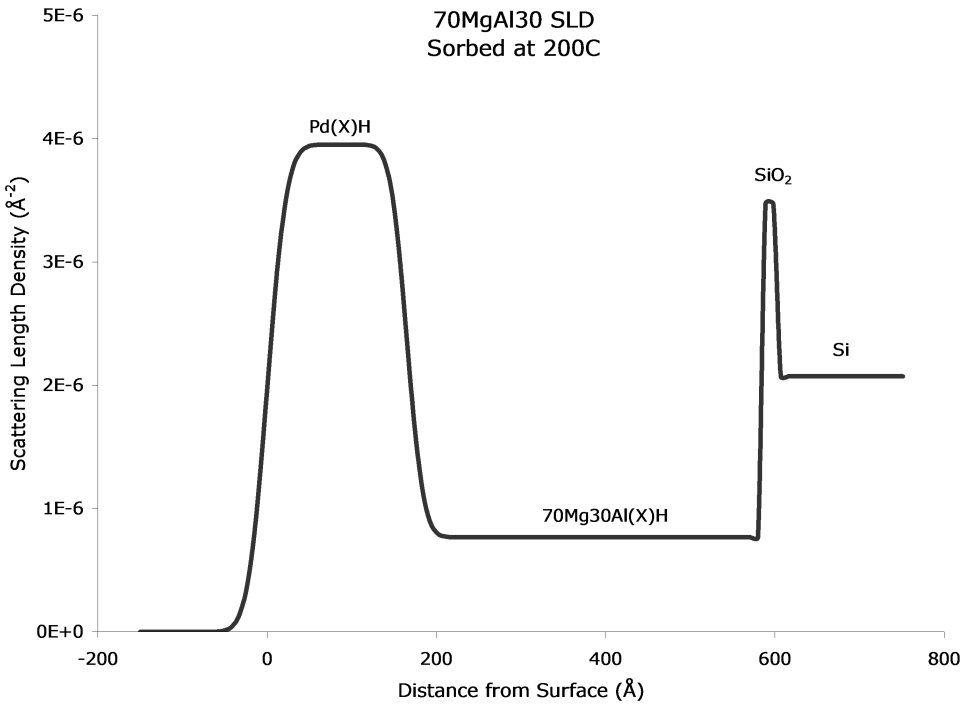

Figure 5.23: The Scattering Length Density (SLD) profile fit corresponding to the reflectivity of 70Mg30Al sorbed at 200C, shown in Figure 5.21. The SLD indicates the thicknesses and roughnesses of each layer of the film, and can be used to determine their composition.

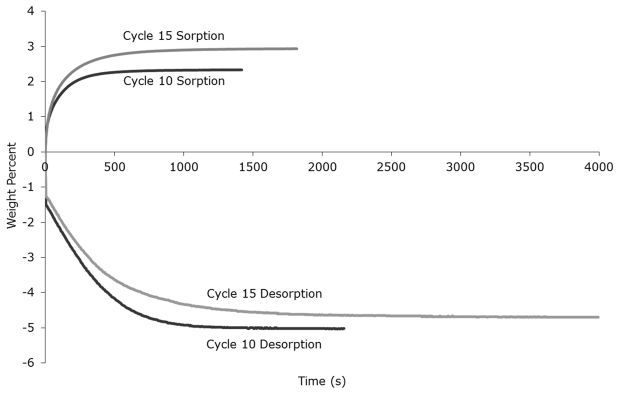

Figure 5.24: Example sorption and desorption curves for 80Mg20Al, cycles 10 and 15.

applications would require orders of magnitude more than this, but it is first necessary to reach this point), which necessitates a broader view of the trends of the cycling. The compositions examined in this study were 80Mg20Al, 70Mg30Al and 60Mg40Al. None of the curves were able to be fit completely by either CV or KJMA, but the early portions of many resemble one model or the other.

The first composition examined was 80Mg20Al; example curves shown in Figure 5.24 demonstrate typical absorption and desorption behaviour of MgAl samples. The cycles shown have rapid absorption which flattens out rapidly; the curves have a section which appears linear, like the top 70% of a KJMA curve. Keeping in mind that these cycles are the tenth cycle and beyond, the initial nucleation is not observed as there have already been hydride particles nucleated in previous cycles, some nuclei of which are expected to remain after desorption, enhancing the initial absorption rate; this also implies that there is some non-reversible capacity, and desorption is never 100% complete. The desorption curves are much slower than the absorption, and appear more curved than the sorption curves, yet still display some of the linear part of the early-middle curve, characteristic of the KJMA model.

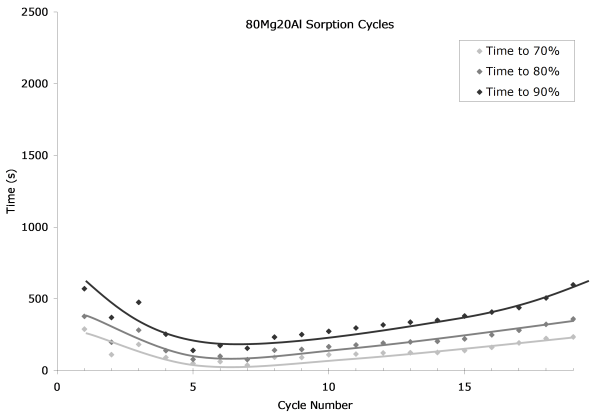

Figure 5.25: Absorption trends in terms of time to a given percentage of maximum capacity for 80Mg20Al.

Two interesting issues with the Sieverts Apparatus used are notable here: firstly, the desorption curves appear to jump vertically, primarily due to initial data recording beginning slowly after the sample was equilibriated with the vacuumed volumes, an effect which was mitigated with accelerated recording; and secondly, the desorption and absorption curves do not have the same totals. This method has two notable sources of error: the sample is further vacuumed out for 5 minutes after each desorption cycle; and slow initial recording of extremely rapid initial absorption can cause the sorption data to be underreported; these were mitigated by lowering the cutoff rate and accelerating the initial recording rate, respectively.

The cycling of the 80Mg20Al, sorption shown in Figure 5.25 and desorption shown in Figure 5.26, has an initial peak of slower absorption and desorption times, which settles from around 500s for 90% sorption and more than 2000s for 90% desorption towards 250s sorption and 900s desorption; the sorption capability slowly begins to degrade over 10 cycles, and desorption rapidly degrades above 15 cycles. This makes it unsuitable for long term cycling.

The 70Mg30Al sample was somewhat slower than the 80Mg20Al sample; example curves, shown in Figure 5.27 demonstrated significantly higher absorption

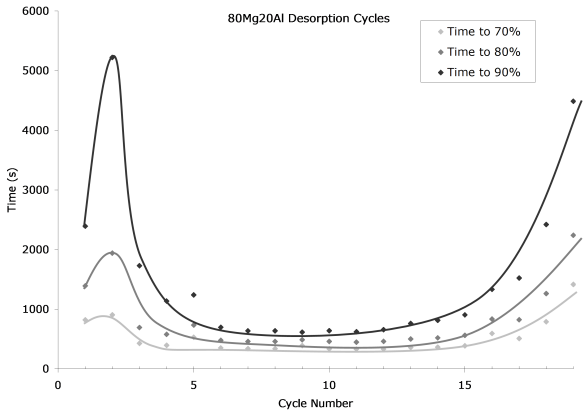

Figure 5.26: Desorption trends in terms of time to a given percentage of maximum capacity for 80Mg20Al.

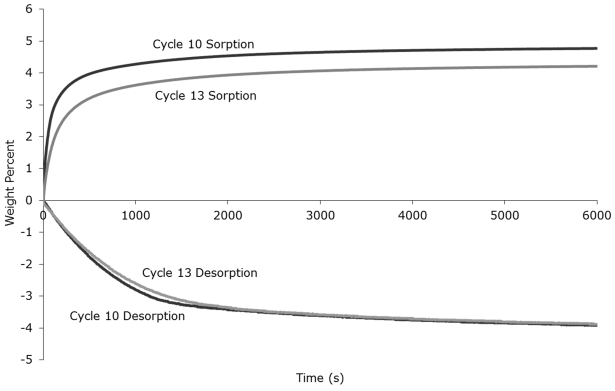

Figure 5.27: Example sorption and desorption curves for 70Mg30Al, cycles 10 and 13; cycle 13 was used rather than cycle 15 due to cycling being terminated at that cycle number.

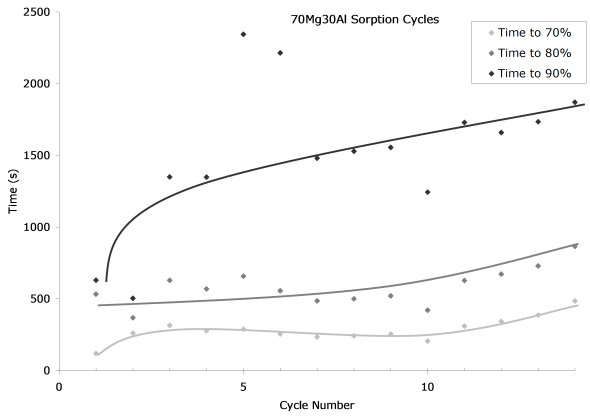

Figure 5.28: Absorption trends in terms of time to a given percentage of maximum capacity for 70Mg30Al.

maximums, but flattened out far less quickly than 80Mg20Al. Desorption also appears slower, though less so than the difference in absorption. The absorption curves show a linear section like KJMA, but the desorption curves do not, matching the CV model better; the differences between the curves are due to the difference in driving force of the sorption processes; the equilibrium pressure at 200°C is ~0.05 bar, which puts the absorption pressure at over 50 times the equilibrium pressure, while the equilibrium pressure is only 10 times the desorption pressure.

The cycling trends of the 70Mg30Al sample, shown in Figures 5.28 and 5.29, were significantly different than the 80Mg20Al; while it had a similar peak in desorption times initially, it also stayed fairly slow in desorption throughout cycling, and with visible degradation in times; during sorption it started with quicker uptake, but degraded beyond 80Mg20Al within the first few cycles and continued degrading significantly with further cycling.

The 60Mg40Al was by far the fastest of the series and the most stable; it was cycled over 400 times, and while significant degradation did occur, it was fairly slow, as can be seen in Figure 5.30 comparing four cycles over the extended range. The absorption is interesting in that it shows two abrupt

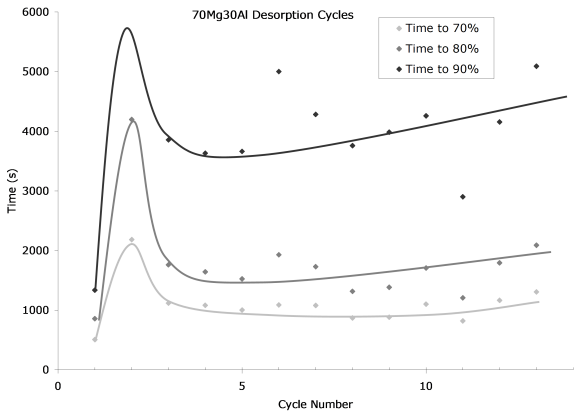

Figure 5.29: Desorption trends in terms of time to a given percentage of maximum capacity for 70Mg30Al.

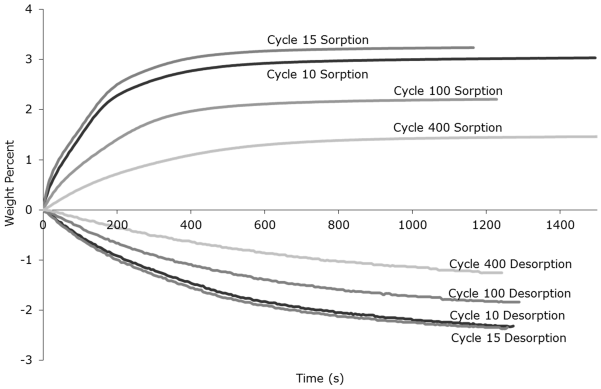

Figure 5.30: Example sorption and desorption curves for 60Mg40Al, cycles 10, 15, 100 and 400.

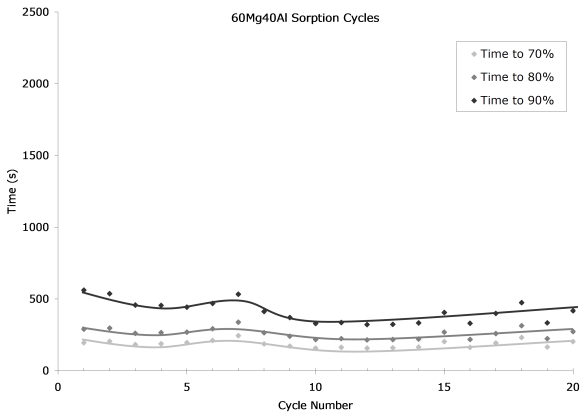

Figure 5.31: Absorption trends in terms of time to a given percentage of maximum capacity for 60Mg40Al.

changes in slope, something not seen in either KJMA or CV; this suggests that either another model is needed, or one of the models is convoluted with other factors; it does show linear sections, suggesting a modified KJMA. The desorption curves show no linear sections, suggesting CV-like behaviour.

The cycling trends are presented in two parts; this sample was tested after the previous samples, and as a result of its good performance it was allowed to continue cycling. In the first set of figures, Figures 5.31 and 5.32, cycles are shown on similar scales to the previous samples; the second set, Figures 5.33 and 5.34, extended cycling is shown. In the first set, sorption starts slightly higher over the first few cycles and then settles somewhat from 10 to 15 cycles; desorption remains constant over this period; both sorption and desorption are faster than 70Mg30Al and comparable to the fastest portions of 80Mg20Al, but it doesn't display the degradation of either. In the second set of figures, extended cycling, it is observed that both sorption and desorption degrade slowly over 400 cycles, however final performance is not significantly different from initial performance. It is as fast as 80Mg20Al is and over twice as fast as the 70Mg30Al for sorption even at the end of 400 cycles; in desorption, it is slightly faster at the end of 400 cycles than the 80Mg20Al was at its best and over three times faster than the 70Mg30Al.

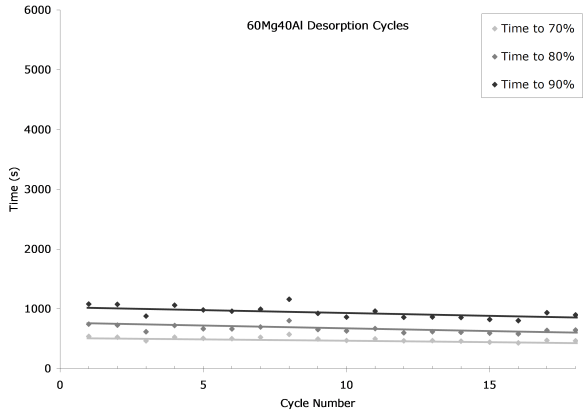

Figure 5.32: Desorption trends in terms of time to a given percentage of maximum capacity for 60Mg40Al.

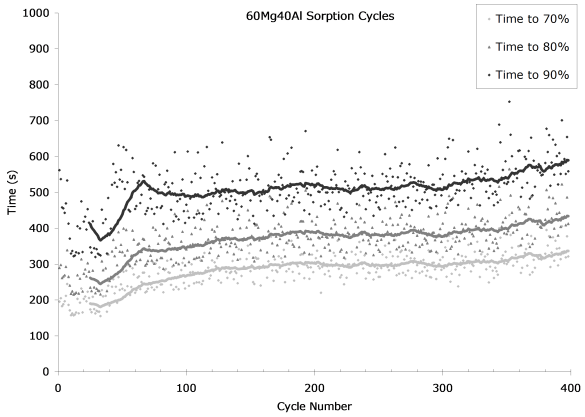

Figure 5.33: Absorption trends in terms of time to a given percentage of maximum capacity for 60Mg40Al.

Figure 5.34: Desorption trends in terms of time to a given percentage of maximum capacity for 60Mg40Al.

These differences are more than one might expect from the compositional changes involved, and when considering some of the experimental conditions a possible explanation can be observed: The 80Mg20Al and 70Mg30Al were sputtered first, at a higher base pressure of around $2.5 * 10^{-7}$ torr, whereas the later samples were sputtered at lower pressures in the low 10^{-8}'s due to seasonal humidity changes and improvements in sputtering techniques; the difference in oxygen contamination could quite possibly slow hydrogen travel through grain boundaries.

An overview of the maximum weight percentage of absorption and desorption in each composition is shown in Figure 5.35 and Figure 5.36 respectively; while the data has high variance, trends can nonetheless be observed readily. In sorption, the 70Mg30Al holds the most hydrogen - around 4% - while the 80Mg20Al and 60Mg40Al hold less at or slightly below 3%; they appear fairly stable in maximum uptake, with a possible downward trend for 70Mg30Al. The desorption curves are somewhat different, with the 70Mg30Al and 80Mg20Al desorbing the most hydrogen - around 4% - and trending slightly downwards, while 60Mg40Al is relatively stable at around 3%. The difference between absorption and desorption for 80Mg20Al suggests that the absorption data has

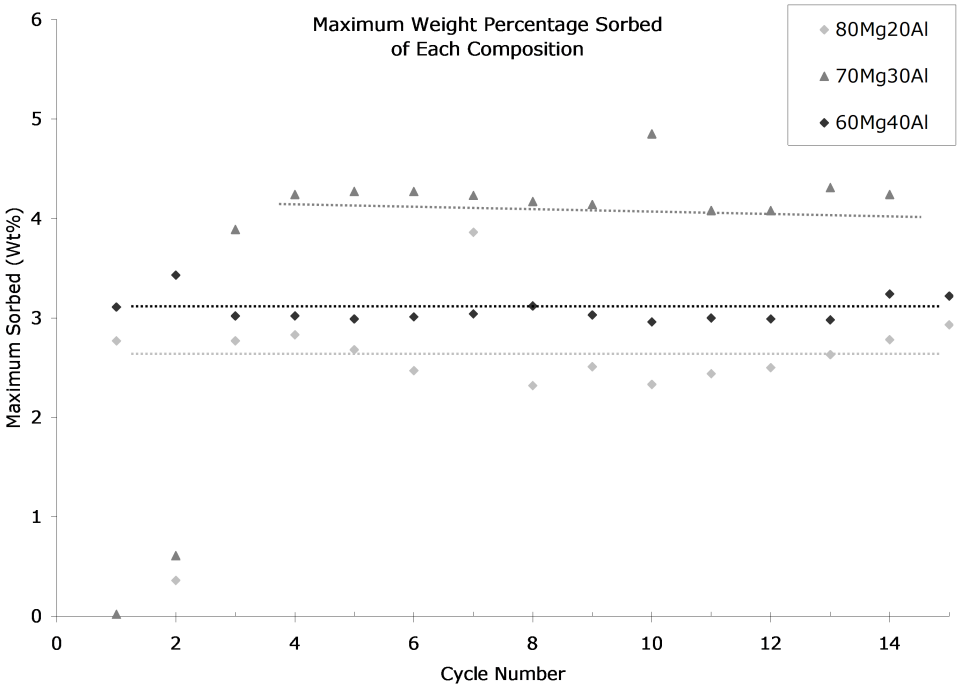

Figure 5.35: The maximum weight percentage absorbed of each composition for each of 15 cycles.

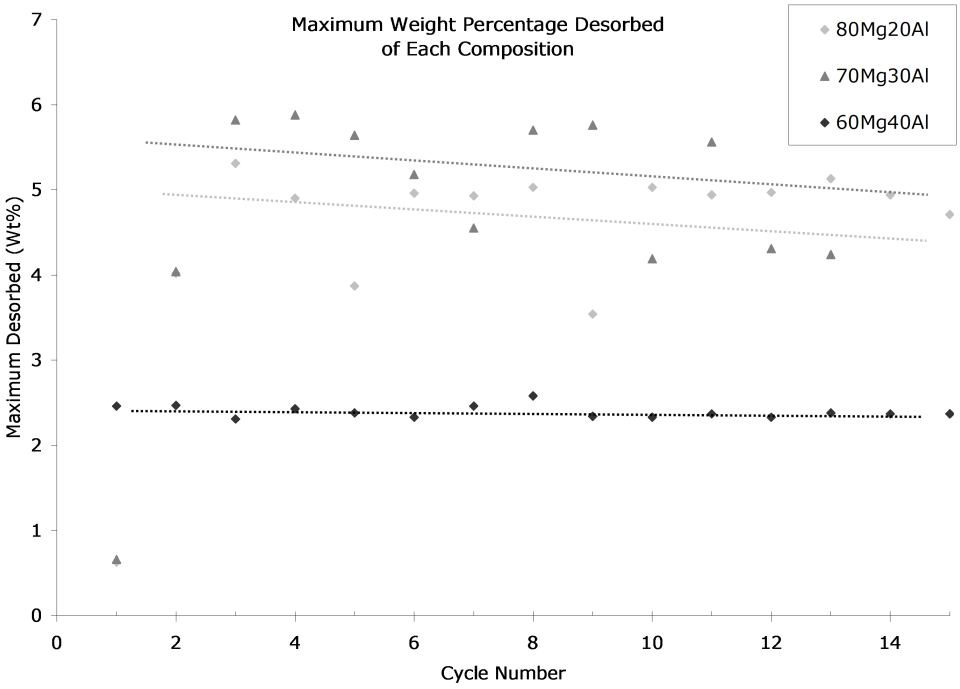

Figure 5.36: The maximum weight percentage desorbed of each composition for each of 15 cycles.

been under-reported - however, the main trend is clear, that sorption maximums remain stable, and desorption maximums are close to stable, with slow degradation.

Comparing the trends in the maximum weight percentages with the trends in the time to a percentage of the maximum, it can be seen that the overall capacity is remaining relatively stable, but for 80Mg20Al and 70Mg30Al the time to fill or empty that capacity greatly increases over time, while 60Mg40Al is relatively stable through 400 cycles, though with a lower total capacity.

5.2 MgAlTi

The second set of materials studied was MgAlTi, and again as discussed in Section 2.4.1, the high-Mg end was of primary interest; furthermore, the ratios of Al:Ti of interest were those of the possible AlTi intermetallics, specifically 3:1, 2:1, 1:1 and 1:3, as a possible method to modify the sorption behaviour; samples were created as discussed in Section 4.1.1. Three primary investigative tools were used on MgAlTi: the Sieverts Apparatus and XRD as in MgAl, and additionally the HPDSC. Initial exploration of the phase space of MgAlTi started at the 70% Mg range where MgAl had been tested successfully; additionally, higher and lower fractions of Mg, 60% and 85% were made for comparison, the latter representing halfway to 100% Mg; when 85% Mg had better initial results than 70% Mg, the investigation was focused on that concentration.

5.2.1 High-Pressure Differential Scanning Calorimetry

The High Pressure Differential Scanning Calorimeter, or HPDSC, was used to determine the enthalpy of hydride - in essence to determine the species

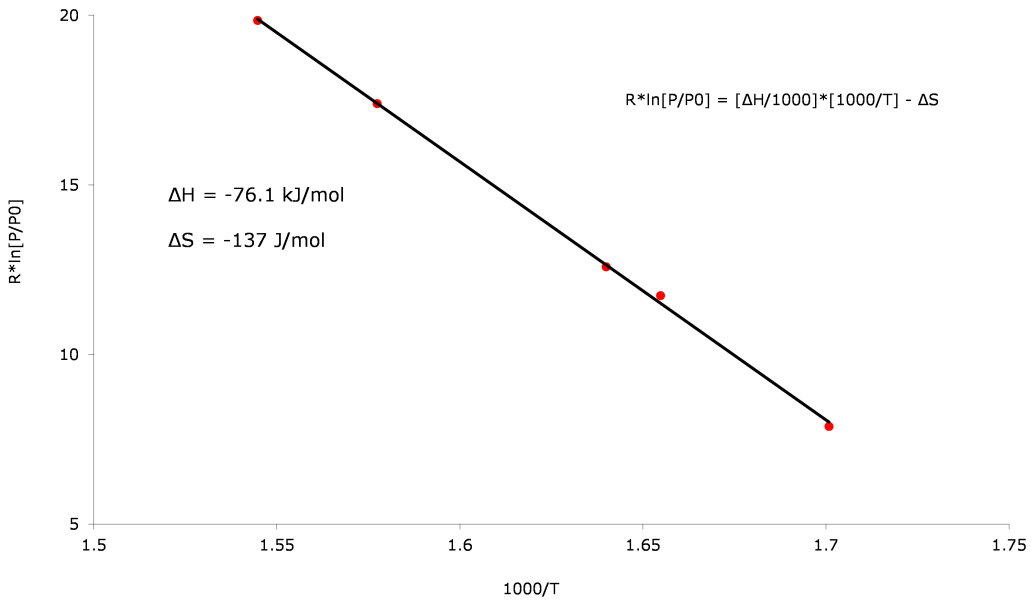

Figure 5.37: A plot of absorption peaks found in the HPDSC for 70Mg20Al10Ti to make a *van't Hoff* plot, as in Equation 2.1.4, to determine ΔH and ΔS.

of hydride being formed, as discussed in Section 2.1. The 1:1 and 2:1 Al:Ti compositions of the 70% series were tested, shown in Figures 5.37 and 5.38. Resulting in enthalpies of formation of -76.1 kJ/mol and -80.8 kJ/mol for 70Mg20Al10Ti and 70Mg15Al15Ti, respectively, both suggest the ΔH of MgH_2 (Section 2.4); the observed entropies of formation also agree with those typical of metal hydrides (Section 2.1). The HPDSC runs each had a single absorption peak, which indicates a single species; each peak was plotted as a point in Figures 5.37 and 5.38.

The results indicate that there is no positive change in enthalpy of hydride formation in MgAlTi over MgH_2 as had been desired in Section 2.4, and strongly indicates that the hydrogen is being stored as MgH_2. Additionally, we can calculate the equilibrium H_2 pressure using the *van't Hoff* equation (Equation 2.1.4); it is 0.057 bar at 473K.

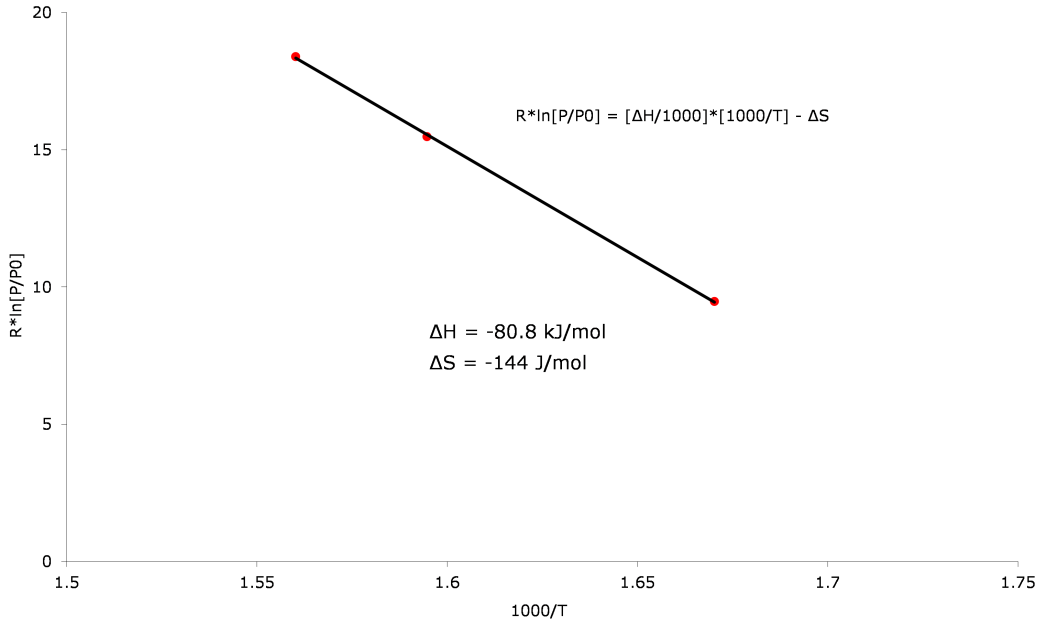

Figure 5.38: A plot of absorption peaks found in the HPDSC for 70Mg15Al15Ti in pressure and temperature modified to make a *van't Hoff* plot, as in Equation 2.1.4, to determine the enthalpy of hydride formation, ΔH, and the entropy of hydride formation, ΔS.

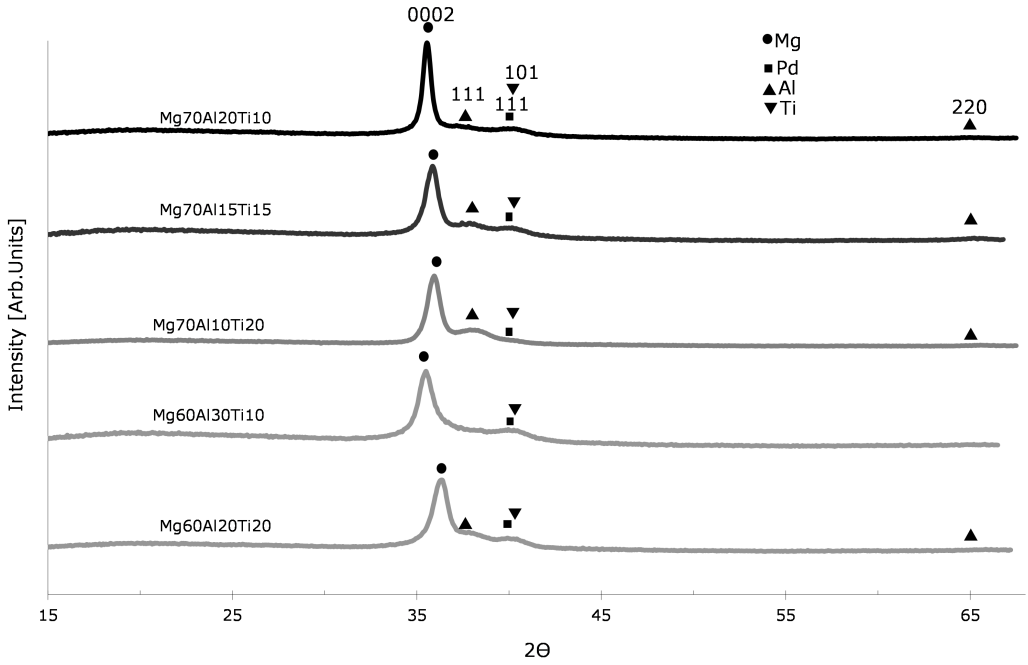

Figure 5.39: The as-deposited XRD patterns of various MgAlTi compositions; as additional Al or Ti is added, the Mg {0002} peak shifts to higher 2θ especially with addition of Ti.

5.2.2 X-Ray Diffraction

X-Ray Diffraction, or XRD, was performed on several of the Al:Ti ratios, to determine the phases being formed in the material. XRD of various as-deposited on-wafer Al:Ti ratios, in Figure 5.39, confirmed that MgAlTi behaves just like MgAl (Figure 5.11) in the as-deposited state, as expected; a shifting Mg (JCPDS Card no. 89-4244) {0002} peak is the dominant feature, the peak shifting towards higher 2θ as more Al (JCPDS Card no. 4-787) or Ti (JCPDS Card no. 89-5009) is added, with greater shifts seen for additional Ti than additional Al. Slight humps are observed for Al at 38.5°; there also appears a hump at around 40° to 41° which corresponds to both the Pd (JCPDS Card no. 46-1043) {111} and Ti {101} at 40.1° and 40.25° respectively.

Samples cycled in the Sieverts apparatus - Section 5.2.3 - were stopped at

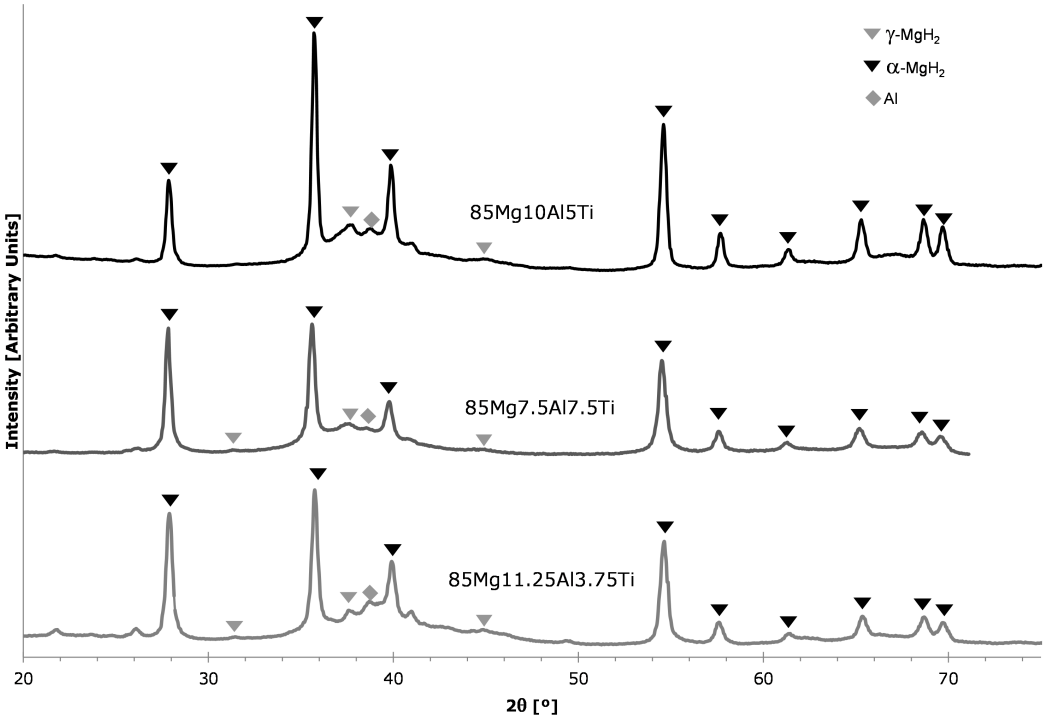

Figure 5.40: XRD patterns of absorbed samples of MgAlTi compositions; samples were cycled in the Sieverts apparatus (Section 4.2.3)

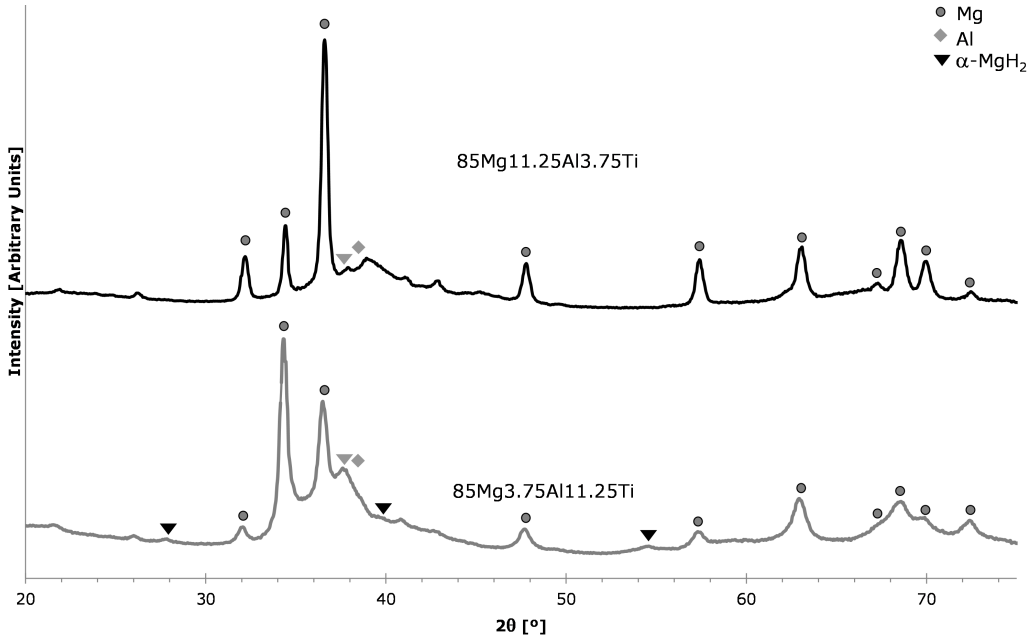

Figure 5.41: XRD patterns of desorbed samples of MgAlTi compositions; samples were cycled in the Sieverts apparatus (Section 4.2.3)

the conclusion of either an absorption or desorption stage in order to provide absorbed and desorbed samples after having been cycled numerous times.

The absorbed samples, shown in Figure 5.40, include the 3:1, 2:1 and 1:1 Al:Ti ratios, and show primarily α-MgH_2(JCPDS Card no. 12-697), visible at 27.9°, 35.7°, 39.9°, 54.6°, 57.8°, 61.3°, 65.3°, 68.8°, and 69.8°; these are the dominant peaks of this series. This agrees with the HPDSC results in finding MgH_2 as the predominant hydrogen storing phase. Additional peaks include small γ-MgH_2 peaks at 31.5°, 37.7° and 45.0°, which is not unexpected given its appearance in MgAl, however its presence is much reduced. An Al peak is also found at 38.5°. A small peak at 40.9° does not match any of the expected phases or even unexpected hydrides considered: none of the four Al_xTi_y alloys match, nor AlH_3, nor $Al_{12}Mg_{17}$.

Both the absorption and desorption series show a broad hump from approximately 33° to 43°, which could be explained as a broad range of d-spacings

arising from a disordered matrix including Mg, Al and Ti, which each have primary peaks in the region. This aspect of the patterns has not been fully elucidated.

The desorbed series, shown in Figure 5.41, is the expected counterpart of the absorbed series, with the majority phase being Mg; all the dominant peaks are Mg, with peaks at 32.2°, 34.4°, 36.6°, 47.8°, 57.4°, 63.1°, 67.3°, 68.6°, 70.0°, and 72.5°. There are additional peaks of α-MgH_2 which did not fully desorb at 27.9°, 39.9° and 54.6°, as well as an Al shoulder on a peak at 38.5°. The small peak noted at 40.9° in the absorbed sample is also present, indicating that its progenitor was not involved in storing hydrogen. There is an additional small peak at 42.8° which cannot be accounted for under the same criteria as the 40.9° peak, but again is clearly a minority phase.

5.2.3 Kinetics

Cycling in the Sieverts apparatus was done for a number of samples - as mentioned at the beginning of the section, organized into 7-%, 85% and 1:1 Al:Ti for comparison. The individual cycles are presented in order of increasing Mg fraction. The findings of the HPDSC and XRD sections - that no significant enthalpy of hydride formation adjustments had been made and α-MgH_2 was the hydrogen carrying phase - were evident in the Sieverts cycling as well, as the temperature of cycling could not be lowered from the 200°C of MgAl, as the samples would not cycle below that temperature. Pressures were held the same at ~3bar for absorption and ~5mbar for desorption, as described in Section 4.2.3. Scales on graphs have been kept similar with desorption kept at 2500s, and absorption at 250s for the 85%Mg series and 500s for others.

The absorption cycles of the first composition, 60Mg20Al20Ti a 1:1 Al:Ti composition shown in Figure 5.42 has a high initial starting absorption time, during what is presumed to be nucleation and growth of hydride grains (Section

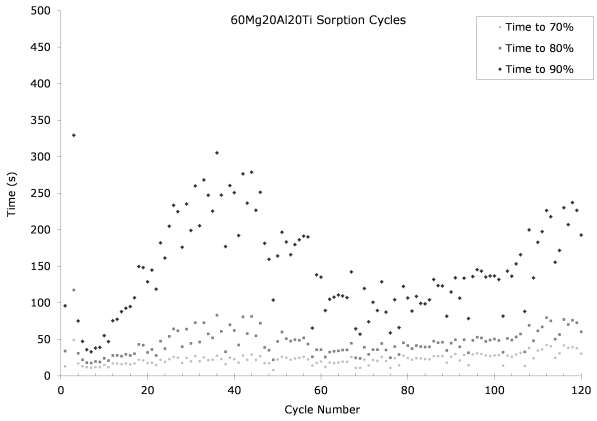

Figure 5.42: Times to percentages of maximum hydrogen absorbed for 60Mg20Al20Ti over 120 cycles.

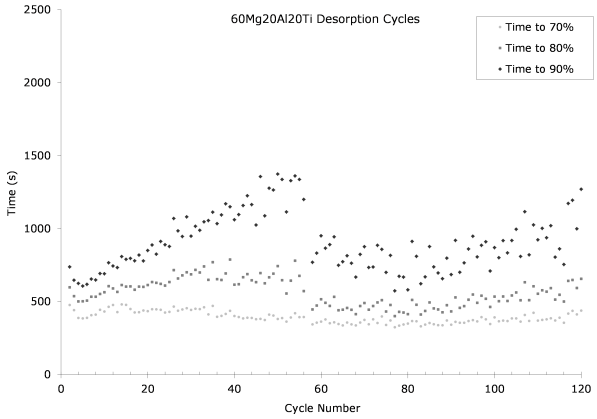

Figure 5.43: Times to percentages of maximum hydrogen desorbed for 60Mg20Al20Ti over 120 cycles.

Figure 5.44: Times to percentages of maximum hydrogen absorbed for 70Mg7.5Al22.5Ti over 120 cycles.

2.2.3); absorption quickly settled to below 50 seconds to 90% of maximum; time to 70% remained relatively stable with a slow increase over 120 cycles; time to 90%, however, was not stable, increasing for 40 cycles, decreasing again until cycle 60, and finally increasing once more. It remained at less than 250 seconds to 90% and below 50 seconds to 70% of maximum for the entire 120 cycles. The desorption of 60Mg20Al20Ti, shown in Figure 5.43, is similar in its stability of the 70% of maximum - at less than 500 seconds per cycle - with an increase for approximately 50 cycles of the 90% before falling again until cycle 80, where it begins climbing again. The desorption is almost an order of magnitude slower than absorption, a trait held by all of the MgAlTi series. The trend of the composition towards the end of the run is increasing in time to a given percentage, for both absorption and desorption.

The 70Mg7.5Al22.5Ti - a 1:3 Al:Ti composition - absorption cycles, shown in 5.44, quickly settle to below 50 seconds for time to 90% of maximum absorbed, but increases steadily to 100 seconds by cycle 20, whereupon it stabilizes with a slight increase in time starting at cycle 40. Time to 70% and 80% are both stable - with slight upwards trends from cycle 20 onwards - at less than 25 and 50 seconds, respectively. The desorption for the 70Mg7.5Al22.5Ti (Figure

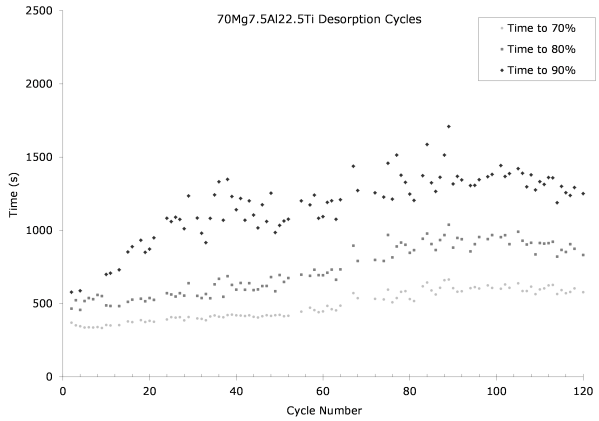

Figure 5.45: Times to percentages of maximum hydrogen desorbed for 70Mg7.5Al22.5Ti over 120 cycles.

5.45) started from 500 seconds for 90% desorption and increased to just above 1000s by cycle 40, with a slow ramp towards 1500s by 120 cycles. Time to 70% and 80% start from below 500s and just above 500s, respectively, with slow increases over the whole range to just above 500s and just below 1000s, respectively. Both absorption and desorption have trends of increasing time over the cycling range after the initial drop.

Absorption of the 70Mg15Al15Ti, a 1:1 Al:Ti composition, was the fastest of the 70% Mg series, as shown in Figure 5.46. Absorption time started high as is typical, but rapidly settled to below 25 seconds for 90%, and remained stable at that level for the remainder of the range; this run was halted at 80 cycles. Desorption also remained stable after 10 cycles, as can be seen in Figure 5.47, with 70%, 80% and 90% settling to approximately 300s, 500s and 750s, respectively. Absorption and desorption are both stable over the course of this run.

The 70Mg20Al10Ti, a 2:1 Al:Ti composition shown in Figure 5.48, was much slower than the previous; it starts high and drops to below 100 seconds, 50s and below 50s for 90%, 80% and 70%, respectively, by 10 cycles. A long slow hump with a peak at 50 cycles of below 200s, below 100s and below 50s follows

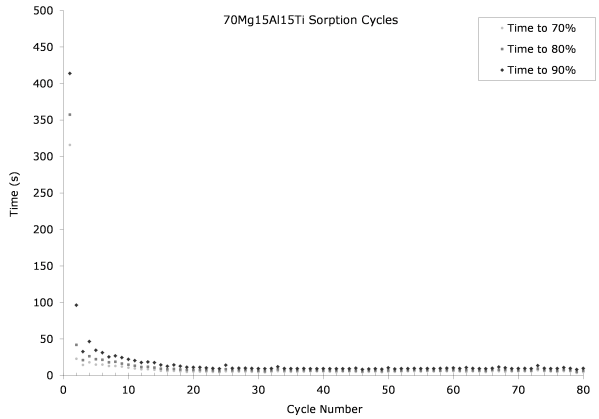

Figure 5.46: Times to percentages of maximum hydrogen absorbed for 70Mg15Al15Ti over 80 cycles.

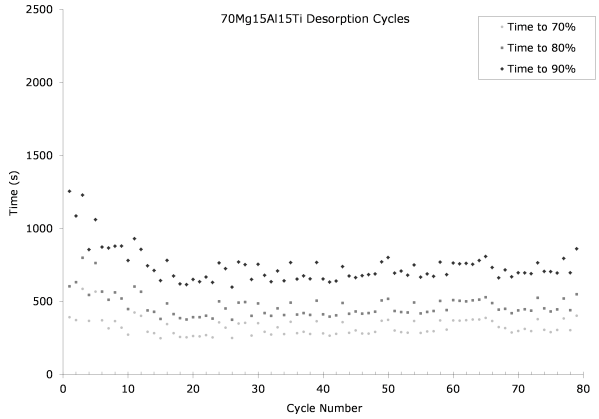

Figure 5.47: Times to percentages of maximum hydrogen desorbed for 70Mg15Al15Ti over 80 cycles.

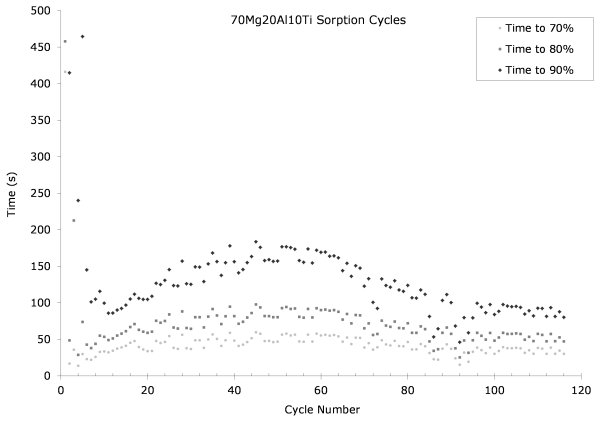

Figure 5.48: Times to percentages of maximum hydrogen absorbed for 70Mg20Al10Ti over 120 cycles.

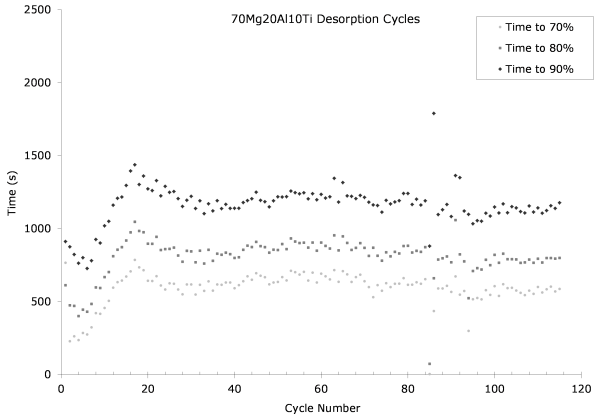

Figure 5.49: Times to percentages of maximum hydrogen desorbed for 70Mg20Al10Ti over 120 cycles.

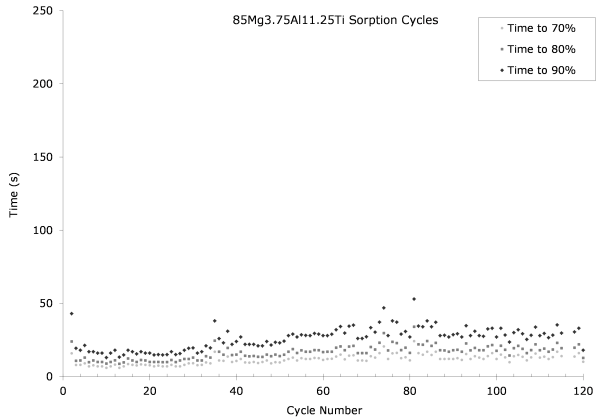

Figure 5.50: Times to percentages of maximum hydrogen absorbed for 85Mg3.75Al22.5Ti over 120 cycles.

for 90%, 80% and 70%, before settling to approximately their previous values for the remainder of the run. Its desorption cycles, in Figure 5.49, have a peak just before 20 cycles of 1500s, 1000s and 750s for 90%, 80% and 70% respectively, before settling to approximately 1200s, 800s and 600s, at which they remain stable for the rest of the run. The desorption is stable across the run, and the absorption is stable by the end of the run.

The 85% Mg series has faster absorption on average than 60% or 70% Mg; consequently, the vertical scale has been halved to 250 seconds; the desorption scale remains the same. The 85Mg3.75Al11.25Ti (1:3 Al:Ti), in Figure 5.50, has rapid absorption starting below 25 seconds after the initial peak for 90%, with a slow increase to approximately 35s by cycle 80, where it remains stable for the remainder of the run; 80% and 70% follow the same trends but stabilize below 25 seconds. Desorption, in Figure 5.51, is relatively stable the whole run, with a slight increase at 70 cycles; the times to 90%, 80% and 70% stabilize at approximately 100s, 800s and 600s over the last 40 cycles, being quicker by roughly 100s each before cycle 70. The last 40 cycles of both absorption and desorption are stable.

The 1:1 Al:Ti composition is again the fastest in its series; 85Mg7.5Al7.5Ti

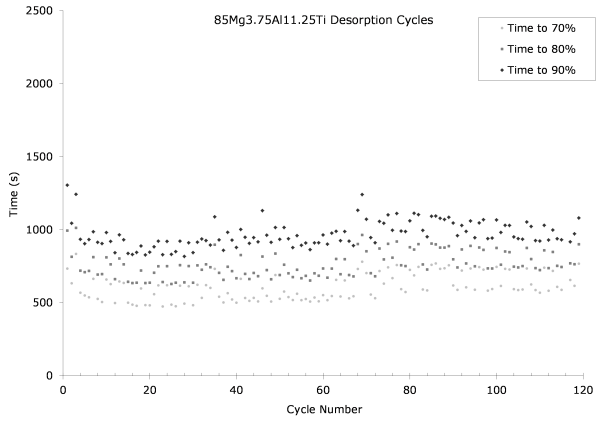

Figure 5.51: Times to percentages of maximum hydrogen desorbed for 85Mg3.75Al22.5Ti over 120 cycles.

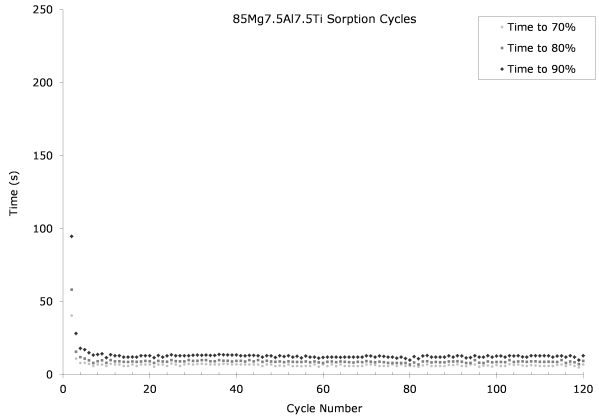

Figure 5.52: Times to percentages of maximum hydrogen absorbed for 85Mg7.5Al7.5Ti over 120 cycles.

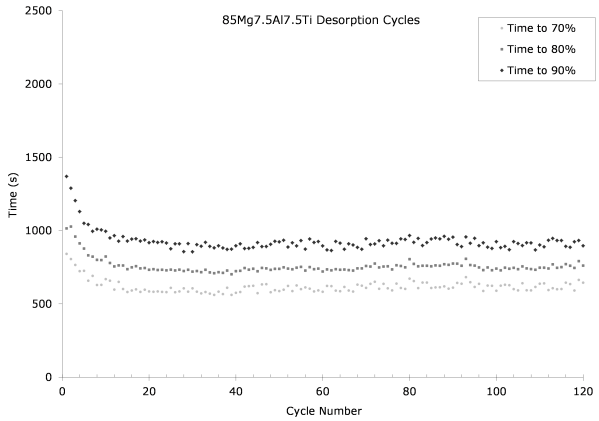

Figure 5.53: Times to percentages of maximum hydrogen desorbed for 85Mg7.5Al7.5Ti over 120 cycles.

absorption, shown in Figure 5.52, stabilizes below 15 seconds for 90% of maximum within 10 cycles, and remains there through 120 cycles. Its desorption (Figure 5.53) was similarly stable, settling below 1000s, 750s and 500s after 20 cycles, for time to 90%, 80% and 70% of maximum respectively, and maintaining those levels for the subsequent 100 cycles. Both absorption and desorption of this composition are quite stable.

The absorption of 85Mg10Al5Ti, the 2:1 Al:Ti of the 85% series, looks stable at first glance, as seen in Figure 5.54, but there is a slow steady increase from the first settled cycles around cycle 10 until the end; time to 90%, 80% and 70% of maximum start below 25s, 15s and 10s and gradually increase to around 50s, 25s and 20s, respectively. Its desorption, Figure 5.55, shows this trend more readily; there is a steady increase from around 1100s, 900s and 500s, for 90%, 80% and 70% to approximately 1400s, 1250s and 1000s by 120 cycles. This compositions trend is increasing time for both absorption and desorption.

Absorption of the 85Mg11.25Al3.75Ti (Figure 5.56) consists of a large asymmetric hump starting around 10 cycles, peaking between 40 to 70 cycles and stretching to 120 cycles, at which point it is still decreasing. The start is at 50 seconds, 30s and 25s for 90%, 80% and 70% respectively, the peak approx-

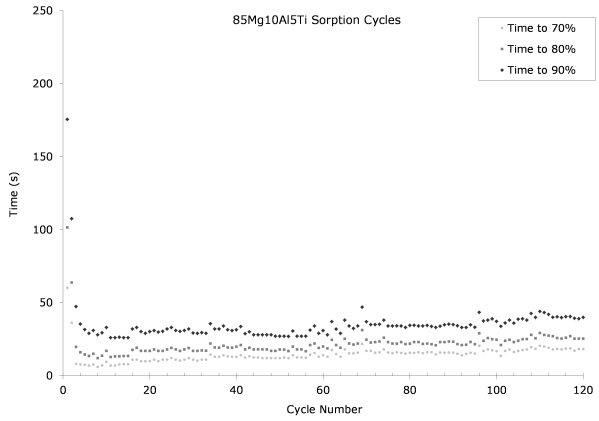

Figure 5.54: Times to percentages of maximum hydrogen absorbed for 85Mg10Al5Ti over 120 cycles.

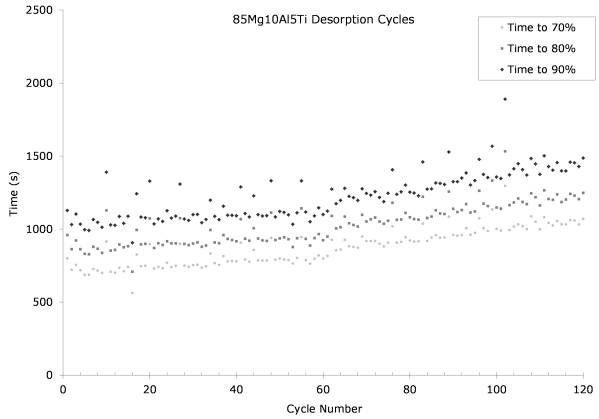

Figure 5.55: Times to percentages of maximum hydrogen desorbed for 85Mg10Al5Ti over 120 cycles.

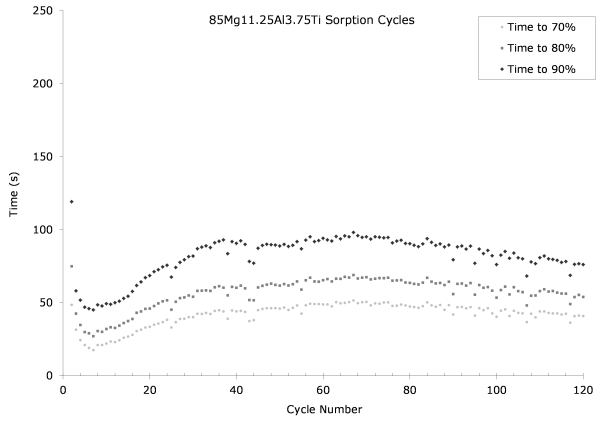

Figure 5.56: Times to percentages of maximum hydrogen absorbed for 85Mg11.25Al3.75Ti over 120 cycles.

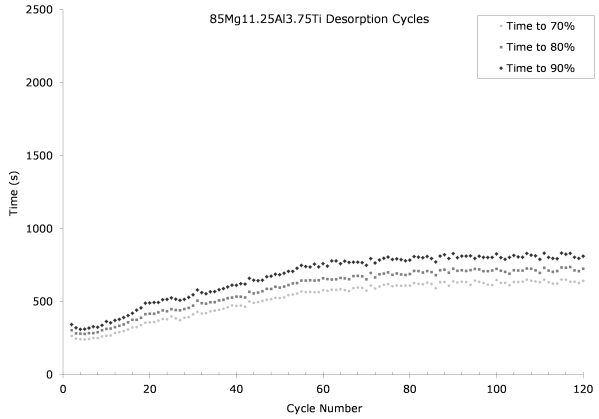

Figure 5.57: Times to percentages of maximum hydrogen desorbed for 85Mg11.25Al3.75Ti over 120 cycles.

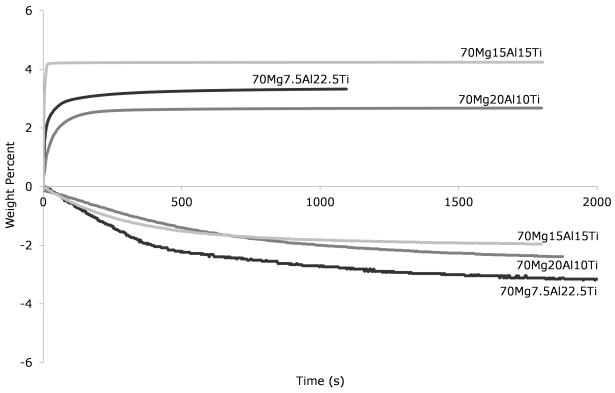

Figure 5.58: Cycle 80 curves of the samples from the 70% series of MgAlTi.

imately 100s, 70s, and 50s, while the values at 120 cycles are approximately 80s, 60s and 40 seconds. The desorption, in Figure 5.57, is unusual in that it trends the opposite direction as the final absorption trend: desorption begins relatively quickly, with time to 90%, 80% and 70% of maximum all between 200 and 350 seconds, but rapidly trends upwards to approximately 750s, 650s and 550s by cycle 60; thereafter the trend is upwards much more gradually, each of 90% 80% and 70% gaining around 50 seconds. While this is almost stable, it is increasing, and the desorption is clearly not stable either, being in a decreasing trend towards the end of its run.

What becomes clear is that the first 10 to 20 cycles are typically completely different from the rest of the run especially in absorption; nucleation and growth of hydride grains during this period is proposed as the reason for this. Thus, when considering the characteristic behaviour of a sample, the first 20 cycles should be discounted. Additionally, while most of the time absorption and desorption follow the same trends, there are exceptions.

Examining individual cycles of the 70% Mg series shown in Figure 5.58 - the cycles of which are cycle 80 to match the last of the 70Mg15Al15Ti sample - the reason for such different values for time to percent of maximum becomes apparent. The 70Mg15Al15Ti absorbs much more rapidly than either the

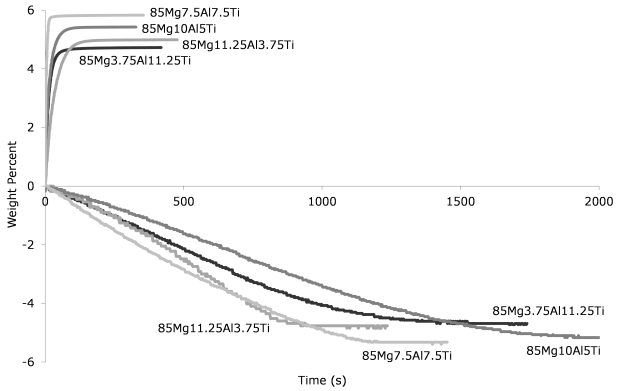

Figure 5.59: Cycle 120 curves of the samples from the 85% series of MgAlTi.

70Mg7.5Al22.5Ti or 70Mg20Al10Ti, rising almost vertically in comparison; the 70Mg7.5Al22.5Ti rises faster than the 70Mg20Al10Ti. The sorption curves are nearly linear in their initial rise, but the slowing of the 70Mg20Al10Ti and 70Mg7.5Al22.5Ti curves resembles the top half of a KJMA curve (Section 2.4.4); the 70Mg15Al15Ti, while appearing nearly linear, does curve towards the top of its rise. The desorption curves are an order of magnitude slower, as observed in the time to maximum graphs, curving much more gradually. While the curves appear to resemble both the CV model and the top of the KJMA mode, the 70Mg7.5Al22.5Ti has a more linear initial desorption which suggests the KJMA model would be a better fit.

The 85% Mg individual curves, in Figure 5.59, demonstrate again the rapid absorption of the 1:1 Al:Ti composition; 85Mg7.5Al7.5Ti is nearly vertical in its rise next to the other three compositions. The 85Mg10Al5Ti and 85Mg3.75Al11.25Ti are next fastest, sharing approximately the same absorption profile until they top out at different levels - and when comparing their time to maximum graphs, Figures 5.54 and 5.50, the relative separation of their 90%, 80% and 70% points are similar. The 85Mg11.25Al3.75Ti composition is slower, which is reflected in its time-to-maximum curves. The desorption curves are again long slow curves relative to the absorption profiles; two of them, the 85Mg10Al5Ti and 85Mg7.5Al7.5Ti are also visibly not parabolic (the shape of a CV curve), but

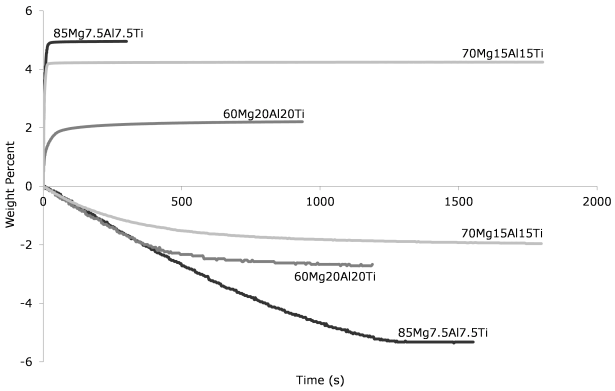

Figure 5.60: Cycle 80 curves of the 1:1 Al:Ti samples of MgAlTi.

they do resemble a KJMA curve; the two others would better fit a KJMA curve as well.

The example curves of the 1:1 Al:Ti ratios, in Figure 5.60, are compared in order to determine what effect simply increasing the Mg concentration has. Comparing the absorption curves it is evident that the increase from 70% to 85% Mg had little effect on the shape of the curves. When comparing maximum hydrogen sorbed it must be noted that these are individual cycles and the maximum is not necessarily indicative of the average maximum of the sample, as will be shown. The 60% Mg sample also shows the same vertical start, however it curves towards its maximum much more gradually.

In desorption, the 60% and 80% Mg show the most similarity, exhibiting the same slope until curving towards their respective limits. The 70% Mg also starts on the same trend, but has a reduced limit that it curves towards more rapidly. It should be noted again that absorption and desorption limits need not agree, as the desorbed samples were vacuumed out for 5 minutes after reaching their desorption limit; and that if their desorption caused the sample volume to approach the above-calculated plateau of 0.057 bar of H_2 desorption would cease.

The plot of maximum absorption versus cycle number of the 70% Mg series,

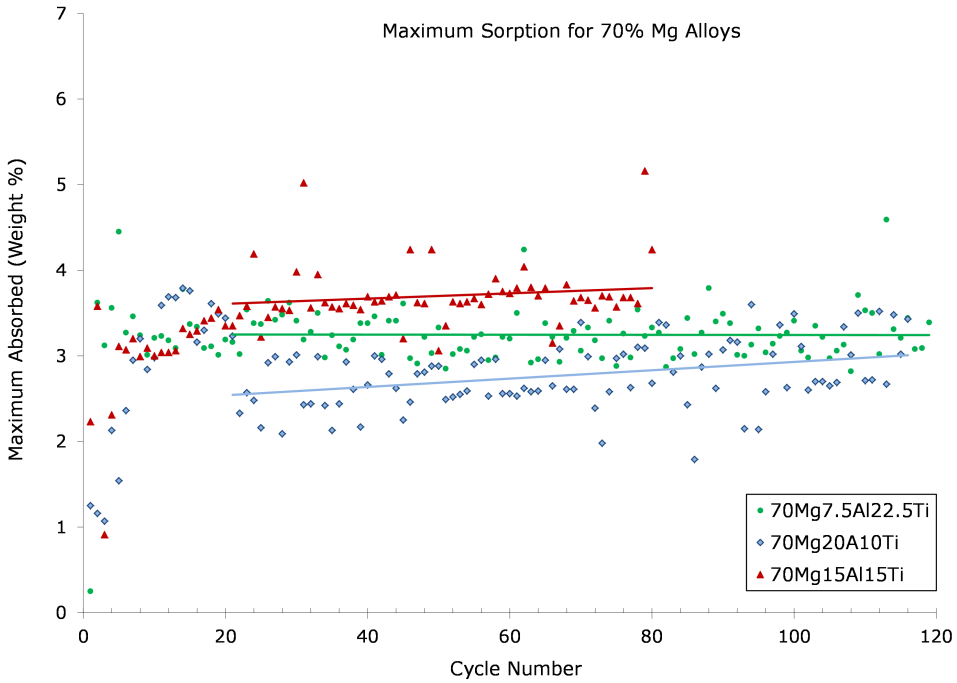

Figure 5.61: Maximum weight percentage absorbed by each 70% Mg composition for each cycle; the best fit line is a linear regression of the points excluding the first 20 cycles.

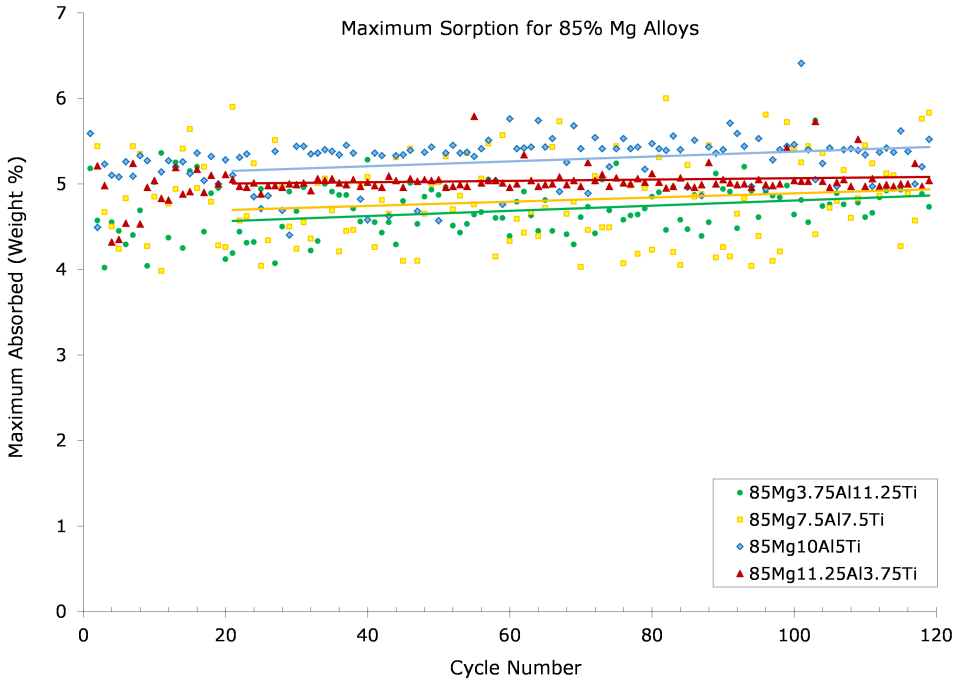

Figure 5.62: Maximum weight percentage absorbed by each 85% Mg composition for each cycle; the best fit line is a linear regression of the points excluding the first 20 cycles.

Figure 5.61, shows the large variance in the maximums observed; despite this large variance, trends and relative comparisons may be made, a task further enabled by linear regression of the series, excluding the first 20 cycles, as the above results suggested. It can be immediately seen that the 70Mg15Al15Ti has the highest absorption levels, followed by the 70Mg7.5Al22.5Ti, and lastly the 70Mg20Al10Ti. The median percentages absorbed for these three - excluding the first 20 cycles - were 3.63%, 3.22% and 2.71% respectively. The maximums of 70Mg15Al15Ti and 70 Mg7.5Al22.5Ti appear to have stabilized towards the end of their runs while 70Mg20Al10Ti was clearly still improving, though it was also below the other two, yet approaching them slowly.

The 85% Mg series maximum sorption plot, Figure 5.62, shows at first glance that the 85% Mg compositions are closely together within a band from 4% to

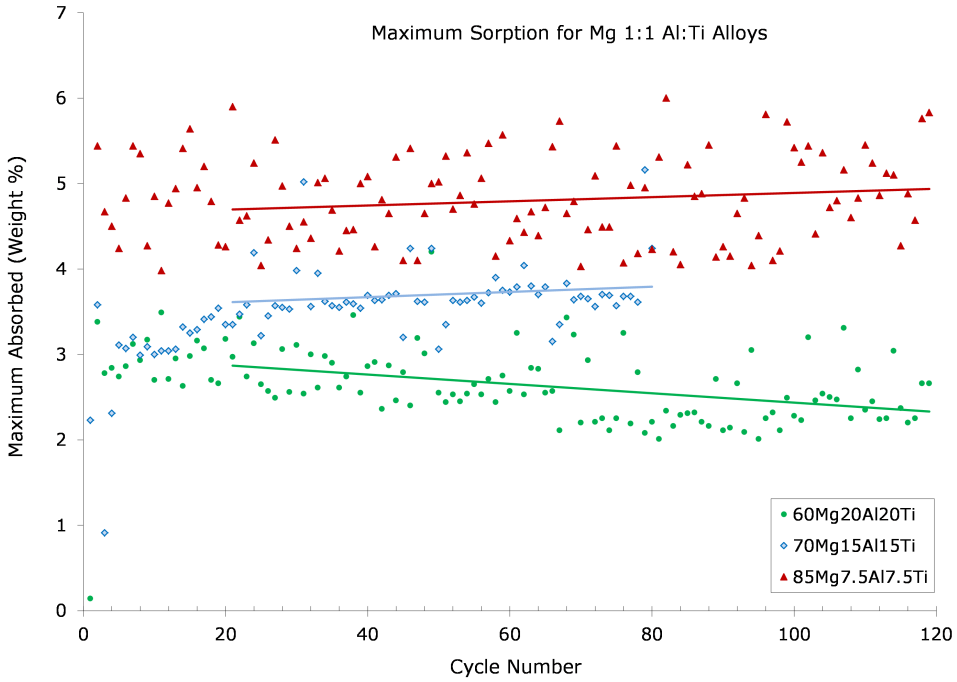

Figure 5.63: Maximum weight percentage absorbed by each of the 1:1 Al:Ti MgAlTi composition for each cycle; the best fit line is a linear regression of the points excluding the first 20 cycles.

6%. Upon closer inspection it is apparent that the 85Mg7.5Al5.5Ti composition is scattered across this region, 85Mg3.75Al11.25Ti is scattered along the bottom, 85Mg11.25Al3.75Ti is tightly grouped in the middle, and 85Mg10Al5Ti is loosely grouped at the top. All four appear stable with a very slight upwards trend for all but the 85Mg11.25Al3.75Ti. The median amounts absorbed - excluding the first 20 cycles - were 5.29% for 85Mg10Al5Ti, 5.01% for 85Mg11.25Al3.75Ti, 4.75% for 85Mg7.5Al7.5Ti and 4.71% for 85Mg3.75Al11.25Ti.

Comparing the 1:1 Al:Ti ratios maximum weight percentage absorbed H_2 in Figure 5.63 it is immediately obvious that maximum absorption average is higher with a higher Mg fraction. Furthermore, while 85% Mg and 70% Mg show stability with marginal upwards trends, the 60% Mg was trending downwards most of its run, although it appeared stable through its last 40 cycles.

Mg Fraction	Al:Ti Ratio	Median Maximum Absorbed	Median Time to X% of Maximum (s)					
			Absorbed			Desorbed		
			70%	80%	90%	70%	80%	90%
60%	1:1	2.55%	23.8	47.2	143	378	542	909
70%	1:3	3.22%	22.0	42.6	105	523	794	1244
70%	1:1	3.63%	5.3	6.9	9.6	302	438	695
70%	2:1	2.71%	41.7	67.8	125	617	836	1182
85%	1:3	4.71%	12.0	7.9	28.0	592	750	950
85%	1:1	4.75%	6.4	8.9	12.7	606	741	910
85%	2:1	5.29%	15.3	21.6	34.0	914	1067	1250
85%	3:1	5.01%	45.0	61.2	88.6	592	674	775

Table 5.1: A table of median values of indicators of stability and kinetics; the first 20 cycles have been ignored from all median values.

The median weight percentage of hydrogen absorbed for each Mg fraction - again excluding the first 20 cycles - was 4.75%, 3.63% and 2.55% for 85% Mg, 70% Mg and 60% Mg, respectively, a difference of over 1 weight percent between each.

Tables 5.1 and 5.2 have summaries of the Sieverts data for MgAlTi; in general, a higher Mg fraction yields higher quantities absorbed, and Al:Ti 1:1 appears to have the best kinetic enhancements in terms of speed to high fractions of maximum weight percentage absorbed.

Composition	Al:Ti Ratio	Trend		
		Maximum Absorbed	Time to X% of Maximum Absorption	Time to X% of Maximum Desorption
60Mg20Al20Ti	1:1	Decreasing	Increasing	Increasing
70Mg7.5Al22.5Ti	1:3	Stable	Increasing	Increasing
70Mg15A15Ti	1:1	Stable	Stable	Stable
70Mg20Al10Ti	2:1	Increasing	Stable	Stable
85Mg3.75Al11.25Ti	1:3	Stable	Stable	Stable
85Mg7.5Al7.5Ti	1:1	Stable	Stable	Stable
85Mg10Al5Ti	2:1	Stable	Increasing	Increasing
85Mg11.25Al3.75Ti	3:1	Stable	Increasing	Decreasing

Table 5.2: A table of trends of stability of the various MgAlTi compositions towards the end of their respective runs.

6

Conclusions

Hydrogen storage is an essential component of mobile fuel cell applications. The targets set out for this project were 6 weight% reversible capacity over many cycles, with an operating temperature below 100°C, requiring an adjustment to the enthalpy of hydride formation to $-40kJ/mol$ from $-74kJ/mol$ for desired pressures, and a charging time below 5 minutes. Median charging times of less than 15 seconds to 90% of maximum capacity were found in 85Mg7.5Al7.5Ti samples over 100 cycles, well within the target goal. A median of 5.29 weight% reversible storage was found in 85Mg10Al5Ti, 88% of the target goal. The maximums observed were, however, close to the theoretical maximums, as Pd and Ta caps were ~10% of the sample weight.

In the MgAl portion of the results, it was found that the as-sputtered MgAl

was primarily a shifted Mg phase - Al in solid solution with Mg - and that upon first hydrogenation both α-MgH_2 and γ-MgH_2 were created, with the α-MgH_2 phase being the dominant phase. Thermogravimetric Analysis (TGA) was used to minimize the thickness of a Pd catalytic layer, and neutron reflectometry showed that the films catalytic layer remained intact, and suggested the use of a Ta interlayer to prevent mixing of the Pd and Mg layers. Thermogravimetric Analysis further showed a gravimetric storage of 5.8 weight% in 70Mg30Al, and suggested that 200°C was required to fully desorb the samples over 10 hours, a value higher than expected for significant destabilizing of the hydride phase. Cycling of absorption and desorption in the Sieverts Apparatus found that the 70Mg30Al held the most hydrogen at just over 4 weight percent, followed by 80Mg20Al and 60Mg40Al, but that the cycles were stable in their times to a given percentage of maximum absorbed only for 60Mg40Al, and to a lesser degree the actual maximum weight percentage cycled. The preponderance of α-MgH_2 suggests that the enthalpy of hydride formation is unchanged from that of α-MgH_2, although presence of γ-MgH_2 may influence the first hydrogenation cycles.

The MgAlTi section found that the thermodynamic stability of the hydride - the enthalpy of hydride formation - was unchanged, determined via HPDSC and a *van't Hoff* plot, which gave values of -76.1 kJ/mol, which agrees with MgH_2, and -80.8 kJ/mol which is in rough agreement; no improvement in the enthalpy of hydride formation towards the desired -40 kJ/mol was observed. X-Ray Diffraction (XRD) also agreed, with α-MgH_2 and Mg being the dominant phases of the absorbed and desorbed compositions, respectively. The required cycling temperature was 200°C in the Sieverts Apparatus, the same as MgAl, and at the same pressures. XRD of MgAlTi also finds a lack of Al_xTi_y phases or Al or Ti phases, suggesting that Al and Ti are in an amorphous phase responsible for the large hump in the XRD of MgAlTi in the 33° to 43° range. Cycling also shows that a higher Mg fraction yields a higher weight percent absorbed; the 85Mg10Al5Ti sample held the most, with a me-

dian weight% stored of 5.29%. In both the 70% and 85% Mg samples, the 1:1 Al:Ti ratios were found to have the fastest absorption and desorption times, with both having median times to 90% of maximum stored of below 15 seconds. MgAlTi is found to be considerably faster than MgAl in both absorption and desorption. The cycling of MgAlTi indicated that the first ten to twenty cycles are typically much slower, likely a result of the initial nucleation of hydride grains, of which some likely remain between cycles. What exactly occurs to the microstructure of the compositions during this period has not been fully elucidated, and would require further study for a full understanding.

In summary, no improvement in the enthalpy of formation was observed in either MgAl or MgAlTi, but definite kinetic improvements are observed in MgAlTi compared to MgAl, especially at the 1:1 Al:Ti ratio. It was observed that the 70% Mg compositions were quite fast in absorption times, especially compared to samples with smaller fractions of Mg, but sacrificed significant maximum reversible hydrogen storage weight percentages; 85% Mg samples were observed to have similar absorption and desorption time improvements, but with significantly higher weight% hydrogen stored. Futher study should include the minimization of the catalytic layer, and finding the maximum fraction of Mg that can be used while maintaining favourable sorption properties. Co-sputtering proved to be a useful method of rapidly prototyping new materials, creating materials with the desired structure; the smooth films created also enabled the use of neutron reflectometry to investigate hydrogen storage behaviour directly. Cycling behaviour, however, was best observed in a Sieverts apparatus.

References

[1] K. J. Gross. *Intermetallic Materials for Hydrogen Storage*. PhD thesis, University of Fribourg, Fribourg, Switzerland, 1998.

[2] L. Schlapbach. Hydrogen as a Fuel and Its Storage for Mobility and Transport. *MRS Bulletin*, page 675, 2002.

[3] B. Sakintuna, F. Lamari-Darkrim, and M. Hirscher. Metal hydride materials for solid hydrogen storage: a review. *International Journal of Hydrogen Energy*, 32(9):1121–1140, 2007.

[4] Fuel cell, 1945. US Patent 2,384,463.

[5] H.F. Hunger. FUEL CELL WITH CATION EXCHANGE RESIN, 1961. US Patent 3,013,098.

[6] FT Bacon. Fuel cells, past, present and future* 1. *Electrochimica Acta*, 14(7): 569–585, 1969.

[7] PD Agarwal. The GM high-performance induction motor drive system. *IEEE Transactions on Power Apparatus and Systems*, pages 86–93, 1969.

[8] S. Dunn. Hydrogen futures: toward a sustainable energy system. *International Journal of Hydrogen Energy*, 27(3):235–264, 2002.

[9] J.M. Ogden. Developing an infrastructure for hydrogen vehicles: a Southern California case study. *International Journal of Hydrogen Energy*, 24(8):709–730, 1999.

[10] J.A. Ritter, A.D. Ebner, J. Wang, and R. Zidan. Implementing a hydrogen economy. *Materials Today*, 6(9):18–23, 2003.

[11] M.H. Maack and J.B. Skulason. Implementing the hydrogen economy. *Journal of Cleaner Production*, 14(1):52–64, 2006.

[12] D.P. Gregory. The hydrogen economy. *Scientific American*, 228(1):13–21, 1973.

[13] S. Satyapal, J. Petrovic, C. Read, G. Thomas, and G. Ordaz. The us department of energy's national hydrogen storage project: Progress towards meeting hydrogen-powered vehicle requirements. *Catalysis Today*, 120(3-4):246–256, 2007.

[14] L. Schlapbach and A. Zuttel. Hydrogen-storage materials for mobile applications. *Nature*, 414(6861):353–8, 2001.

[15] M.A. Kromer and J.B. Heywood. Electric Powertrains: Opportunities and Challenges in the US Light-Duty Vehicle Fleet. *Laboratory for Energy and the Environment. Massachusetts Institute of Technology. LFEE*, 3, 2007.

[16] S.A. Bhat and J. Sadhukhan. Process intensification aspects for steam methane reforming: an overview. *AIChE Journal*, 55(2):408–422, 2009.

[17] G. Keith, B. Biewald, D. White, and S.E. Economics. Evaluating Simplified Methods of Estimating Displaced Emissions in Electric Power Systems: What Works and What Doesn't. *Synapse Energy Economics*, 2004.

[18] Honda. Home hydrogen refueling technology advances with the introduction of honda's experimental home energy station. News Release, November 2005. http://world.honda.com/news/2005/c051114.html.

[19] Y. Tandon. Open versus closed energy systems and climate change. *Development*, 54(2):190–193, 2011.

[20] P.M. Cox, R.A. Betts, C.D. Jones, S.A. Spall, and I.J. Totterdell. Acceleration of global warming due to carbon-cycle feedbacks in a coupled climate model. *Acc. Chem. Res*, 28:37–44, 1995.

[21] A.P. Sokolov, P.H. Stone, C.E. Forest, R. Prinn, M.C. Sarofim, M. Webster, S. Paltsev, C.A. Schlosser, D. Kicklighter, S. Dutkiewicz, et al. Probabilistic

forecast for 21st century climate based on uncertainties in emissions (without policy) and climate parameters. *Journal of Climate*, 22:5175–5204, 2009.

[22] CE Thomas, B.D. James, F.D. Lomax Jr, and I.F. Kuhn Jr. Fuel options for the fuel cell vehicle: Hydrogen, methanol or gasoline? *International Journal of Hydrogen Energy*, 25(6):551–567, 2000.

[23] J. Xu, C.M.Y. Yeung, J. Ni, F. Meunier, N. Acerbi, M. Fowles, and S.C. Tsang. Methane steam reforming for hydrogen production using low water-ratios without carbon formation over ceria coated ni catalysts. *Applied Catalysis A: General*, 345(2):119–127, 2008.

[24] P.L. Spath and M.K. Mann. Life cycle assessment of hydrogen production via natural gas steam reforming. *National Renewable Energy Laboratory*, page 23, 2001.

[25] JE Funk and RM Reinstrom. Energy Requirements in Production of Hydrogen from Water. *Industrial & Engineering Chemistry Process Design and Development*, 5(3):336–342, 1966.

[26] LIU Mingyi, YU Bo, X. Jingming, and C. Jing. Thermodynamic analysis of the efficiency of high-temperature steam electrolysis system for hydrogen production. *Journal of Power Sources*, 177(2):493–499, 2008.

[27] C.W. Forsberg. Hydrogen, nuclear energy, and the advanced high-temperature reactor. *International Journal of Hydrogen Energy*, 28(10):1073–1081, 2003.

[28] A. Andreasen. Hydrogenation properties of Mg–Al alloys. *International Journal of Hydrogen Energy*, 33(24):7489–7497, 2008.

[29] T. Vegge. Locating the rate-limiting step for the interaction of hydrogen with mg (0001) using density-functional theory calculations and rate theory. *Physical Review B*, 70(3):035412, 2004.

[30] M. Dornheim, N. Eigen, G. Barkhordarian, T. Klassen, and R. Bormann. Tailoring hydrogen storage materials towards application. *Advanced Engineering*

Materials, 8(5):377–385, 2006.

[31] S. Bouaricha, J P Dodelet, D. Guay, J. Huot, S. Boily, and R. Schulz. Hydriding behavior of Mg–Al and leached Mg–Al compounds prepared by high-energy ball-milling. *Journal of Alloys and Compounds*, 297(1-2):282–293, 2000.

[32] E. Wicke, H. Brodowsky, and H. Züchner. *Hydrogen in Metals II: Hydrogen in Palladium and Palladium Alloys*. Springer, 1978.

[33] F.D. Manchester and A. San-Martin. *ASM Handbook: Alloy Phase Diagrams: H-Pd (Hydrogen - Palladium)*, volume 3. ASM International, 2002.

[34] L. Schlapbach. *Hydrogen in Intermetallic Compounds I: Introduction*. Springer, 1988.

[35] R. Griessen and T. Riesterer. *Hydrogen in Intermetallic Compounds I: Heat of Formation Models*. Springer, 1988.

[36] KHJ Buschow, PCP Bouten, and AR Miedema. Hydrides formed from intermetallic compounds of two transition metals: a special class of ternary alloys. *Reports on Progress in Physics*, 45:937–1039, 1982.

[37] P. Vermeulen, E. F. M. J. van Thiel, and P. H. L. Notten. Ternary MgTiX-Alloys: A Promising Route towards Low-Temperature, High-Capacity, Hydrogen-Storage Materials. *Chemistry-A European Journal*, 13(35):9892–9898, 2007.

[38] D.V. Schroeder. *Introduction to Thermal Physics*. Addison Wesley Longman, San Francisco, 2000.

[39] F.D. Manchester, A. San-Martin, and J.M. Pitre. The H-Pd (hydrogen-palladium) System. *Journal of Phase Equilibria*, 15(1):62–83, 1994.

[40] R. Wiswall. *Hydrogen in Metals II: Hydrogen Storage in Metals*. Springer, 1978.

[41] Y. Li and R.T. Yang. Hydrogen Storage in Metal-Organic Frameworks by Bridged Hydrogen Spillover. *J. Am. Chem. Soc*, 128(25):8136–8137, 2006.

[42] SJ Van Der Molen, JWJ Kerssemakers, JH Rector, NJ Koeman, B. Dam, and R. Griessen. Hydriding kinetics of Pd capped YH switchable mirrors. *Journal of Applied Physics*, 86:6107, 1999.

[43] L. Zaluski, A. Zaluska, P. Tessier, J O Ström-Olsen, and R. Schulz. Catalytic effect of Pd on hydrogen absorption in mechanically alloyed Mg2Ni, LaNi5 and FeTi. *Journal of Alloys and Compounds*, 217(2):295–300, 1995.

[44] K. Yoshimura, Y. Yamada, and M. Okada. Hydrogenation of Pd capped Mg thin films at room temperature. *Surface Science*, 566:751–754, 2004.

[45] A. Zaluska, L. Zaluski, and J O Ström-Olsen. Nanocrystalline magnesium for hydrogen storage. *Journal of Alloys and Compounds*, 288(1-2):217–225, 1999.

[46] K. Otto, CP Hubbard, WH Weber, and GW Graham. Raman spectroscopy of palladium oxide on [gamma]-alumina applicable to automotive catalysts:: Nondestructive, quantitative analysis; oxidation kinetics; fluorescence quenching. *Applied Catalysis B: Environmental*, 1(4):317–327, 1992.

[47] P. Shewmon. *Diffusion in solids*. The Minerals, Metals & Materials Society, Diffusion in Solids. Second Edition.(Retroactive Coverage)(United States), 1989, 1989.

[48] HG Schimmel, GJ Kearley, J. Huot, and FM Mulder. Hydrogen diffusion in magnesium metal (phase) studied by ab initio computer simulations. *Journal of alloys and compounds*, 404:235–237, 2005.

[49] S. Hao and D.S. Sholl. Hydrogen diffusion in mgh and namgh via concerted motions of charged defects. *Applied Physics Letters*, 93:251901, 2008.

[50] FH Ellinger, CE Holley Jr, BB McInteer, D. Pavone, RM Potter, E. Staritzky, and WH Zachariasen. The preparation and some properties of magnesium hydride. Technical report, AECU-2970, Los Alamos Scientific Lab., 1954.

[51] JF Stampfer Jr, CE Holley Jr, and JF Suttle. The magnesium-hydrogen system. *Journal of the American Chemical Society (US)*, 1960.

[52] H. Okamoto. Al-Mg (aluminum-magnesium). *Journal of Phase Equilibria and Diffusion*, 19(6):598–598, 1998.

[53] R A H Niessen and P H L Notten. Electrochemical hydrogen storage characteristics of thin film MgX (X= Sc, Ti, V, Cr) compounds. *Electrochemical and Solid-State Letters*, 8:A534, 2005.

[54] CV Thompson. Grain growth in thin films. *Annual Review of Materials Science*, 20(1):245–268, 1990.

[55] J.A. Thornton. Influence of apparatus geometry and deposition conditions on the structure and topography of thick sputtered coatings. *Journal of Vacuum Science and Technology*, 11:666, 1974.

[56] C.V. Thompson and R. Carel. Stress and grain growth in thin films. *Journal of the Mechanics and Physics of Solids*, 44(5):657–673, 1996.

[57] S.A. Campbell. *The science and engineering of microelectronic fabrication*. Oxford University Press New York, 1996.

[58] C. Ophus, EJ Luber, M. Edelen, Z. Lee, LM Fischer, S. Evoy, D. Lewis, U. Dahmen, V. Radmilovic, and D. Mitlin. Nanocrystalline–amorphous transitions in Al–Mo thin films: Bulk and surface evolution. *Acta Materialia*, 57(14):4296–4303, 2009.

[59] R.L. Holtz and M.A. Imam. Hydrogen storage capacity of submicron magnesium–nickel alloys. *Journal of Materials Science*, 32(9):2267–2274, 1997.

[60] M.Y. Song, J.L. Bobet, and B. Darriet. Improvement in hydrogen sorption properties of Mg by reactive mechanical grinding with Cr2O3, Al2O3 and CeO2. *Journal of Alloys and Compounds*, 340(1-2):256–262, 2002.

[61] ASW Wong, DZ Chi, M. Loomans, D. Ma, MY Lai, WC Tjiu, SJ Chua, CW Lim, and JE Greene. F-enhanced morphological and thermal stability of NiSi films on BF-implanted Si (001). *Applied Physics Letters*, 81:5138, 2002.

[62] HC Kim and TL Alford. Improvement of the thermal stability of silver metal-

lization. *Journal of applied physics*, 94:5393, 2003.

[63] J F Herbst. On extending Miedema's model to predict hydrogen content in binary and ternary hydrides. *Journal of Alloys and Compounds*, 337(1-2):99–107, 2002.

[64] J.L. Murray. The Mg–Ti (Magnesium-Titanium) system. *Journal of Phase Equilibria*, 7(3):245–248, 1986.

[65] J.C. Schuster and M. Palm. Reassessment of the binary aluminum-titanium phase diagram. *Journal of Phase Equilibria and Diffusion*, 27(3):255–277, 2006.

[66] I. Ohnuma, Y. Fujita, H. Mitsui, K. Ishikawa, R. Kainuma, and K. Ishida. Phase equilibria in the Ti–Al binary system. *Acta Materialia*, 48(12):3113–3123, 2000.

[67] XH Lin and WL Johnson. Formation of Ti-Zr-Cu-Ni bulk metallic glasses. *Journal of Applied Physics*, 78(11):6514–6519, 1995.

[68] A.A. Nayeb-Hashemi and J.B. Clark. The Mg- Pd (magnesium-palladium) system. *Journal of Phase Equilibria*, 6(2):164–167, 1985.

[69] H. Okamoto. Pd-Ta (Palladium-Tantalum). *Journal of Phase Equilibria and Diffusion*, 28(2):233–233, 2007.

[70] R.E. Buxbaum and A.B. Kinney. Hydrogen transport through tubular membranes of palladium-coated tantalum and niobium. *Ind. Eng. Chem. Res*, 35 (2):530–537, 1996.

[71] S. Bouaricha, J. Huot, D. Guay, and R. Schulz. Reactivity during cycling of nanocrystalline Mg-based hydrogen storage compounds. *International Journal of Hydrogen Energy*, 27(9):909–913, 2002.

[72] NM Peachey, RC Snow, and RC Dye. Composite Pd Ta metal membranes for hydrogen separation. *Journal of Membrane Science*, 111(1):123–133, 1996.

[73] SA Steward. Review of hydrogen isotope permeability through materials. Tech-

nical report, UCRL-53441, Lawrence Livermore National Lab., CA (USA), 1983.

[74] Jacques Huot. *Hydrogen technology: mobile and portable applications*. Springer Verlag, 2008.

[75] AA Burbelko, E. Fras, and W. Kapturkiewicz. About Kolmogorov's statistical theory of phase transformation. *Materials Science and Engineering: A*, 413: 429–434, 2005.

[76] JA Puszkiel, P. Arneodo Larochette, and FC Gennari. Hydrogen storage properties of MgxFe (x: 2, 3 and 15) compounds produced by reactive ball milling. *Journal of Power Sources*, 186(1):185–193, 2009.

[77] W.D. Callister and D.G. Rethwisch. *Materials science and engineering: an introduction*. John Wiley & Sons New York:, 1997.

[78] K.G. Budinski and M.K. Budinski. *Engineering materials: properties and selection*. Prentice Hall, 2005.

[79] J.F. Shackelford. *Introduction to materials science for engineers*. Prentice Hall, 2005.

[80] H. Fritzsche, M. Saoudi, J. Haagsma, C. Ophus, E. Luber, CT Harrower, and D. Mitlin. Neutron reflectometry study of hydrogen desorption in destabilized MgAl alloy thin films. *Applied Physics Letters*, 92:121917, 2008.

[81] L.G. Parratt. Surface studies of solids by total reflection of x-rays. *Physical Review*, 95(2):359, 1954.

[82] H.E. Kissinger. Reaction kinetics in differential thermal analysis. *Analytical chemistry*, 29(11):1702–1706, 1957.

[83] R. Domenech-Ferrer, M. Gurusamy Sridharan, G. Garcia, F. Pi, and J. Rodríguez-Viejo. Hydrogenation properties of pure magnesium and magnesium–aluminium thin films. *Journal of Power Sources*, 169(1):117–122, 2007.

[84] M. Fichtner, O. Fuhr, and O. Kircher. Magnesium alanate-a material for reversible hydrogen storage? *Journal of Alloys and Compounds*, 356:418–422, 2003.

[85] R. Gremaud, A. Borgschulte, W. Lohstroh, H. Schreuders, A. Züttel, B. Dam, and R. Griessen. Ti-catalyzed Mg (AlH4) 2: A reversible hydrogen storage material. *Journal of Alloys and Compounds*, 404:775–778, 2005.

[86] K. Zeng, T. Klassen, W. Oelerich, and R. Bormann. Critical assessment and thermodynamic modeling of the mg-h system. *International journal of hydrogen energy*, 24(10):989–1004, 1999.

[87] H. Fritzsche, M. Saoudi, J. Haagsma, C. Ophus, C.T. Harrower, and D. Mitlin. Structural changes of thin MgAl films during hydrogen desorption. *Nuclear Inst. and Methods in Physics Research, A*, 600(1):301–304, 2009.

[88] H. Fritzsche, E. Poirier, J. Haagsma, C. Ophus, E. Luber, CT Harrower, and D. Mitlin. A systematic neutron reflectometry study on hydrogen absorption in thin mg1-xalx alloy films. *Canadian Journal of Physics*, 88, 2010.

[89] WP Kalisvaart, CT Harrower, J. Haagsma, B. Zahiri, EJ Luber, C. Ophus, E. Poirier, H. Fritzsche, and D. Mitlin. Hydrogen storage in binary and ternary mg-based alloys: A comprehensive experimental study. *International Journal of Hydrogen Energy*, 35(5):2091–2103, 2010.

[90] Z. Lee, C. Ophus, LM Fischer, N. Nelson-Fitzpatrick, KL Westra, S. Evoy, V. Radmilovic, U. Dahmen, and D. Mitlin. Metallic nems components fabricated from nanocomposite al–mo films. *Nanotechnology*, 17:3063, 2006.